Carbon Nanostructures Under High Pressure Studied By Infrared Spectroscopy

Dissertation zur Erlangung des Doktorgrades
der Mathematisch-Naturwissenschaftlichen
Fakultät der Universität Augsburg

vorgelegt von
Komalavalli Thirunavukkuarasu

April 2009

Erstgutachter:	Prof. Dr. C.A. Kuntscher
Zweitgutachter:	Prof. Dr. A. Wixforth

Tag der mündlichen Prüfung: 25 May 2009

Contents

1 Introduction

The study of carbon nanostructures has emerged to be a giant thriving field of research with the discovery of fullerenes in 1985 by Kroto and coworkers, and subsequently carbon nanotubes in 1991 by Iijima and coworkers. Extremely varied properties of the carbon-based nanomaterials arise due to its exotic form which leads to reduced dimensionality. While diamond and graphene (graphite) are well known three-dimensional (3D) and two-dimensional (2D) forms of carbon, the fullerenes and carbon nanotubes form the zero-dimensional (0D) and one-dimensional (1D) forms, respectively. Due to the reduced dimensionality, the carbon nanostructures exhibit interesting physical properties induced by strong many-body correlation effects. Some interesting properties of these carbon nanostructures are outstanding mechanical, thermal, electronic, and electrical properties and chemical robustness. Furthermore, fullerenes readily form derived materials by combining with a large variety of materials like organic molecules, alkali metals, etc., to form a wide class of materials (for e.g. alkali fullerides, endohedral fullerenes, exohedral fullerenes, host-guest compounds, polymerized fullerenes) with extremely broad range of properties. Therefore, fullerenes and its derivatives have endless list of applications in optical limiters, transistors, catalysts, hydrogen storage, etc. For this reason, enormous efforts have been undertaken for reliable understanding of the basic properties of these carbon nanostructures. In addition to the applications, the fullerene-based materials and the carbon nanotubes offer a large scope for studying the various physical phenomena induced in the low-dimensional systems. The low-dimensional systems have shed new light on the effects of electron-phonon interactions, disorder (for example, impurities) and electron-electron interaction on a quantum system.

Within this project, the study of vibrational and the electronic properties of carbon-based nanostructures, namely fullerene compounds and carbon nanotubes, has been performed. The main goal of this project is the characterization of phenomena induced by the application of external pressure such as structural phase transitions, insulator-to-metal transition and polymerization reactions using infrared spectroscopy in the far-infrared up to the visible frequency range as a function of pressure.

Infrared spectroscopy together with the low temperature and high pressure techniques forms a powerful tool to investigate the dynamics of the charge carriers and provides important information on the fundamental energy scales involved in the various physical phenomena. It allows study of both electronic and vibrational excitations, providing useful information on the microscopic mechanism that builds up the electronic properties of the carbon nanostructures. External hydrostatic pressure compresses the lattice increasing the bandwidth of the electronic states and also induces structural phase transitions. Therefore, in general, the application of pressure is considered a cleaner way to tune the properties of materials under investigation than chemical doping, in order to understand the electronic properties. The combination of high pressure with Raman spectroscopy is well established and widely used, but the coupling of infrared spectroscopy to the high pressure techniques proved to be more difficult. The main limitations arise from the sample size which causes diffraction artifacts and intensity of the sources. Although the limitations could be partly overcome by use of infrared microscope and synchrotron radiation facilities, the difficulty of the experiments make high pressure infrared spectroscopy less common and more novel.

The first part of the project is dedicated to the investigations on C_{60}·C_8H_8 and C_{70}·C_8H_8 which belong to a new class of rotor-stator fullerene compounds, and the fullerite C_{70} at high pressures over a broad frequency range.

The fullerene-based materials are van der Waals crystals where the molecules are rotating freely at high temperatures. On cooling or with the application of pressure, the fullerites undergo orientational ordering transitions where the free rotation of the fullerene molecules are restricted and eventually frozen. Therefore, the vibrational degrees of freedom play an intrinsic role in these classes of materials. The vibrational spectra are sensitive indicators for symmetry change during phase transitions, electron-phonon coupling, and other variations in the internal dynamics of a material. The crystalline C_{70} undergoes a series of orientational ordering transitions up on cooling. Generally, high pressure is expected to have the same effect as low temperature. Therefore, similar orientational ordering transition is expected to occur with the application of pressure. Although, several pressure-dependent experimental investigations have been performed on the C_{70} fullerite, the pressure-induced changes in the symmetry and intermolecular interactions have not been completely understood. The pressure-induced phase transition in the solid C_{70} has been reported by studies such as X-ray diffraction. However, optical spectroscopic investigations found no consistent observations related to the pressure-induced transitions indicating a need for further optical studies on solid C_{70}.

The new class of rotor-stator compounds, C_{60}·C_8H_8 and C_{70}·C_8H_8, synthesized recently, are fullerene-cubane mixed crystals where cubane molecules occupy the interstitial sites between the fullerene balls. The curvature of the balls perfectly matches the concave surface of cubane. In these crystals, the cubane act as stator while the fullerenes freely rotate as rotors. The orientational phase transition in these crystals occur at temperatures much lower than in any other known fullerene system. The investigations on these compounds under hydrostatic pressure can therefore throw light on the pressure-induced structural transitions. Furthermore, the interaction between the fullerene and cubane plays a vital role in determining the properties of these materials. Thus, the mechanism of the intermolecular interactions in these high-symmetry fullerene compounds can enable us to gain insight into the nature of intermolecular interactions in the fullerene-based van der Waals crystals. This can be achieved by varying the intermolecular distances and consequently the interactions between them with the application of pressure.

Using infrared spectroscopy at high pressures, both the vibrational and the electronic properties of the fullerene-based compounds, C_{70}, $C_{60}{\cdot}C_8H_8$ and $C_{70}{\cdot}C_8H_8$ have been investigated to look for signatures of phase transitions and intermolecular interactions which play a dominant role in determining the physical properties of these materials.

In addition, infrared spectroscopic measurements on unoriented SWCNT films (both as-prepared and purified SWCNT films) at high pressures have been performed over a wide energy range. The polarization-dependent infrared spectroscopic measurements have been performed for the first time on oriented SWCNT films (oriented nanotubes in polyethylene matrix and magnetically-aligned SWCNT film) over a broad frequency range. The temperature-dependent studies at ambient pressure have been performed on the unoriented SWCNT films to compare the effect of temperature and pressure on the SWCNT films.

The investigation of SWCNTs under high pressure is particularly interesting as one can induce structural deformations of the SWCNTs and study their effect on the electronic, vibrational, and mechanical properties. Furthermore, one can tune the distance between the SWCNTs by the application of pressure and hence study the influence of intertube interactions. The structural and electronic properties of SWCNTs are extremely sensitive to external pressure. Small deformations in the structure of highly elastic SWCNTs can induce large changes in its electronic properties. This unique property of SWCNTs with a great potential for applications needs to be thoroughly understood. Therefore, an attempt has been made to study the pressure-induced phenomena like structural phase transition, carrier localization, and other changes in the low-energy band structure of various unoriented and oriented SWCNT films using infrared spectroscopy. From the polarization-dependent optical response of the oriented SWCNT films under pressure further information on how the anisotropy of the optical properties changes with pressure, and whether a dimensional crossover of this highly anisotropic system from one to two dimensions is induced above a certain pressure can be inferred.

The introduction to the experimental techniques i.e., the infrared spectroscopy, high-pressure generation and low-temperature technique, and the analysis methods required for extracting the physical information are presented in upcoming Chapter 2. Chapter 3 presents the basic properties of the investigated fullerene-based compounds, and subsequently the experimental investigations performed within this work and their implications. Basic properties of SWCNTs and the changes in the electronic response of the nanotubes under extreme conditions (low temperature or high pressure) are presented in Chapter 4 before finally summarizing the findings of this work in the Chapter 5.

2 Experimental Techniques

The pressure-dependent infrared measurements presented in this work were performed using a Fourier transform Infrared (FTIR) spectrometer (Bruker IFS66v/S) coupled to an infrared (IR) microscope. The IR microscope, in conjunction with the spectrometer, allows measurements involving very small samples. Therefore, it is an essential equipment in order to perform IR measurements at high pressures using diamond anvil cells (DACs) where the studied samples do not exceed micrometer dimensions. In this chapter, the important information about the experimental realization of the infrared spectroscopy at high pressure are explained. A brief description of the low temperature technique is also presented.

2.1 Fourier transform infrared spectroscopy

2.1.1 Principle of Fourier transform spectroscopy

The foundations of the FTIR spectroscopy lie in the working of Michelson interferometer and mathematical operation of Fourier transformation. The working principle of a simple FTIR spectrometer is shown in Figure 2.1. Energy from a conventional source is directed towards a beamsplitter. The beamsplitter creates two separate optical paths by partially reflecting and partially transmitting the incident light. One part of the beam is then reflected by a fixed mirror and the other part is reflected by a movable mirror that translates back and forth. The two beams are then recombined at the beamsplitter before reaching the detector. The energy that reaches the detector is therefore the sum of these two beams. When the distance between the beamsplitter and the fixed and movable mirrors are the same, the optical path length traveled by the two beams are equal. When the movable mirror is moved, the optical path difference (δ) becomes nonzero.

Figure 2.1 shows the schematic of the working principle of an FTIR spectometer. As δ is increased the signal from the detector - the interferogram - goes through a series of maxima and minima. The maxima occur when δ is an integral multiple of wavelengths of the emitting source (i.e., δ = nλ; n=0,±1,±2, etc.,). The minima occur when δ is

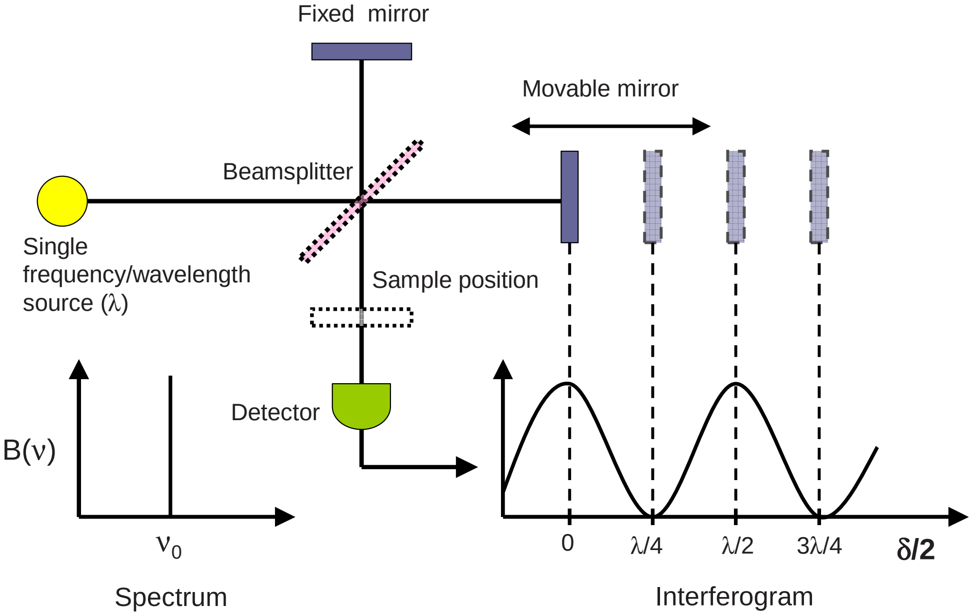

Figure 2.1: *Schematic illustration explaining the working principle of an FTIR spectrometer. The figure illustrates how an interferogram is generated as the movable mirror is translated for a spectrum of infinitely narrow line source.*

an odd multiple or half wavelengths (i.e., δ=[n+$\frac{1}{2}\lambda$]). The resulting interferogram can be described as an infinitely long cosine wave defined by the equation

$$I(\delta) = B(\nu)cos(2\pi\delta\nu[cm^{-1}]) \tag{2.1}$$

in which I(δ) is the intensity of the detector signal as a function of optical path difference and B(ν) is the intensity or brightness of the source as a function of frequency ν given in cm^{-1}. When the source emits more than one frequency, it is possible, to treat each frequency as a result of a cosine function with its own periodicity and then add the cosine waves to obtain the form of the resultant interferogram. Mathematically the interferogram can be defined as a sum of the cosine waves of all the frequencies present in the source as,

$$I(\delta) = \sum_{\nu_1}^{\nu_n} B(\nu_i)cos(2\pi\delta\nu_i) \tag{2.2}$$

A typical infrared source emits a continuous spectrum and therefore the summation is replaced by an integral,

$$I(\delta) = \int_0^{\infty} B(\nu)cos(2\pi\delta\nu)d\nu \tag{2.3}$$

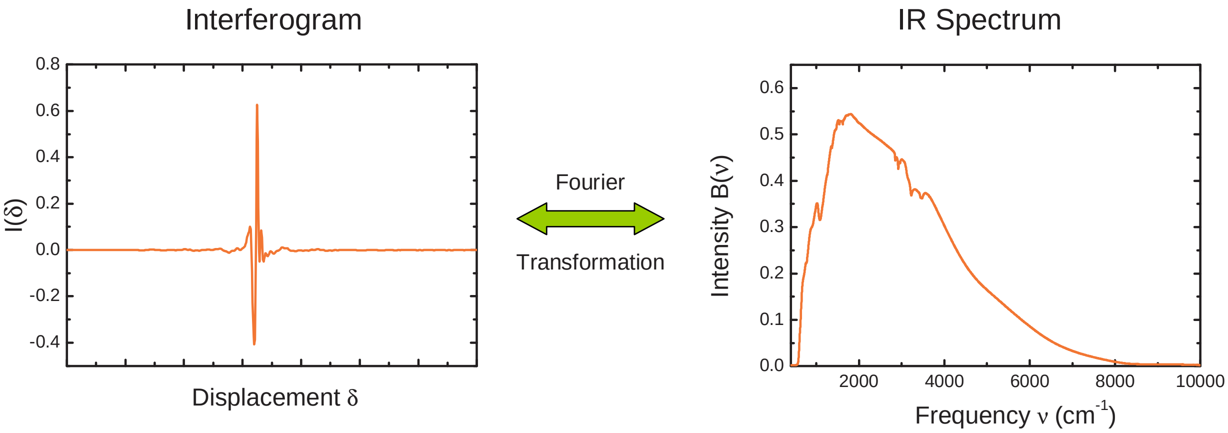

Figure 2.2: *A typical interferogram and its corresponding spectrum in the MIR frequency range obtained in a FTIR spectrometer.*

A typical interferogram and the corresponding spectrum is shown in Figure 2.2. At zero optical path difference ($\delta = 0$), all cosine waves from all frequencies present are in phase. Thus the signal I(δ) always has a strong maximum at $\delta = 0$ and this feature of the interferogram is known as the centerburst. As we move outward in either direction of the centerburst, the multitudinous cosine waves begin to reinforce and cancel each other, and the intensity of the interferogram dies off rapidly in to a series of lower amplitude oscillations.

However, the interferogram is measured only over a finite path difference, i.e., the mirror displacement is $(\delta)\leq(\delta_{max})$). This finite movement of the mirror can be expressed by multiplying the interferogram function with a window function. Abrupt termination of the interferogram due to this window function introduces false side lobes into the transformed spectra causing distortion in the analyzed spectrum. Removing or suppressing them is accomplished by replacing the window function with other functions. This process is known as apodization. The restriction of the apodization not only limits the resolution to $\Delta\nu = 1/\delta_{max}$, but also leads to errors in the calculated spectrum depending on the extrapolations used.

The principal advantage of Fourier transform spectroscopy is that the interferogram contains information about all spectral elements thereby avoiding loss of information in a single measurement. Fourier transform spectroscopy offers excellent signal-to-noise ratio in considerably shorter time compared to grating spectroscopy without loss of spectral resolution.

Frequency range	Source	Beamsplitter	Polarizer	Detector
Farinfrared 10 - 700 cm^{-1}	Hg discharge lamp	50 μm Mylar/Ge 23 μm 6 μm	Polyethylene	Bolometer DTGS
Midinfrared 500 - 8000 cm^{-1}	Globar	KBr/Ge	KRS-5	MCT detector DTGS
Nearinfrared 2000 - 12000 cm^{-1}	Tungsten lamp	CaF$_2$	KRS-5	InSb detector
Visible/UV 10000 - 26000 cm^{-1}	Tungsten lamp	CaF$_2$	Prism	Si diode GaP diode

Table 2.1: *Different sources, beamsplitters, polarizers and detectors used for various infrared frequency ranges for measurements using the Fourier transform spectrometer.*

2.1.2 Fourier transform infrared spectrometer

The infrared measurements within this project were performed using the FTIR spectrometer Bruker IFS66v/S. The optical layout of this FTIR spectrometer is shown in Figure 2.3.

The FTIR spectrometer can cover a broad frequency range from 10 to 30000 cm^{-1} i.e., far-infrared (FIR) to visible frequencies. It employs three different light sources for the different ranges in the infrared frequencies. Depending on the frequency required for the measurement, different combinations of source, beamsplitter and the detector are chosen. The size of the beam spot can be chosen using apertures of size 0.25 - 12 mm with the remotely-controlled aperture wheel (see Figure 2.3). The list of sources, beamsplitters, polarizers and detectors used for the different frequency ranges in the spectrometer are listed in Table 2.1.

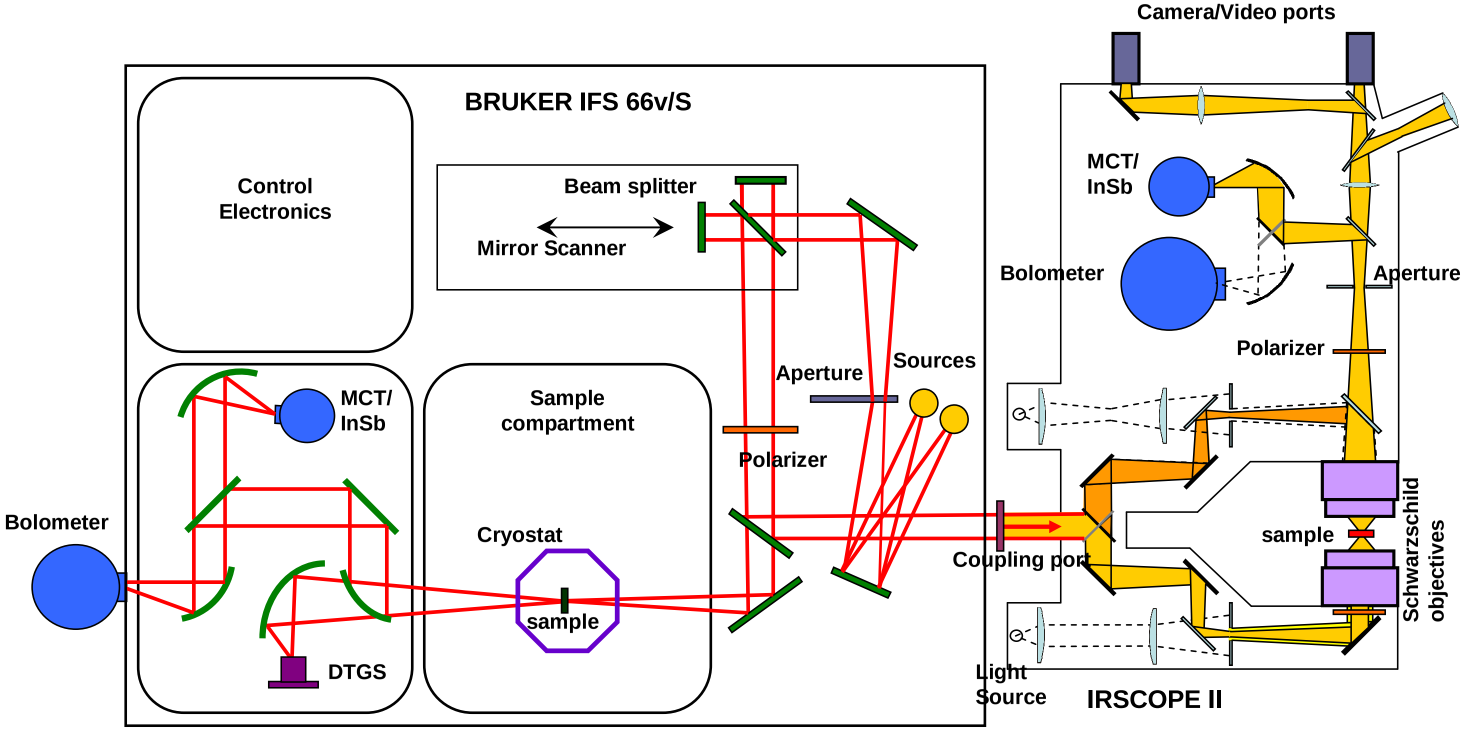

Figure 2.3: *Optical layout of Bruker IFS66v/S Fourier transform infrared spectrometer coupled to IR microscope illustrating the their coupling and the entire optical configuration.*

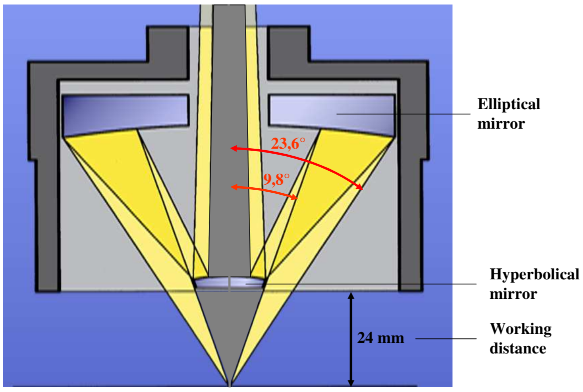

Figure 2.4: *Basic construction of a Schwarzschild or cassegrain objective used in an infrared microscope.*

The silicon-based bolometer used in the FIR frequency range is a cryogenic detector operated at liquid helium temperature, while mercury cadmium telluride (MCT) and InSb detectors used at mid-infrared (MIR) and near-infrared (NIR) frequencies, respectively, are operated at liquid nitrogen temperature. Deuterated triglycine sulfate (DTGS) detectors that are used optionally in FIR and MIR ranges are operable at room temperature. A silicon diode and a GaP diode detector can be used for the measurements in the visible/UV range.

2.1.3 Infrared microscope

The infrared microscope coupled to the spectrometer conveniently enables measurements of samples of several tens of micrometers of dimensions, in the frequency range 50 - 22000 cm^{-1}. The lowest measurable frequency is determined by the diffraction limit of the microscope. The microscope used within this thesis work may be coupled to all detectors (see Table 2.1 for the list of the detectors used for various frequency ranges). The polarization of the incident light can be accomplished either using the polarizer at the spectrometer or by using the polarizers inserted in the main optical path of the infrared microscope. The main advantage of using IR microscope is that a specific area on the sample can be chosen for the measurement. It is indeed particularly useful in the measurement of optical properties of materials under pressure in which a highly focused light is required as the samples have dimensions of $\sim 100 \times 100$ μm^2 or even less.

Basic construction of the infrared microscope

The optical layout of the infrared microscope is shown in Figure 2.3. The main parts of the infrared microscope are two identical Schwarzschild (or cassegrain) objectives. One objective is used for focusing the light on the sample and the second one serves as condenser for transmission measurements. The basic construction of a Schwarzschild objective is shown in Figure 2.4. Each objective consists of a concave and a convex mirror; the objectives used in the current setup have a magnification of 15x and a working distance of 24 mm. Field apertures in the focal plane of the objective, of sizes in the range of 0.3 - 3.75 mm, are used to define the sample area to be analyzed. Through a system of remotely-controlled mirrors, it is possible to guide the incident light in the optical path of the microscope for the view mode, the reflection mode and the transmission mode.

2.2 Infrared spectroscopy and optical response functions

In this section, the physical quantities that can be obtained from the infrared spectroscopic measurements are described briefly. The definitions of various optical response functions and the analysis models required for understanding the investigations performed as a part of this thesis work are presented. See Ref. [1–3] for more detailed information on the first two subsections.

2.2.1 Optical response functions

The optical response functions of the studied materials can be determined by means of optical spectroscopy. The optical properties of the materials are described by the complex refractive index $\tilde{n}$:

$$\tilde{n} = n + ik \quad , \tag{2.4}$$

where n and k give the refractive index and extinction coefficient of the material. When the refractive index is known, it is possible to determine the complex dielectric constant $\tilde{\epsilon}$ ($\tilde{\epsilon} = \epsilon_1 + i\epsilon_2$) which is related to the refractive index as

$$\tilde{\epsilon} = \tilde{n}^2 \quad . \tag{2.5}$$

The measured quantities, namely the reflectivity and the transmittance, are related to the complex refractive index and dielectric function. The reflectivity (R) of a material at normal incidence is related to the complex refractive index by Fresnel equation as:

$$R = \left|\frac{\tilde{n} - n_w}{\tilde{n} + n_w}\right|^2 \quad , \tag{2.6}$$

where n_w is the refractive index of the medium which forms the interface at the reflecting surface of the sample. When the medium is air or vacuum then the expression reduces to

$$R = \frac{(n-1)^2 + k^2}{(n+1)^2 + k^2} \quad . \tag{2.7}$$

The transmittance of the material is then given by the expression

$$T = \frac{[(1-R)^2 + 4Rsin(\phi)^2]e^{-\alpha d}}{(1-Re^{-\alpha d})^2 + 4Re^{-\alpha d}sin(\beta+\phi)^2} \quad , \tag{2.8}$$

where α is the power absorption coefficient given by $4\pi\mathrm{k}/\lambda_0$ (λ_0 is the wavelength in vacuum), d is the thickness of the material, and β and ϕ are the phase change upon passing through the material and reflection, respectively. They are defined as

$$\phi = arctan\left\{\frac{-2k}{1-n^2-k^2}\right\} \quad ; \beta = \frac{2\pi nd}{\lambda_0} \quad . \tag{2.9}$$

Experimentally, the reflectivity of a material can be determined by normalizing the intensity of light reflected from the surface of the sample during normal incidence by the intensity of light reflected from the surface of a nearly-100% reflecting material. Generally, the nearly-100% reflecting material is known as a reference and the references that are commonly used are mirrors made of Al, Au and Ag. In case of transmittance measurement, the intensity of light transmitted through the sample is normalized to the intensity of light without the sample. Thus, the reference is the light through the empty sample holder or some matrix media (for e.g. KBr) of powder samples.

2.2.2 Drude-Lorentz model

Drude-Lorentz model has been successfully employed to describe the measured reflectivity or transmittance. This model allows one to describe the dielectric function of both the free carriers (so called Drude term) and the localized carriers (so called Lorentz term). The dielectric function of materials according to the Drude-Lorentz model can be written as

$$\epsilon(\omega) = \epsilon_\infty - \frac{\omega_p^2}{\omega^2 + i\Gamma\omega} + \sum_j \frac{\omega_{p,j}^2}{(\omega_j^2 - \omega^2) - i\Gamma_j\omega} \tag{2.10}$$

where ω_p is the plasma frequency of the corresponding excitation, Γ is the damping due to energy loss mechanisms, ω is the frequency of the incident radiation, and ω_j is the

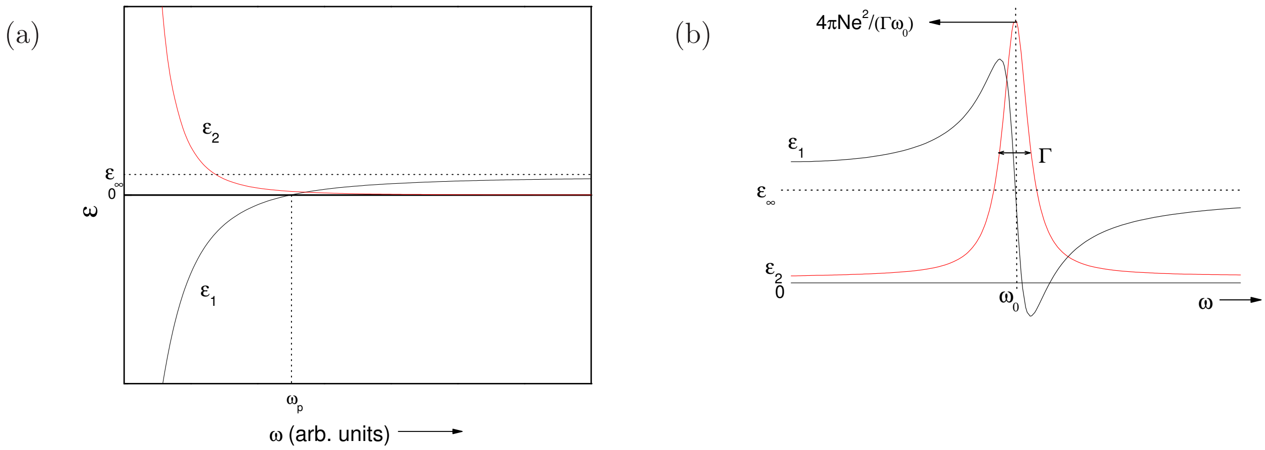

Figure 2.5: *(a) Schematic representation of the spectral dependence of ϵ_1 and ϵ_2 for a free-electron metal described by Drude model. (b) Frequency dependence of the real and imaginary parts of the dielectric function, $\epsilon_1(\omega)$ and $\epsilon_2(\omega)$ for $\epsilon_\infty > 0$.*

resonance frequency of the excitation. The second term of the Eqn.(2.10) corresponds to the Drude term while the last term corresponds to the Lorentz terms. The plasma frequency, defined as the frequency at which ϵ_1 becomes zero, is given by the expression

$$\omega_p^2 = \frac{4\pi N e^2}{m} \quad , \tag{2.11}$$

where N is the number of charge carriers and m is the free electron mass. The dc conductivity (σ_{dc}) can be obtained from the relation

$$\sigma_{dc} = \frac{4\pi N e^2}{m\Gamma} \quad . \tag{2.12}$$

Figure 2.5(a) shows the schematic representation of the real and imaginary parts of the dielectric function of a free-electron metal described by the Drude model. Figure 2.5(b) shows the schematic representation of the real and imaginary parts of the dielectric function described by Lorentz model. The real and imaginary parts of the complex optical conductivity can be obtained from the dielectric function using the relations

$$\sigma_1(\omega) = \frac{\omega \epsilon_2(\omega)}{4\pi} \quad , \tag{2.13}$$

$$\sigma_2(\omega) = (1 - \epsilon_1(\omega))\frac{\omega}{4\pi} \quad . \tag{2.14}$$

2.2.3 Optical conductivity of inhomogeneous media

The study of the optical properties of condensed matter systems with inhomogeneities in submicron scale, reveals anomalous behavior of the optical conductivity that do not occur in the related homogeneous systems. Such phenomena have been observed in several materials like aggregated metallic films, suspensions of metallic particles in a dielectric medium and amorphous compounds [4].

The scattering of light by submicroscopic particles in an inhomogeneous media can be described by the Maxwell-Garnett (MG) theory. This effective medium approximation (EMA) theory takes into account the modification of the applied electric field by the dipole fields of the particles. The result of the MG theory can be obtained from the generalized Clausius-Mosotti equation for spherical metal particles immersed in a polarizable insulator of dielectric function $\epsilon_i(\omega)$ [5]: According to the generalized Clausius-Mosotti equation, the effective dielectric function $\epsilon(\omega)$ is

$$\frac{\epsilon(\omega)-\epsilon_i(\omega)}{\epsilon(\omega)+2\epsilon_i(\omega)}=\frac{4\pi\alpha(\omega)}{3\epsilon_i(\omega)} \quad , \tag{2.15}$$

where $\epsilon_i(\omega)$ is the dielectric function of the insulator and $\alpha(\omega)$ is the polarizability of the medium. Substituting $\alpha(\omega)$ with the expression for the polarizability of the isolated metal sphere, the MG relation can be obtained as

$$\frac{\epsilon(\omega)-\epsilon_i(\omega)}{\epsilon(\omega)+2\epsilon_i(\omega)}=(1-x)\frac{\epsilon_m(\omega)-\epsilon_i(\omega)}{\epsilon_m(\omega)+2\epsilon_i(\omega)} \quad , \tag{2.16}$$

where x is the volume fraction of the insulator and $\epsilon_m(\omega)$ is the dielectric function of the metal.

When the size of the particles are non-spherical, the simple MG theory does not describe the dielectric function of the material reliably. Therefore, the size and shape of the particles have to be included as one of the parameters in the above expression. This gives

$$\frac{\epsilon(\omega)-\epsilon_i(\omega)}{g\epsilon(\omega)+(1-g)\epsilon_i(\omega)}=(1-x)\frac{\epsilon_m(\omega)-\epsilon_i(\omega)}{g\epsilon_m(\omega)+(1-g)\epsilon_i(\omega)} \quad , \tag{2.17}$$

where g is the depolarization factor [5]. The depolarization factor can be calculated depending on the morphology of the particles embedded in the dielectric medium with reasonable approximation [6, 7].

Above equations from the MG theory give rise to a dielectric anomaly and thus influences the optical properties. The anomaly gives rise to a resonance in ϵ_2 at a frequency where $\epsilon_1 \approx 0$. For a simple metal, the anomaly is expected to be observed below the plasma frequency and move to higher frequencies with increasing concentration of the insulator. In real metals, the presence of a finite $\mathrm{Im}\epsilon_m(\omega)$ damps the anomaly, thereby removing the singularity. The intensity of the resulting conduction resonance peak in $\epsilon(\omega)$ is then inversely proportional to $\mathrm{Im}\epsilon_m(\omega)$ and is a function of

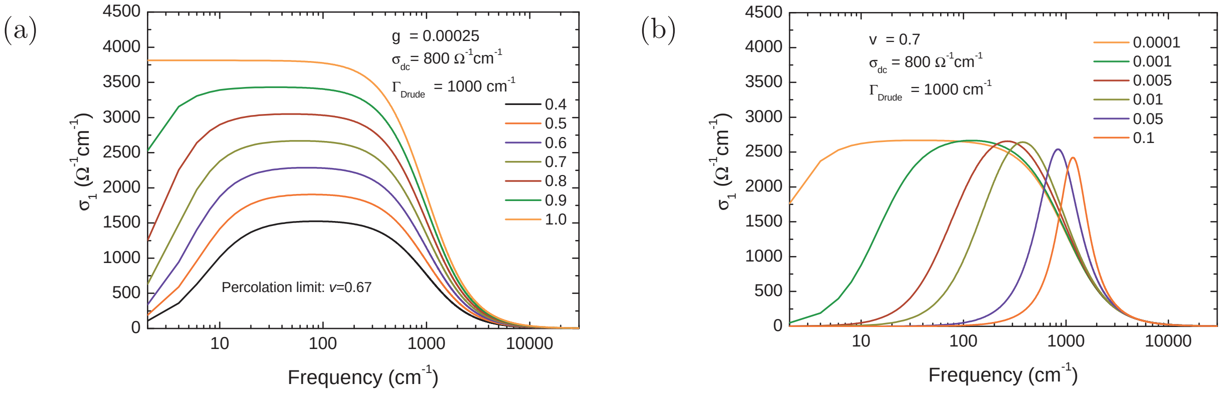

Figure 2.6: *(a) Dependence of the free-electron Drude response on the volume fraction (v) of the metallic particles in the dielectric medium. (b) Influence of the depolarization factor (g) on the frequency response of the Drude parameters. The dc conductivity (σ_{dc}) and damping (Γ) of the Drude term were taken as 800 cm^{-1}and 1000 cm^{-1}, respectively.*

concentration. This is reminiscent of the bulk plasma resonance. Thus, the optical properties of metal aggregates consists of two resonances, namely the plasma resonance and the optical conduction resonance (OCR) [8]. While the OCR can be observed in the optical conductivity, the plasma resonance can be observed only in the electron energy-loss function [5]. For very low concentration of metal particles the frequencies of the two resonances are nearly equal. As the concentration of metal particles tends to unity, the OCR and the plasma resonance shift to lower and higher energies, respectively [8].

The nature of the conduction resonance peak was discussed in detail by Marton and Lemon [8]. Crudely, the resonance frequency is the boundary between the low-frequency insulating behavior, characteristic of the dielectric medium and the high-frequency behavior of the metallic particles embedded in the medium. The model that explains the occurrence of the resonance peak is as follows:

When light is incident on the metal-insulator aggregate system, the small metal particle is located in a periodic local field inside the aggregate system. The free-electrons of the particles respond to the local field by oscillating within the volume of the aggregate. This give rise to a periodic conduction current within the aggregate. At a certain frequency, the phase of the conduction currents in all particles in the aggregate become nearly equal enhancing the local field. When the local currents are exactly in phase with the driving electric field, the conduction resonance occurs.

Thus, the frequency dependence of the optical properties like transmittance, reflectance, absorbance and optical conductivity strongly depends on the concentration and shape of the particles that form the inhomogeneous medium together with an insulating matrix. This means that the measured low-energy response due to the free-electrons in metals, is determined by the concentration and depolarization factor of the particles in the dielectric medium. Simulations which illustrate such dependence of the free-electron response in the infrared frequencies is shown in Figure 2.6. The variation of the frequency dependence of the Drude parameters as a function of the volume fraction ($v = 1 - x$) of the metallic particles and the depolarization factor (g) are shown. It can be seen that the position of the resonance peak strongly depends on the depolarization factor. The longer the particles, the lower is the frequency of the resonance peak [7]. The volume fraction of the insulating and metallic particles also affect the conductivity drastically. In a metal-rich limit i.e., when $x < 0.33$, the conductivity is determined by the percolation through the long metallic particles. This condition which describes the transition from continuous-insulator limit to continuous-metal limit is known as the percolation limit.

Within this work, MG effective medium approximation is extremely useful in describing the infrared frequency spectra of the carbon nanotube films. The carbon nanotube thin films have an inhomogeneous distribution of the bundles of carbon nanotubes which would affect the nature of the measured optical response. The measured transmittance/reflectance spectra of carbon nanotube films were therefore fitted with the Drude-Lorentz model combined with the EMA model to obtain the optical conductivity of the carbon nanotubes from the combined optical response of the nanotube and the dielectric medium in which they are embedded. The details of the analysis of the various carbon nanotube films will be presented in Chapter 4.

2.3 Infrared spectroscopy under high pressure

Infrared spectroscopy under high pressure is performed using a diamond anvil pressure cell. In this section, general characteristics of the DAC and the descriptions of the DACs used within this project are presented. Also, the pressure determination method and pressure transmitting media required for measurements using DAC are explained. In addition, the important information related to the high-pressure IR experiments are described briefly.

2.3.1 Diamond Anvil Cell

The development of the DAC for pressure generation revolutionized the field of high pressure research. DACs are used for combining high pressure technique together with

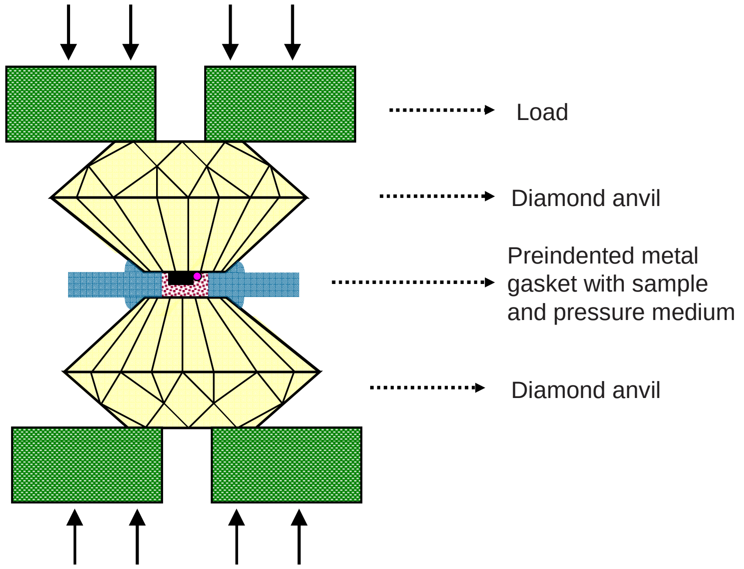

Figure 2.7: *General schematic drawing of diamond anvil cell illustrating its basic operation (adopted from Ref. [9]).*

optical measurements. Optical absorption and reflectivity measurements, and Raman and Brillouin scattering studies at ultra-high pressures have become possible only with the use of DACs. They have a great advantage of exploiting high strength of diamonds with its transparency over the ultraviolet, visible, infrared and X-ray spectral range.

General characteristics of DACs

A general schematic drawing of a DAC is shown in Figure 2.7. It consists of two diamond anvils opposing each other. These diamond anvils are produced from single crystals that are inclusion free and have low birefringence. The diamonds have brilliant cut (8 or 16 faces) and the working plane is produced at the culet. The pressure range in which a DAC can be employed depends on the culet. Flat culets are used for pressure below 100 GPa and beveled culets are used for pressures above 100 GPa. The diamonds rest on support seats with apertures, designed according to the nature of experiments. To reduce the stress concentration at the edges, the aperture has to be as small as possible and the edges rounded. The edge of the diamonds has to be faceted. The operation of DAC is based on the principle that a sample placed between the flat parallel surfaces of two opposed diamond anvils is subjected to pressure when a force pushes the two anvils together.

The three main parts of a DAC are as follows [10]:

- **Anvil-alignment mechanism:** An accurate alignment of the diamond anvils is extremely important before using a DAC due to the brittleness of the diamonds. The working tips of the anvils must be parallel and have equal coincidence diameters. The coincidence of the anvil tips can be achieved by simple translation of the diamonds. The angular alignment of the anvils can be achieved by tilting the anvils until the interference fringes between the opposing diamond culets disappear. An accuracy of parallelism better than 200 nm across the culet is necessary.

- **Sliding system:** A piston-cylinder system is used as the main guiding system in several DACs. The piston should fit very well in the cylinder with a tolerance of ≈ 5 μm to avoid swinging of the diamond anvils.

- **Mechanism of application of load:** There are several mechanism for application of load for pressure generation. Based on the loading mechanism, the DACs can be classified as clamped cell, pneumatic- or hydro-loading cell and lever-arm driven cell.

Thus the differences among various DACs arise from the ways in which force-generation and anvil-alignment mechanisms are designed [11]. Accordingly, five generic types of DACs have evolved. They are:

1. National Bureau of Standards (NBS) cell [12]
2. Bassett cell [13]
3. Mao-Bell cell [11]
4. Syassen-Holzapfel cell [14]
5. Merrill-Bassett cell [15]

Generally, in a high pressure apparatus, the sample is contained in a gasket filled with hydrostatic pressure transmitting medium (more detailed description of pressure transmitting medium is presented in the Section 2.3.3). The gasket is prepared by drilling a hole at the center of a preindented metal disk. Apart from the use as container for the pressure medium and the sample, the gasket acts as a supporting ring, preventing failure of the anvils due to concentrations of stresses at the edges of the anvils. Therefore, the gasket critically determines the pressure distribution in the anvil.

In contrast to the diamonds, the gasket material and structure can be chosen and varied as per the requirements of the experimenter. However, the selection of gasket

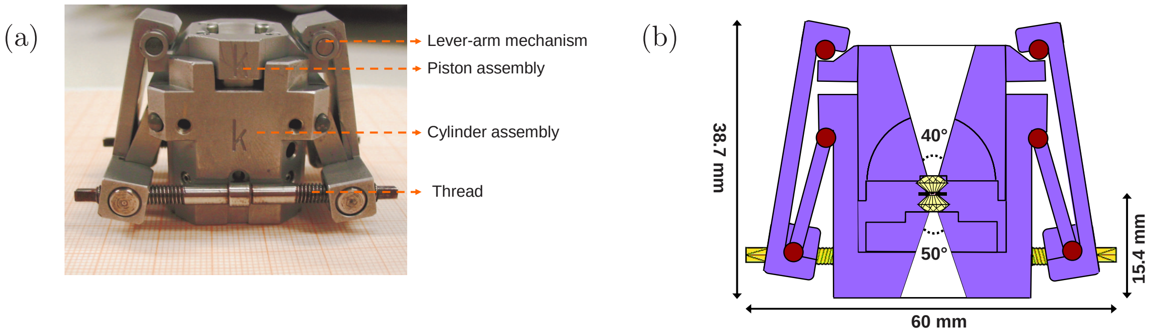

Figure 2.8: *(a) A picture of Syassen-Holzapfel cell showing its main parts and outer construction. (b) A schematic cross-sectional view of the Syassen-Holzapfel pressure cell showing the inner construction. The dimensions of the cell are also indicated.*

dimensions is very crucial. The basic working of gasket has also been studied theoretically [16]. The part of the gasket between the culets undergoes plastic deformation as the diamonds advance and is extruded. The hydrostatic pressure within the metal decreases linearly in the direction of extrusion. The gradient of pressure increases as the gasket becomes thinner. The extrusion may be entirely outwards or may be inwards. The choice of gasket thickness and the diameter of the sample hole also depend on the hydrostatic pressure medium used. For relatively incompressible pressure media, the hole may be one-third or two-fifth of the culet diameter. For compressible medium like helium, the hole may be made larger as the hole shrinks by a factor of two or more after loading of pressure medium.

Although different pressure ranges have different requirements there are some simple scaling rules. The maximum load applied to the diamonds is about one ton independent of the pressure range [17]. The culet diameter is then proportional to the square root of the pressure range. The pressure gradient in the gasket from the edge inwards is inversely proportional to the thickness and so the gasket initial thickness must be proportional to $P^{-3/2}$. The constant of proportionality for the thickness includes the shear strength of the metal and the higher the elastic yield strength of the metal, the thicker the gasket may be for a given pressure.

Hence, optimum dimensions and parameters of a diamond anvil cell should be chosen based on the requirements of the desired pressure experiments. In the following subsections, a detailed description of the pressure cells used within this project will be presented. A Syassen-Holzapfel type piston-cylinder clamped cell and a cryoDAC Mega clamped cell with large culets obtained from *easylab*, were used within this project.

Syassen-Holzapfel-type DAC

The Syassen-Holzapfel type diamond anvil cell is a clamped piston-cylinder cell developed by Huber, Syassen and Holzapfel [14]. Figure 2.8 shows (a) Syassen-Holzapfel DAC and (b) its cross-sectional view. One of the diamond anvils is mounted in a X-Y translational stage incorporated in a fixed backing plate. The other diamond is mounted on a tilting stage in a moving piston. The force for compressing the anvils for pressure generation is produced by a thread-and-knee mechanism. A simple gear-set wrench synchronously turns two threaded rods which connect the front and back sides of the brackets and pulls the lower ends of the brackets together. Thereby, the distance between the upper ends of the brackets decreases compressing the moving piston to generate pressure. The special geometry of this construction results in large force multiplication. Due to the presence of long piston and good fit combined with thrust acting strictly parallel to the axis of the device, this DAC has excellent alignment stability.

The Syassen-Holzapfel DAC used within this project has a height of 38.7 mm and a length of $\approx$ 60 mm. The diamond anvils are made of type-IIa diamonds with height of 1.5 mm and culet diameter of 400 μm. The maximum pressure that can be generated in this DAC is around 25 GPa. The opening angle of the apertures at the piston and the cylinder assemblies are 40° and 50°, respectively, to minimize signal loss. A gasket made from stainless steel with initial thickness 0.25 mm is used in this DAC. Holes with diameter of about 150-200 μm were drilled in the gaskets pre-indented to a thickness about 70-80 μm, for measuring at pressures up to 10-15 GPa.

CryoDAC Mega Clamp cell

The diacell cryoDAC Mega from *easylab* is a non-magnetic clamp cell made of CuBe alloy. It is suitable for optical and X-ray diffraction studies at cryogenic temperatures. The DAC consists of a piston-cylinder assembly mounted within two CuBe blocks. Figure 2.9(a) shows the disassembled cryoDAC mega for clear view of the various parts of the pressure cell. The DAC assembly fits into the CuBe blocks such that there will be no distortion of the piston-cylinder movement even at the highest loads. Both piston and cylinder are fixed to the CuBe block by means of screws. One of the CuBe block holds the DAC in its groove while the other block fits over the DAC and is used to apply load to the cell by means of four cap head bolts.

The cross-sectional view of the DAC is shown in Figure 2.9(b). One diamond anvil is located at the bottom of the cylinder mounted upon a tungsten carbide support plate. This assembly is retained by a clamping plate which can be translated normal

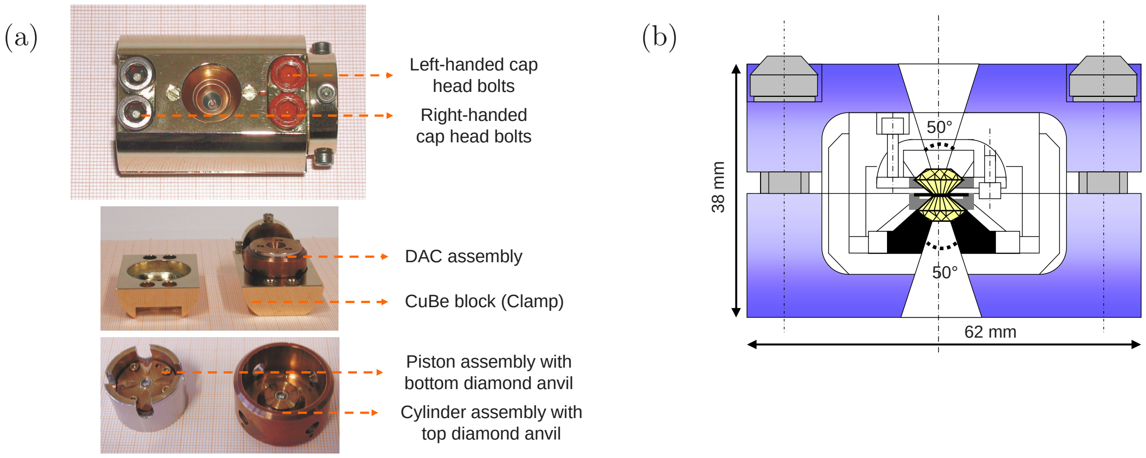

Figure 2.9: *(a) A picture of the clamp cell CryoDAC showing its main parts. (b) A schematic cross-sectional view of the CryoDAC illustrating the inner construction. The dimensions of the cell are also indicated.*

to the cylinder axis by means of the lateral adjustment screws. The other anvil is held similarly on its carbide support plate, and is located within a hemisphere which carries three screws for tilt adjustment of the anvil culets relative to each other.

The diameter of the complete pressure cell assembly is 38 mm. The diamond anvils have height of 1.5 mm and culet diameter of 800 μm. The opening angle of the apertures in this DAC is 50° at both the piston and cylinder assemblies. The maximum pressure that can be achieved in this DAC is about 12 GPa. The gaskets used together with this DAC are made of CuBe alloy with a thickness of 0.4 mm. The gaskets are preindented to a thickness of about 100 μm and drilled with holes of diameter 400 μm for applying pressure up to 8 GPa.

2.3.2 Pressure determination method

The ruby luminescence method is the most commonly used method for pressure determination in high pressure experiments using a DAC. Although pressure standards were used earlier, ruby luminescence proved to be the most convenient for DAC. It can also provide indications about the hydrostaticity of the pressure medium. In this section, a brief description of the principle of ruby luminescence method and experimental realization of this pressure determination technique is presented.

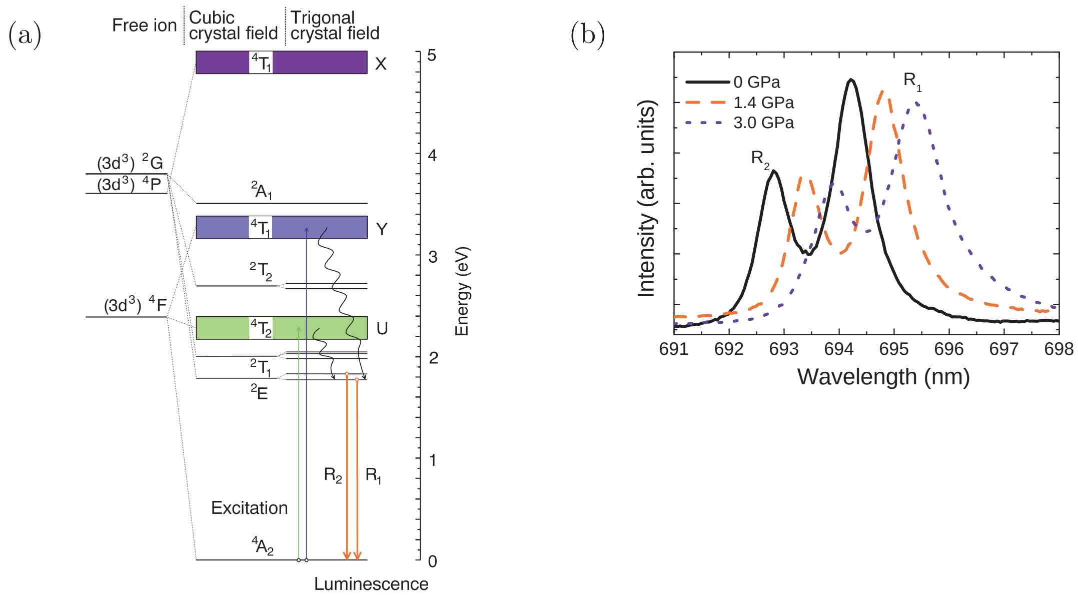

Figure 2.10: *(a) The crystal field splitting of* Cr^{3+} *in ruby. The absorption and emission processes of* R_1 *and* R_2 *transitions are also indicated [22]. (b) Typical spectra of ruby luminescence of* R_1 *and* R_2 *lines for various pressures at room temperature are shown.*

Principle of ruby luminescence

Ruby is α-Al_2O_3 doped with Cr. The Cr^{3+} ions replace Al^{3+} ions which are six-fold coordinated by oxygen. Since Cr^{3+} has slightly larger ionic radius than Al^{3+}, doping with Cr induces trigonal distortions in the crystal. The ligand field energy levels of Cr^{3+} in ruby is shown in Figure 2.10 (a). The ground state of the Cr^{3+} ion ($^4A_2$) and its excited state (^2E) are split into a pair of Kramers doublets, 0.38 cm^{-1} apart in the ground state and 29.14 cm^{-1} apart in the excited state [18–21]. This splitting of the cubic field states is due to the combined action of the spin-orbit coupling and the trigonal distortion of the oxygen octahedra.

When Cr^{3+} is excited by a laser either in green or in the violet (see Figure 2.10 (a)), the metastable states are populated by fast non-radioactive decay. Subsequently much slower radiative transitions takes place in particular from the metastable ^2E doublet state to the ground state giving rise to the R lines. The R_1 and R_2 lines of ruby are therefore two closely spaced lines at the extreme red end of the visible spectrum which occur at the same wavelengths in absorption and emission.

The frequencies of the R lines are very sensitive to pressure and temperature, and the shift of the R lines with respect to changing temperature and pressure can be used for pressure determination at a given experimental condition [23–27]. The pressure- and temperature-induced wavelength shifts are usually assumed to be independent of

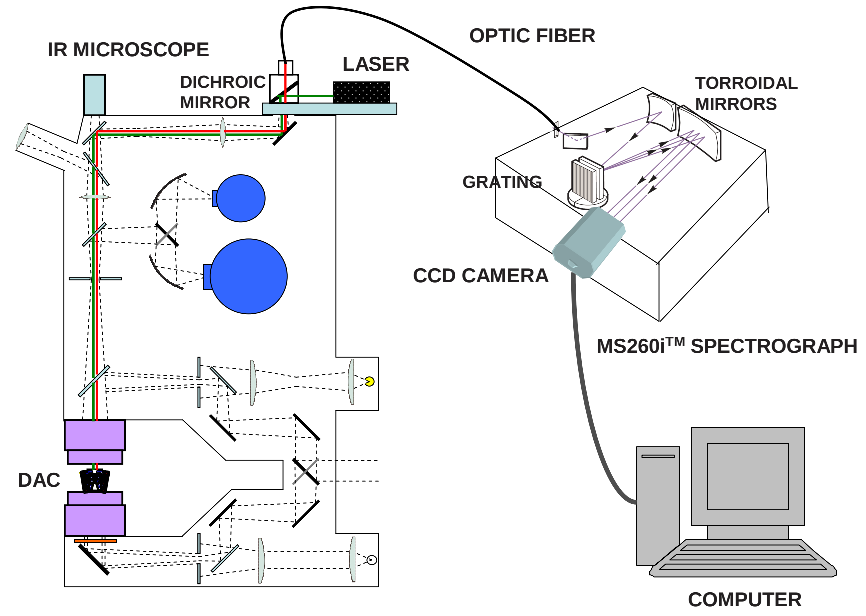

Figure 2.11: *General schematic drawing of ruby luminescence spectrometer coupled to the IR microscope.*

each other. The ruby pressure calibration at room temperature, that is used within this project, was given by Mao *et al.* taking into account the non-linearity in the pressure-induced shifts of the ruby R_1 line [27]. The relation is:

$$P(\Delta\lambda) = \frac{A}{B}\left[\left(1+\frac{\Delta\lambda}{\lambda_0}\right)^B - 1\right] \tag{2.18}$$

where $\Delta\lambda$ is the wavelength shift of the R_1 line with pressure and λ_0 refers to the wavelength at zero pressure (694.25 nm at 298 K). The parameters are A=1904 GPa and B=7.665.

The pressure dependence of the ruby R_1 line is shown in Figure 2.10(b). It can be observed that the pressure-shifts are quite large and the frequency of R_1 can be determined easily and accurately. Thus, by measuring the frequency of the R_1 luminescence line from a ruby ball placed next to the sample in a DAC at a given temperature, the pressure generated in the sample space of the DAC can be determined.

Ruby luminescence arrangement

In order to accurately measure the pressure generated in the DAC during the experiment, a high resolution charge coupled device (CCD) spectrograph coupled to the IR microscope is employed. This facilitates in-situ measurement of pressure in the DAC without having to remove the pressure cell from the microscope.

The main components of the ruby luminescence arrangement are the excitation laser and CCD spectrograph. Figure 2.11 shows the schematic drawing of the ruby luminescence arrangement coupled to the IR microscope illustrating the luminescence measurement configuration[1]. The ruby ball placed in the DAC is excited by the light of wavelength 532 nm produced by the diode-pumped solid-state laser with a power of 10 mW transmitted through a dichroic mirror. The dichroic mirror reflects light of wavelength in the range 500-580 nm and transmits light with other wavelengths. Thus, the luminescence spectrum from the ruby is transmitted to the CCD spectrograph through the mirror and an optical fiber coupling the output from the microscope to the spectrograph.

The CCD spectrograph is a commercial MS260i^{TM} grating-type imaging spectrograph. It consists of an asymmetrical in-plane Czerny-Turner optical configuration with unequal entrance and exit focal lengths of 220 mm and 257 mm, respectively (see Figure 2.11) [28]. The grating of this spectrograph consists of 1800 lines/mm. A set of computer optimized toroidal mirrors produce accurate images of the input slit in the flat output plane. The spectrograph has a excellent spatial resolution of 40 μm. The signal at the exit slit is then detected by a CCD camera. The detection element of the CCD camera has 1024×127 pixels in an area of 26×26 μm^2. The accuracy of pressure determination using this ruby luminescence arrangement is 0.1 GPa.

2.3.3 Pressure transmitting media

The function of a pressure transmitting medium is to translate the uniaxial thrust that is imposed up on it in a high-pressure apparatus into a stress which acts as uniformly as possible on the sample under investigation. The role of a pressure transmitting medium in high pressure experiments can be illustrated as shown in Figure 2.12. The choice of the pressure medium which performs this role is limited by the nature of the experiments to be performed. For example, in optical transmission experiments the medium must have high transmission in the spectral regions of interest, while in electrical measurements the medium should be an insulator. An ideal pressure transmitting medium should have the following properties [29]:

- Zero shear strength
- Chemically inert

---

[1] The optical configuration of CCD spectrograph was adapted from information manual of MS260i imaging spectrograph.

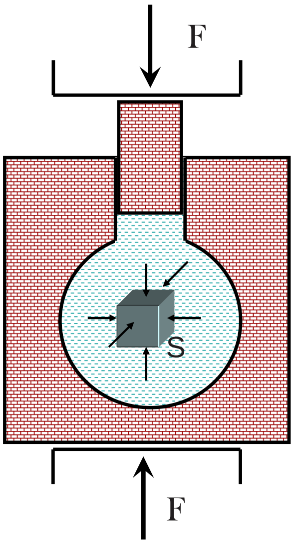

Figure 2.12: *Schematic representation of the role of the pressure medium in a high pressure apparatus. The uniaxial thrust F is transformed by the pressure medium into a uniform stress acting on the sample S (adopted from Ref. [29]).*

- Zero penetration into the sample or the materials used in the construction of the high pressure apparatus
- Zero compressibility
- Easy to handle
- Easy to seal within the high pressure closure
- Excellent hydrostaticity

The pressure transmitting media are generally classified as solid, liquid and gases referring to their states under ambient conditions. The hydrostaticity of the pressure transmitting medium in a DAC can be estimated experimentally in one of the following ways, by measuring

1. the pressure gradient in the medium across the anvil;
2. the full width at half maximum (FWHM) of the ruby luminescence lines;
3. splitting between the ruby R_1 and R_2 lines;
4. lattice parameters of the crystal relative to the loading direction and relating this to the stress component.

In the following subsections, the solid and gaseous pressure transmitting media used within this thesis work are explained.

Solid pressure transmitting media

Solid pressure transmitting medium is the easiest to use. The hole in the gasket can be filled with the solid medium and slightly prepressed so that the medium is compactly packed in the gasket hole. The most commonly used solid pressure transmitting media are soft alkali halides like KBr, KCl, CsI, NaCl, and other materials like teflon, polyethylene. Solid media are used in the DAC particularly when the sample has to be in direct contact with the anvil. Hence, the reflectivity measurements on oriented carbon nanotube films presented in this work could be performed only with the use of solid pressure transmitting medium. CsI was used as the pressure transmitting medium in the all measured frequency ranges (FIR-visible ranges), while both CsI and KCl were employed for IR spectroscopic measurements on powder samples of fullerene-based compounds, C_{70}, C_{60}-C_8H_8 and C_{70}-C_8H_8, in FIR-visible frequency ranges.

Gaseous pressure transmitting media

The advantage of using a gas as a pressure transmitting medium lies in the exceptional low viscosity that it exhibits. Another important advantage of gaseous pressure transmitting media is the ability to use them at low temperatures. Gases Xe, Ar, He and H_2 are excellent pressure transmitters and can be used as pressure media in $\sim$100 GPa range. The most popular choices have been nitrogen, helium and argon. Argon is considered to be hydrostatic up to 9 GPa [10]. Above these pressure values, the pressure transmitting media become more non-hydrostatic. A pressure difference of 1.7 GPa across an argon sample was observed at $\approx$75 GPa [27]. Due to the high compressibility of gases, typically, it requires a volume ratio of about 800:1 to bring an ambient gas up to its liquid density. Therefore, it is not feasible to load gaseous pressure medium within the gasketed DAC under ambient conditions. Loading of the ambient gas pressure transmitting medium into the gasket hole in the DAC can be either by cryogenic-filling [30,31] or by high-pressure gas loading [32,33].

Most of the high pressure transmission measurements on carbon nanotube samples within this project have been performed using argon as the pressure transmitting medium. Some pressure-dependent measurements on rotor-stator compounds in the NIR-visible frequency range were also performed using argon as pressure medium for checking hydrostaticity effects. A home-built cryogenic-filling setup for argon was used for this purpose. Figure 2.13 shows the schematic diagram of the argon-filling setup for the Syassen-Holzapfel type DAC used in this project. A similar arrangement is used for the CryoDAC Mega cell with adaptations to accommodate the differences in the way the load is applied (see Section 2.3.1 for detailed information on the construction

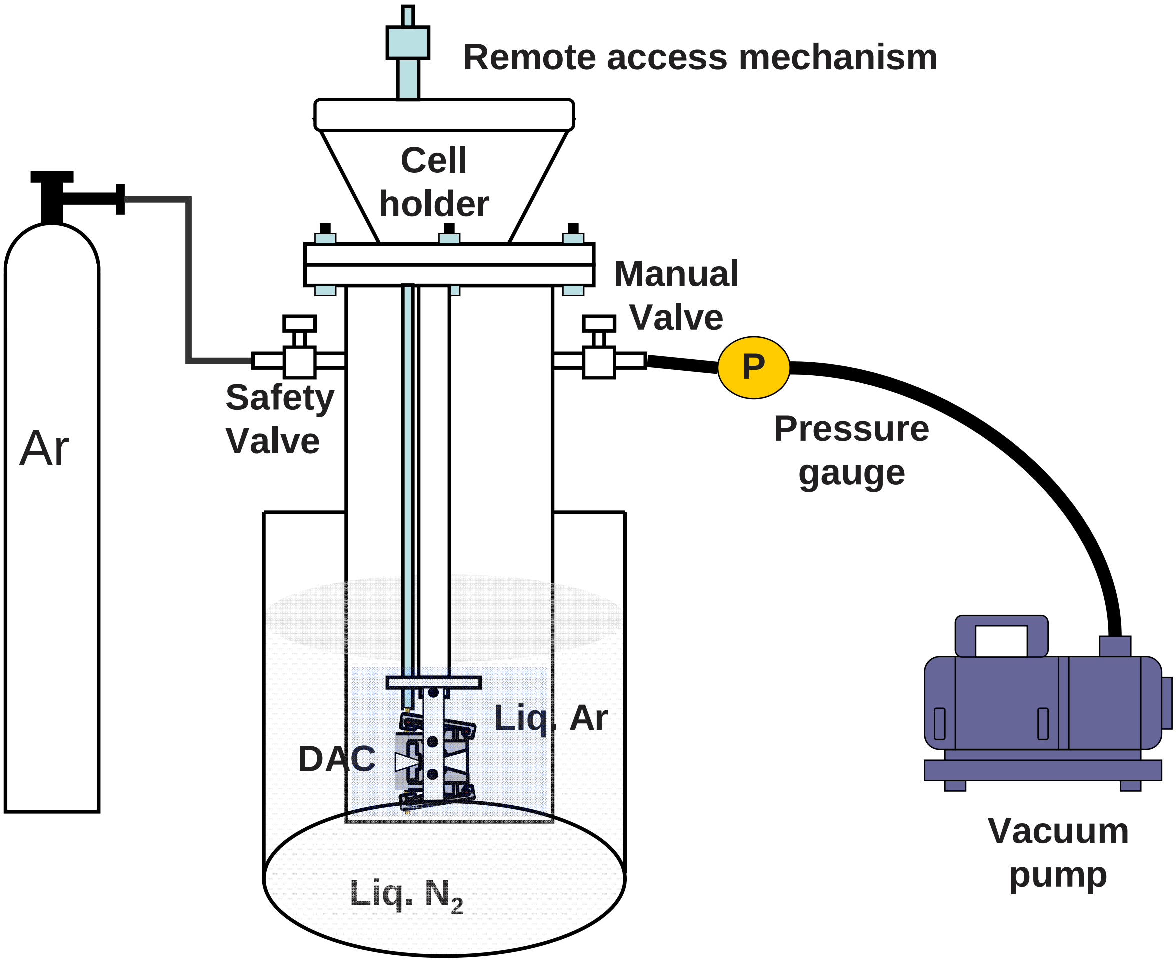

Figure 2.13: *General schematic drawing of experimental arrangement for cryogenic loading of argon in Syassen-holzapfel type DAC.*

of the DACs used in this project). Briefly, the argon filling can be done as follows: The vessel is purged with argon several times and continuous argon flow is maintained with slight over-pressure. The vessel is then cooled with liquid nitrogen and placed in the liquid nitrogen bath. The flow of argon is then regulated such that there is a constant under-pressure of about 0.8 bar maintained in the vessel. The pressure in the vessel shoots up (> 0.1 bar). During this process, the argon liquefies and flows into the DAC. The DAC is then sealed with the aid of a remote access mechanism provided in the cell holder.

2.3.4 IR measurements with a diamond anvil cell

Realization of an infrared measurement under pressure by interfacing a DAC with an infrared spectrometer is not a trivial issue. The problem of obtaining standard foci of micrometer sizes has been solved by the use of an IR microscope coupled to the FTIR spectrometer. However, there are several other factors that have to be tackled in order to obtain a good IR measurement using a DAC. In this section, details related to IR spectroscopy under high pressure like IR properties of diamond, measurement configuration, and the limitations are explained. Both reflection and transmission measurements have been performed within this project.

Optical properties of diamond

In order to perform IR measurements, DACs employ type-IIa diamonds which do not contain nitrogen impurities and are insulating. The refractive index (n_{dia}) is 2.38 at 800 cm^{-1}. The dispersion of the refractive index of diamond is very small in the IR range (see Figure 2.14). The changes in the refractive index of diamond with increasing pressure is about -0.00052 /GPa [34]. Therefore the frequency and pressure dependence of n_{dia} and R_{dia} can be safely neglected. The normal-incidence IR reflectance at the surface of diamond in air is given by

$$R_{dia} = \left[\frac{n_{dia}(\omega) - 1}{n_{dia}(\omega) + 1}\right]^2 \tag{2.19}$$

The value of R_{dia} corresponding to the refractive index of 2.38 is 0.1667.

Due to the high refractive index of the diamonds, reflection losses generally occur at each of the four diamond surfaces. The ratio (r_0) of intensity (I_t) reflected at the top surface to the intensity (I_b) reflected at the bottom surface of a diamond anvil is shown in Figure 2.15(a). The theoretical estimation of r_0 when diamond absorptions are negligible is ≈ 0.694. However, the experimental ratio in the FIR is about 0.74. There is also a modulation superimposed on the ratio (indicated by arrows

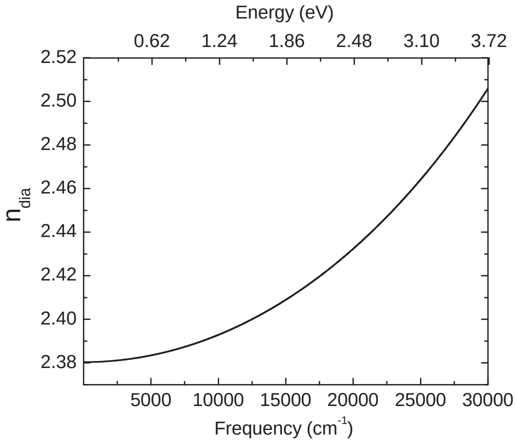

Figure 2.14: *Dispersion of refractive index of diamond in the infrared frequency range* [35].

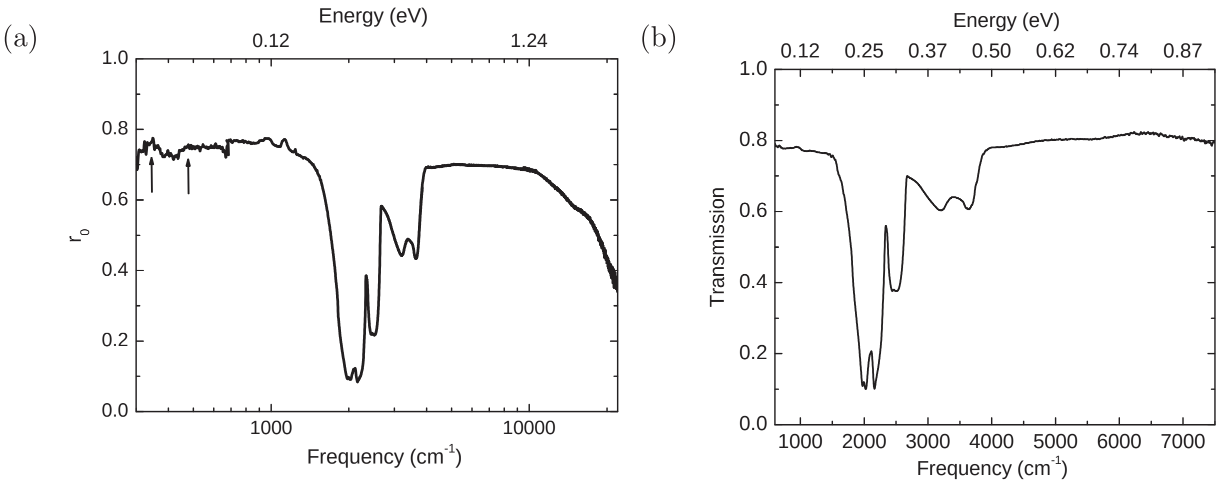

Figure 2.15: *(a) Ratio (r_0) of intensity reflected from the bottom surface of the diamond anvil with respect to the intensity reflected from the top surface of the diamond. It is considered to be nearly constant up to 12000 cm^{-1}. The black arrows indicate the modulations superimposed on the spectrum due to diffraction and/or interference effects. (b) Transmission of the diamond in the MIR range. The strong feature in the reflection and transmission spectra between 1800 $cm^{-1}$and 4000 $cm^{-1}$are due to multi-phonon excitations.*

in Figure 2.15(a) due to diffraction and/or interference effects. The ratio of the IR light reflected from the bottom and top surfaces of the anvil in MIR is around 0.72. The ratio decreases significantly in the visible frequency range from its nearly constant value. This is due to the small dispersion of the refractive index of diamond starting from this frequency range. The transmission of the diamonds is shown in Figure 2.15(b). The refractive index also gives further losses as the optical path length is longer than in vacuum. The diamonds absorb and reflect in the range 1800-2670 cm^{-1}and partly up to 4000 cm^{-1}(see Figure 2.15). This dominant feature in the absorption and reflection spectra of diamonds is due to multi-phonon excitations and has to be discarded during the analysis of the measured spectra.

IR reflectivity at high pressures

One of the general configurations for quantitative reflectivity measurements is shown in Figure 2.16(a). The sample in this case is placed in direct contact with the diamond surface. As mentioned earlier in Section 2.3.3, use of a solid pressure medium is necessary to keep the sample in contact with diamond. For every spectrum (I$_s$) of the sample measured at the sample-diamond interface, a reference spectrum (I$_b$) is measured on the bottom surface of the diamond at the diamond-air interface. Ideally, the ratio of these intensities when multiplied by R$_{dia}$ yields the reflectance of the sample-diamond interface given as

$$R_{s-d}(\omega) = \left[\frac{I_s}{I_b}\right] R_{dia} \tag{2.20}$$

However, the intensity reflected from bottom surface of the diamond can be measured only at the end of the measurement. Therefore, it is important to measure the ratio of intensities reflected from the top surface of the diamond $(I_t/I_{t'})$ for compensating any instabilities like that of source and detector, arising during the course of the experiment (see Figure 2.16(a)). The fact that measured quantity is reflectivity of the sample with respect to diamond should be taken into account while analyzing the measured results. Within this project, reflectivity measurements under pressure were performed for the magnetically-aligned oriented nanotube films.

IR transmission at high pressures

The general configurations for transmission measurement are illustrated in Figure 2.16 b. Measurements may be performed in two different ways according to the sample form: (i) In the case of thin films or bulk samples, the cell loading procedure does not differ from that for the reflectivity measurements. (ii) If the sample is a powder, as it was

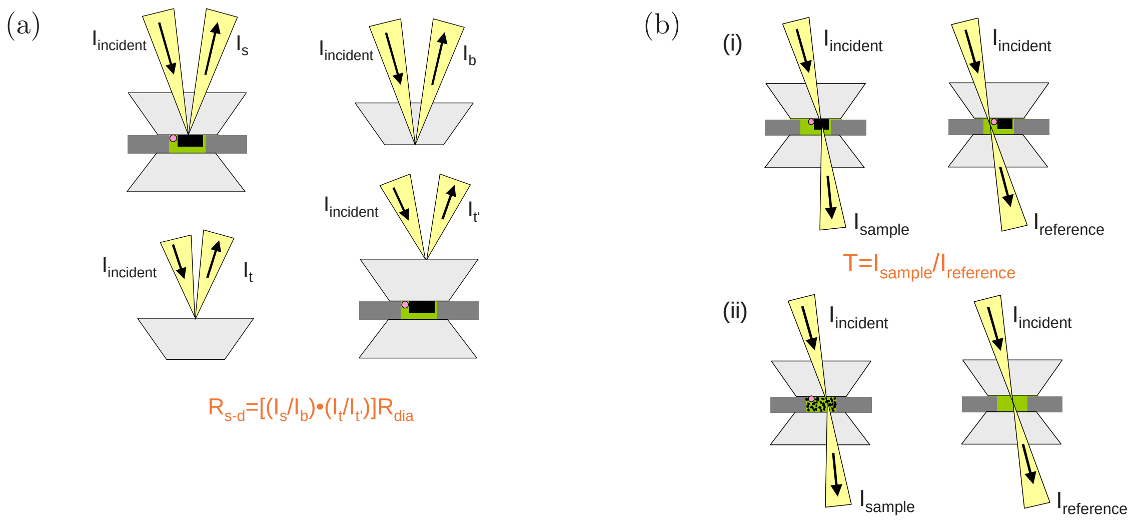

Figure 2.16: *(a) Schematic representation of the measurement configuration for obtaining the various quantities required for calculation of reflectance of a sample at the sample-diamond interface in a DAC. (b) Sketch of the measurement configuration for obtaining the transmission of a sample in a DAC*

the case of fullerene-based compound studied within this project, a matrix containing sample and pressure medium used for obtaining transmission through sample, while light transmitted through the pure pressure transmitting medium is used as reference. In some measurements on the powder samples, the powder sample was placed on the one half of the gasket hole area before filling with the pressure medium, in order to measure the reference spectrum for each measured pressure (see Figure 2.16 b). The transmission of the sample in DAC and subsequently the absorption of the sample can be calculated as

$$T = \frac{I_{sample}}{I_{reference}} \tag{2.21}$$

$$A = -log_{10}T \tag{2.22}$$

where I$_{sample}$ is the intensity of light transmitted through the sample in the DAC while I$_{reference}$ is the intensity of light transmitted through the pressure medium within the DAC.

Another important issue in a transmission measurement using a DAC is the problem of interference fringes. These interferences are caused by a sample with plane-parallel surfaces and/or by multiple reflections within the DAC. The interferences pose some problem in the transmission measurements especially when they mask certain spectral features like vibrational modes in the IR spectra. However, it is quite difficult to get rid of these interferences as they are pressure dependent. Most of the IR measurements within this project were performed in transmission configuration due to the nature of the samples. The unoriented nanotube films, oriented nanotubes in polyethylene matrix and fullerene materials were investigated by transmission measurements.

Working close to diffraction limit

The high pressure IR measurements using microspectroscopy have to deal with the non-trivial problem of working at wavelengths close to the diffraction limit, especially while performing measurements in the FIR range. The resolution limit due to diffraction is given by Rayleigh's relation as

$$\Delta r = \frac{0.66\lambda}{sin(\Theta/2)} \tag{2.23}$$

where Δr is the lateral resolution, λ is the wavelength of light and Θ is the full opening angle of the objective [36]. Using this relation, the limit of the sample and spot size that is required for obtaining a reliable IR spectrum can be estimated. Such an estimate using the full opening angle (40°) of the Syassen-Holzapfel cell, yields a limit of 150 cm^{-1} for a sample size of about 100 μm. The frequency limit becomes larger in reality. Experimentally, it is quite difficult to obtain a good spectrum in the frequency range below 300 cm^{-1} in a DAC especially those with higher maximum pressure limit. It is obvious that the size of samples in DACs is greatly limited by the diameter of the culet and the gasket hole. Therefore, for the FIR measurements on carbon nanotubes under high pressure performed within this project, samples of maximum possible size (at least 200 μm) were used in the CryoDAC Mega pressure cell with a culet diameter of 900 μm.

2.4 Infrared spectroscopy at synchrotron radiation facility

A part of the IR measurements under pressure, more specifically the measurements on oriented SWCNT films in the FIR range, were performed at the synchrotron radiation facility, Angstroemquelle Karlsruhe (ANKA) at Karlsruhe, Germany. The advantages of a synchrotron light source over conventional IR sources are:

- Covers a broader spectral range providing a continuous source from FIR to visible frequency range.
- Provides higher photon flux in the FIR range.

- Offers high brilliance.

In this section, a short explanation on the synchrotron radiation, ANKA synchrotron radiation facility and the infrared beamline at ANKA is presented.

Introduction to synchrotron radiation facility

The synchrotron radiation is emitted by the electrons when they are accelerated to relativistic energies by a microwave cavity and then kept in a circular path by a magnetic field (**B**) by the Lorentz force given as,

$$\mathbf{F} = e \cdot \mathbf{v} \times \mathbf{B} \tag{2.24}$$

The radius (R) of the circular path and the rotational frequency (ω) are given as

$$R = m_0 \cdot \mathbf{v}/e\mathbf{B} \tag{2.25}$$

and,

$$\omega = (e/m_0)\mathbf{B} \tag{2.26}$$

respectively, where m_0 is the free electron mass, **v** is the velocity of electron and e is its charge.

The electromagnetic radiation is emitted in all directions except the direction of acceleration. However, when the relativistic electrons in a synchrotron travel through a bending magnet, the radiation is folded into a narrow cone around the motion direction with an half width of $1/2\gamma$ where γ is the ratio between the relativistic mass of electron and its rest mass. In the plane of the orbit, the emitted radiation is linearly polarized. The power emitted from a synchrotron radiation is given by [37],

$$P = \frac{2e^2c}{3R^2}\left[\frac{E}{m_0c^2}\right]^4 \tag{2.27}$$

where E is the energy of the electron, R is the radius of the circular path and c is the speed of light. The spectral distribution of the emitted radiation is a continuum. However, there exists a critical photon energy (E_c) above which the energy distribution decays rapidly. This critical photon energy in practical units is given as [37],

$$E_c = 665 \cdot E_e^2[GeV] \cdot B[T] \tag{2.28}$$

The storage ring is generally operated at an energy of 2.5 GeV with a typical beam current of 200 mA and lifetime of around 20 Hrs.

The three parameters which characterize a synchrotron beam are:

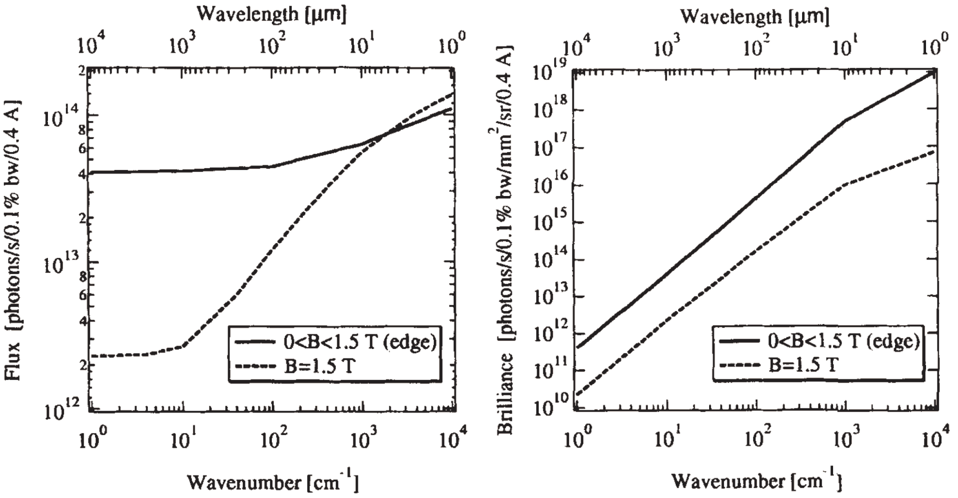

Figure 2.17: *Spectral flux and brilliance of the bending magnet edge source (solid line) are plotted as function of energy in comparison to the central homogeneous source (dashed line)* [38].

- Flux: Photon flux (F) at any given wavelength is defined as a number of photons, which are emitted per second in a spectral bandwidth of $d\lambda/\lambda=10^{-3}$ in an opening angle of 1 mrad. F(photons/s/mrad/(dλ/λ))$\propto$ I(A)·E(GeV)
- Brightness: It is defined as the photon flux per solid angle impinging on to the sample. B(photons/s/mrad^2/(dλ/λ))$\propto$ I(A)·E^2(GeV^2)
- Brilliance: It is the photon density in the image point per solid angle in a spectral bandwidth of $d\lambda/\lambda=10^{-3}$. Brilliance is a function of the area of the optical source.

ANKA-IR beamline

It can be recalled from the previous section that the radiation from a synchrotron has a wide spectral range covering the IR, visible light, UV, soft and hard X-ray regimes. The ANKA-IR beamline uses IR radiation extracted from the leading edge of a dipole bending magnet. The edge radiation is generated over a length of about 10 cm along the electron path. Dipole radiation which is produced when relativistic electrons travel in the homogeneous magnetic field of the bending magnet, is superimposed on the edge radiation. The advantage of using edge radiation is that its spatial distribution is much narrower than that of radiation emitted from the homogeneous part of a dipole magnetic field. Also, the flux and the brilliance of the edge source is much higher

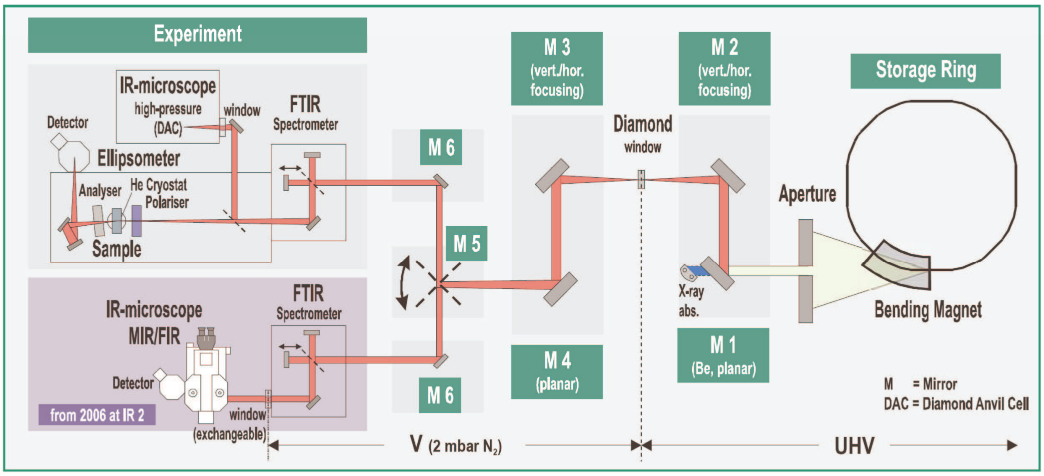

Figure 2.18: *Schematic layout of the IR beamline at ANKA* [39].

than that of the homogeneous field source. Figure 2.17 shows the spectral flux and brilliance of the edge source compared to the central source. It can be seen that the spectral flux and the brilliance of the edge source is at least one order of magnitude higher than that of the central source in the IR frequencies.

The layout of ANKA-IR beamline is shown in Figure 2.18. The IR radiation from the extracted from the storage ring passes through a wedged 1 mm thick diamond window. A slow vacuum valve isolates the vacuum system of the IR beamline from the ultrahigh vacuum of the storage ring. The IR beam enters the FTIR Bruker IFS66v/S coupled to a IR microscope (for more details see Sections 2.1.2 and 2.1.3). The diffraction-limited diameter of the beam spot at the sample in the IR microscope is ≥ 10 μm.

An important aspect that needs to be considered while using synchrotron radiation as the light source for measurements is that the beam current decays with time. Therefore, the measured spectra have to be normalized with the beam current with the help of the actual current information during the collection of a spectrum which is available in a log file. In the transmission measurements performed at ANKA IR beamline, the reference spectra were measured for every pressure step directly after the measurement of the sample. Therefore, normalization of the transmission spectra was not required. On the other hand, the normalization of the measured spectra according to the beam current was done for the reflectivity measurements on magnetically-oriented nanotube film. Additionally, the reflectivity measurements were normalized with the ratio of intensities reflected from the top surface of the diamond anvil to account for instabilities in the synchrotron beam (see Section 2.3.4 for more information).

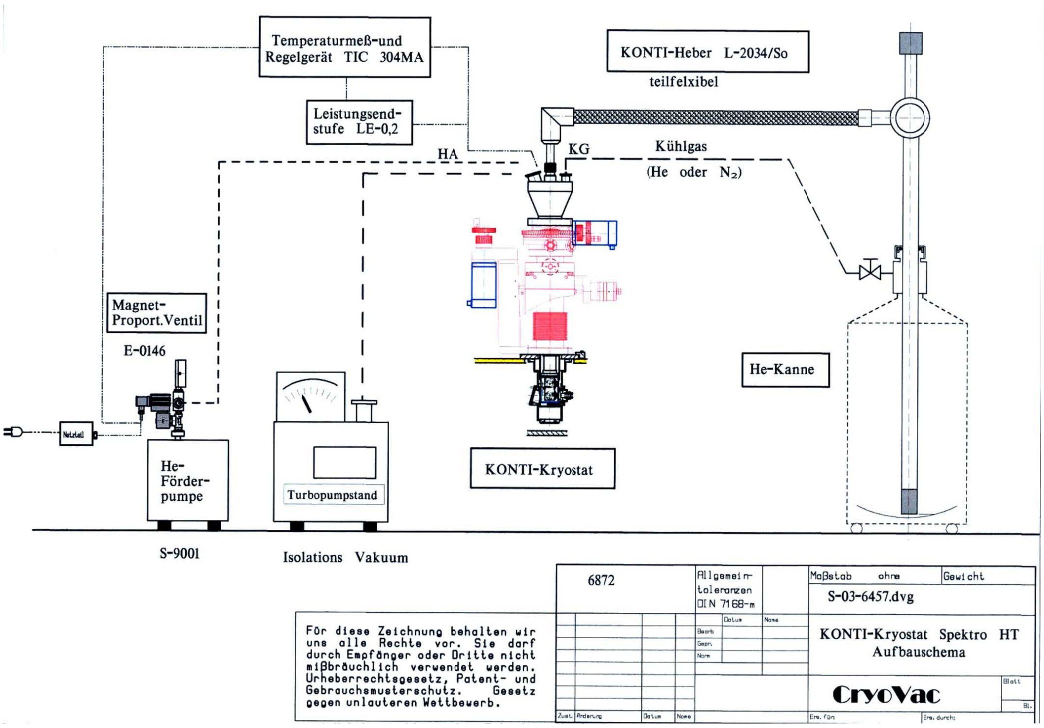

Figure 2.19: *Sketch of the arrangement of the cold finger cryostat and the corresponding equipment* [40].

2.5 Infrared spectroscopy at low temperatures

The temperature-dependent IR spectroscopy on both unoriented and oriented carbon nanotube films were performed using a Cryovac liquid helium cryostat. In this section, a short description of this cryostat and its operation is presented.

The cold finger cryostat is a flow-type cryostat with liquid helium supply from an external tank. The operating temperature range of the cryostat is 5 - 500 K. The required temperature is achieved through the use of a heat exchanger mounted on the bottom of the experimental chamber. Liquid helium is fed from the helium can to this heat exchanger through a narrow stainless steel tube with the help of a vacuum pump. The helium flow is regulated through a fine needle valve on the transfer tube and a magnetic proportional valve at the back-flow side of the cryostat. The magnetic proportional valve and the heater situated close to the sample holder are controlled by a temperature controller. The basic sketch of the cryostat operation arrangement is shown in Figure 2.19.

The optical tail of the cryostat consists of four flanges on its sides to enable reflection and transmission measurements. The optical window for the incident light, fixed at one of these flanges, is positioned at a certain angle to avoid window reflections reaching the detector. The sample holder is provided at the bottom of the heat exchanger and surrounded by two Cu radiation shields. The movement of the sample holder in the horizontal plane for adjusting the focus of the incident light can be performed by manual micrometer screws. The sample holder can be moved up and down with the help of a stepper motor interfaced to the computer through a positioning controller. This facilitates better alignment of the sample. Another stepper motor enables rotation of the sample holder up to 360° and is used to rotate the sample holder. These stepper motors allow movement of the sample and the reference to the measurement position.

The temperature-dependent measurements on unoriented carbon nanotubes films were performed over a very broad frequency range from 50-20000 cm^{-1}. The measured frequency range was extended to lower frequencies down to 6 cm^{-1} for room temperature spectra using a THz spectrometer at Physikalisches Institut 1, Universität Stuttgart. This extension to lower frequency were made possible due to the large size ($\approx$ 1 cm diameter) of the samples available. The temperature-dependent measurements on magnetically-oriented nanotube films were performed from MIR to visible range. Measurements at low frequencies were limited by the dimensions of the sample. The sample size $<$ 1 mm restricted the possibility to perform low temperature measurements in the FTIR spectrometer. In order to extend the IR data to lower frequencies it is required to perform these measurement using a IR microscope cryostat.

3 Fullerene-based compounds

In this chapter, the pressure-dependent investigations on the fullerene-based materials, pure C_{70}*,* $C_{60}\cdot C_8H_8$ *and* $C_{70}\cdot C_8H_8$ *are presented. The basic properties of fullerenes which are important for understanding the results of this project are explained in the first section, and the infrared spectroscopic investigations are presented in the subsequent sections.*

3.1 Introduction to fullerenes

The name "fullerene" was given by Kroto and Smalley to the family of carbon-based molecules observed in their work, due to their resemblance to the geodesic domes designed and built by R. Buckminster Fuller. The name "buckminster fullerene" or simply "buckyball" was given specifically to the C_{60} molecule, whose structure is shown in Figure 3.1. C_{60} is the most abundant form of fullerene although stable forms of other higher-order fullerenes have also been synthesized.

3.1.1 Properties of C_{60}

The C_{60}, the most symmetric fullerene molecule (see Figure 3.1), has all equivalent carbon sites. Each carbon atom is trigonally bonded to three other carbon atoms

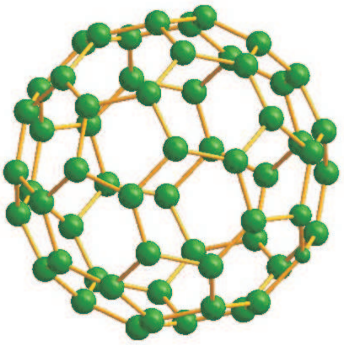

C_{60}

Figure 3.1: *Structure of* C_{60} *molecule. The* C_{60} *molecule belongs to the icosahedral point group* (I_h).

Figure 3.2: *Crystal structure of solid C_{60}. The solid C_{60} has the fcc structure at room temperature.*

in sp^2 configuration. The diameter of the C_{60} molecule including the size of the π-electron cloud associated with the carbon atoms on the shell, is 10.34 Å [41]. In the solid state, the fullerene molecules form cubic crystals commonly referred as fullerites, wherein the molecules are held together due to van der Waals force of attraction. The crystal structure of the solid C_{60} is shown in Figure 3.2. At ambient conditions, the C_{60} fullerite exists in the face-centered-cubic (fcc) lattice.

Vibrational and electronic properties

The C_{60} molecule belongs to the icosahedral point group (I_h). The vibrational modes corresponding to this structural symmetry may be calculated and are [42]: $2A_{1g}$ + $3T_{1g}$ + $4T_{2g}$ + $6G_{1g}$ + $8H_{1g}$ + $1A_{1u}$ + $4T_{1u}$ + $5T_{2u}$ + $6G_{1u}$ + $7H_{1u}$. Among these vibrations, the $4T_{1u}$ vibrational modes are infrared active, and lie at frequencies 527 cm^{-1}, 576 cm^{-1}, 1183 cm^{-1}, and 1429 cm^{-1} [43–46]. Since the C_{60} fullerite is a van der Waals crystal, the intermolecular vibrations have very low energies compared to the intramolecular vibrations. The intermolecular and librational vibrations in these molecular solids typically have energies below 270 cm^{-1} [41].

In order to understand the electronic structure of the higher-order fullerenes and fullerene derivatives, it is worth discussing the properties of the most extensively investigated C_{60} first. The electronic and optical properties of C_{60} are mainly dominated by the contributions from the π orbitals which lie closer to the Fermi level than the σ orbitals. The electronic structure of C_{60} in its both molecular state and solid state are shown in Figure 3.3. The optically-allowed transitions according to the symmetry of the molecule are indicated in Figure 3.3(a). In the solid state, the intermolecular interactions do not affect the molecular wave functions significantly since the van der Waals forces are relatively weak but the molecules rather interact through an electric dipole-dipole interaction. However, these next-neighbor interactions broaden

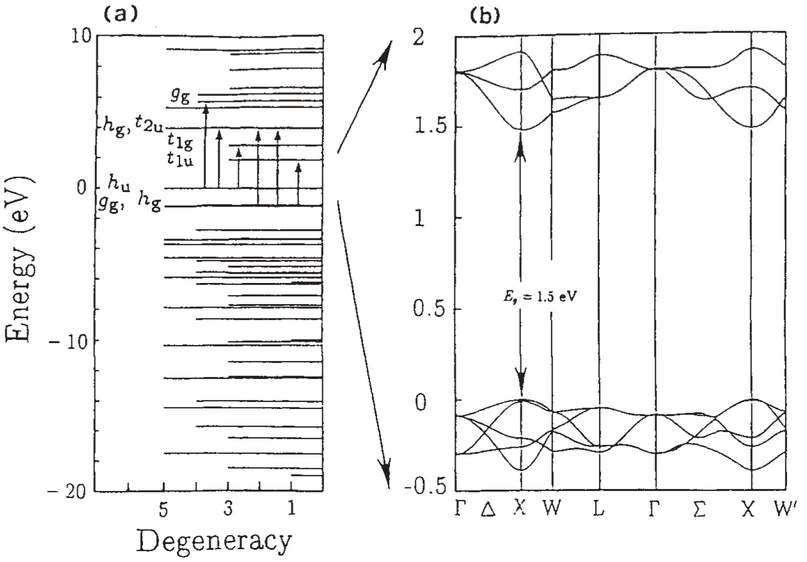

Figure 3.3: *(a) Calculated electronic structure of the isolated C_{60} molecule and (b) the electronic structure of solid C_{60} in fcc phase. [41]*

the molecular orbitals into electronic energy bands (Figure 3.3(b)). The early bandstructure calculations using the local density approximation (LDA) showed that the solid C_{60} is a direct bandgap semiconductor with a gap energy of 1.5 eV [47]. However, the later calculations using GW quasiparticle approach find a bandgap of 2.15 eV [48]. It can be seen from the energy level diagram (Figure 3.3 (a)) that the transition across the highest occupied molecular orbital (HOMO) - lowest unoccupied molecular orbital (LUMO) gap is optically forbidden [47]. Therefore, it was suggested that the onset of the absorption edge in the optical properties of solid C_{60} is due to the weakly phonon-assisted Frenkel exciton while the allowed transitions lie at the higher energies than the excitonic transition [49–51]. This observation was further supported by means of the electron energy loss spectroscopy (EELS) in transmission, indicating a monopolar character of the spectral feature at around 1.8 eV. Such transition is then a singlet exciton in which an electron has been excited from the HOMO to LUMO levels of the same C_{60} molecule in the solid [52]. The spectral feature observed in EELS in reflection and optical absorption studies around 1.8 eV is instead the phonon-assisted triplet exciton.

Pressure-temperature phase diagram

Pristine C_{60} has a rich pressure-temperature (p-T) phase diagram which is shown in Figure 3.4. The orientational ordering transition in C_{60}, where the crystal structure

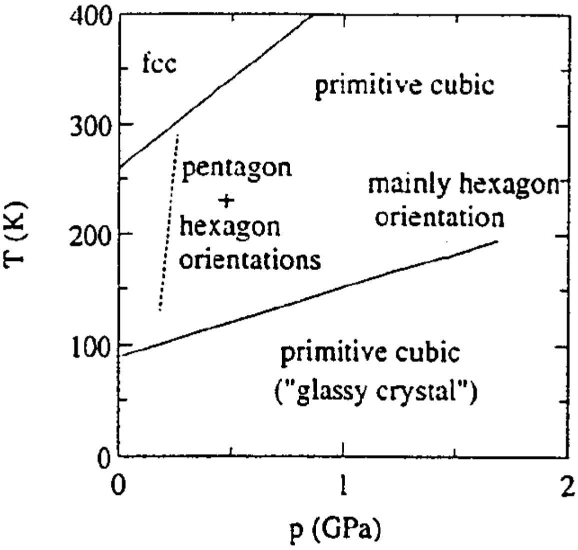

Figure 3.4: *Pressure-temperature phase diagram of the solid C_{60} [59].*

changes from fcc to simple cubic (sc), occurs at 0.2 GPa at room temperature [53,54]. Furthermore, a second anomaly was reported at around 2 GPa in several experimental studies [55–58]. However, the values of the critical pressure of this second transition obtained by different experiments are not consistent, and the origin of this transition is still unclear. Generally, an increase in pressure is expected to have the same effect on a material as a decrease in temperature. Therefore, based on a comparison with the phase transitions occurring in C_{60} with decreasing temperature - a transition to an orientationally ordered state at 260 K and a glass transition at 90 K - the two anomalies in C_{60} at 0.2 and 2 GPa were attributed to an fcc-to-sc and a glass transition, respectively [55,56].

The interpretation of the second phase transition (glass transition) is, however, questionable [60]. In the orientationally-ordered sc phase of C_{60}, found above 0.2 GPa at room temperature and below 260 K at ambient pressure, there are two possible orientations of the C_{60} molecules obtained by rotating them either by ≈38° or ≈98° around the [111] crystal axis. In the first case (38° rotation) the electron-rich double bonds on the C_{60} molecule face the electron-poor centers of the hexagons on its neighbors, and the corresponding orientation is therefore called H-orientation. In the second case (98° rotation), called P-orientation, the electron-rich double bonds on the C_{60} molecule face the electron-poor centers of the pentagons on its neighbors. It was concluded from calculations of the intermolecular energy that C_{60} molecules in the ordered sc phase contain a large number of well-oriented microdomains of both P- and H-orientations [61]. On increasing pressure, an almost completely H-oriented structure is expected above a critical pressure at around 1.2 GPa at room temperature [60,62]. The existence of preferable H-orientation of C_{60} molecules at high pressures was supported by experi-

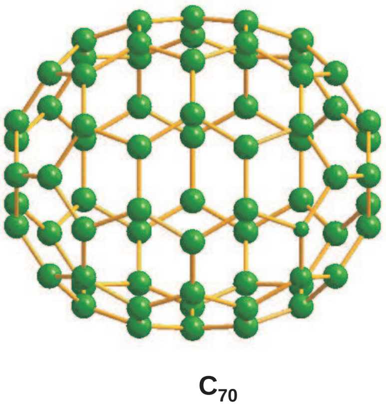

Figure 3.5: *Structure of C_{70} molecule. The C_{70} molecule belongs to the icosahedral point group (D_{5h}).*

mental data on compression properties, thermal conductivity, and Raman scattering studies [63–65]. Also, the high-pressure neutron scattering studies showed that the data at 1.6 GPa at room temperature were in much better agreement with a predominantly H-oriented state, since the H-oriented phase has a slightly smaller molecular volume and therefore is energetically preferable at high pressures [66]. In addition, an estimation from the linear extrapolation of low-pressure glass transition line in the experimentally-obtained p-T phase diagram, yields a glass transition pressure of 3.4 GPa at 293 K [60]. Accordingly, the glass transition is expected at higher pressure. It was therefore suggested that the anomalies at around 2 GPa are more likely related to a change in the orientational ordering of the fullerene molecules, namely from P- to H-orientation [60].

3.2 Pure C_{70}

3.2.1 Basic Properties of C_{70}

C_{70} has a slightly elongated "rugby ball" shape (shown in Figure 3.5) with molecular symmetry D_{5h}. As implied by its low symmetry, the molecule consists of five inequivalent atomic sites, eight different bond lengths and twelve different bond angles. The shape can be visualized by adding a belt of five hexagons around the equatorial plane of the C_{60} molecule which is normal to one of the five-fold axis and rotating the two hemispheres of C_{60} such that they fit to the belt of hexagons. These fullerenes also form van der Waals molecular crystals in the solid state. Unlike C_{60}, the crystal structure of solid C_{70} at ambient conditions, may be either fcc or rhombohedral (rh) structure. The C_{70} crystals are known to contain several structural phases due to stacking faults in the crystal. This commonly leads to the presence of minority amount of hexagonal-close packing (hcp) phase in the crystals. This structural disorder was attributed to nearest neighbor interactions which are not strong enough to provide a well-defined stacking sequence [60], therefore the crystal structure is highly dependent on the crystal growth temperatures [67].

Vibrational and electronic properties

Similar to C_{60}, the vibrational modes observed in the infrared and Raman spectra are the intramolecular vibrations. D_{5h} symmetry of the C_{70} molecule has the vibrational modes $10A_2'' + 21E_1' + 12A_1' + 22E_2' + 19E_2'' + 9A_2' + 9A_1'' + 20E_2''$, where only the E_1' and the A_2'' modes are infrared-active [68]. Several Raman and infrared measurements on C_{70} have been performed identifying most of the fundamental vibrational modes. The calculated and experimentally observed fundamental infrared modes are tabulated in Table 3.1, together with their symmetry assignments.

Fullerene C_{70} is a closed shell system with a HOMO-LUMO gap of about 1.76 eV [72]. Similar to C_{60}, the optical absorption edge of C_{70} and other higher fullerenes is shown to be an excitonic absorption [41].

Pressure-temperature phase diagram

In spite of enormous experimental efforts, the properties of C_{70} are not yet well understood due to the existence of metastable phases and the high dependence of the physical properties on the sample quality [60]. On cooling from high temperatures, the C_{70} undergoes orientational ordering transitions similar to C_{60}. However, the molecular rotation is much more complicated in C_{70}. At high temperatures, the fullerenes are rotating freely. At about 350 K, the rotation about the short molecular axis of the C_{70} molecule is stopped and the molecules are allowed to rotate only along its long axis (C_5) [73, 74]. Assuming as a starting structure the most stable fcc, a structural transition to rhombohedral (rh) phase is achieved during the orientational ordering. The uniaxial rotation of the fullerene about its long axis persists up to 280 K. Below 280 K, the motion of C_{70} molecules is completely stopped and the structure changes from rh to monoclinic (mc).

Several experimental investigations under pressure have also been performed on this compound. A first-order transition where the fcc structure of solid C_{70} changes to rh below 0.9 GPa at room temperature, was reported by Kawamura *et al.* [85–87]. The rh-distortion was found to increase with increasing pressure. A saturation of the rh-angle around 1 GPa was observed in these XRD measurements and attributed to the transformation to a mc phase [86]. Christides *et al.* suggested that the onset of the fcc-rh transition occurs around 0.35 GPa, with fcc phase coexisting up to 1 GPa at room

Table 3.1: *Infrared-active vibrational modes of C_{70} are listed together with their assignments and the experimental values at ambient conditions [45, 69–71].*

Mode	ν (cm^{-1})	$\nu_{observed}$ (cm^{-1})	assignment
F1	318	-	A_2''
F2	326	-	E_1'
F3	359	-	E_1'
F4	416	-	E_1'
F5	459	458	A_2''
F6	507	-	E_1'
F7	535	535	E_1'
F8	564	565	A_2''
F9	573	578	E_1'
F10	639	642	E_1'
F11	667	674	E_1'
F12	703	-	A_2''
F13	730	-	E_1'
F14	751	795	E_1'
F15	828	-	E_1'
F16	896	-	A_2''
F17	906	904	E_1'
F18	1086	1088	E_1'
F19	1144	1135	A_2''
F20	1178	1176	E_1'
F21	1207	1203	A_2''
F22	1256	1251	E_1'
F23	1291	1291	E_1'
F24	1319	1314	E_1'
F25	1321	1320	A_2''
F26	1416	1414	E_1'
F27	1432	1430	E_1'
F28	1463	1460	A_2''
F29	1491	1489	E_1'
F30	1567	1561	A_2''
F31	1569	1585	E_1'

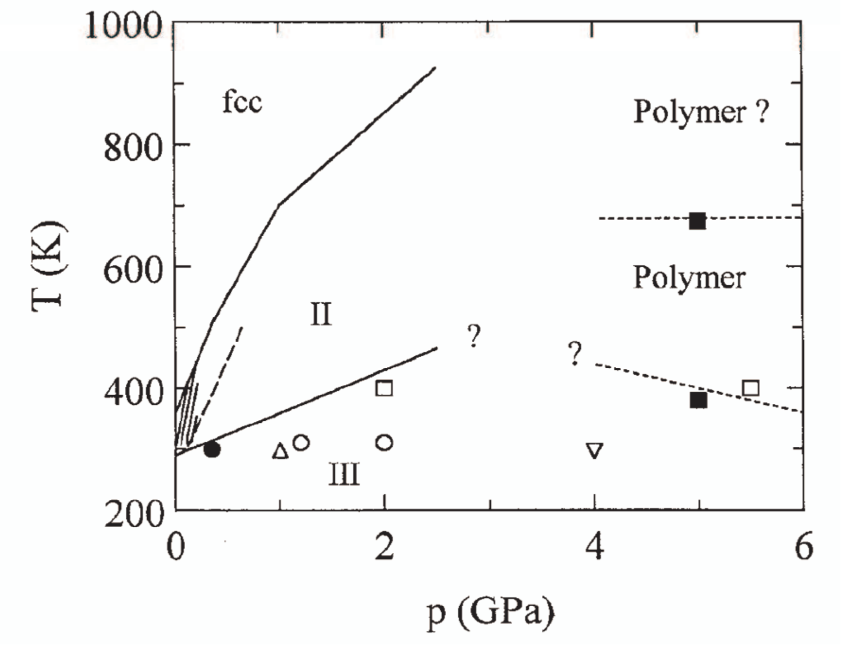

Figure 3.6: *Tentative pressure-temperature phase diagram of the solid* C_{70} *[60]. The estimation of the slope of full lines is presented in Ref. [60]. The broken line is the transition line given by Samara et al. [75, 76]. The shaded region corresponds to region of continuous orientational ordering with increasing pressure [77, 78]. Symbols denote positions of anomalies observed by Christides et al. [79] (solid circle), Huang et al. [58] (up triangle), Sood et al. [80] (open circle), Maksimov and co-workers [81, 82] (open square), Snoke et al. [83] (down triangle) and Iwasa et al. [84] (solid square).*

temperature, based on their energy dispersive X-ray diffraction studies [79]. Generally, compression of the lattice forces the C_{70} molecules to line up parallel, inducing and enhancing the orientational ordering of the molecules that leads to a rh symmetry of the lattice [60]. Furthermore thermal conductivity and compressibility studies on C_{70} found two anomalies at around 0.15 GPa and 0.7 GPa at 296 K [77, 78, 88]. These anomalies were attributed to a continuous change of the orientational ordering and eventual "freezing" of molecular rotations probably accompanied by a fcc-rh structural phase transition in analogy to the changes observed upon decreasing temperature.

Few Raman and infrared spectroscopic studies under pressure at room temperature were performed on C_{70}. However some of these investigations used mixtures of C_{60} and C_{70} which is undesirable as the presence of C_{60} influences the physical properties of C_{70} [89, 90]. The pressure-dependent Raman spectroscopic measurements on pure C_{70} found anomalies which were attributed to the orientational ordering transitions [80–82]. Sood *et al.,* found an anomaly at around 1 GPa in the pressure-dependence of the frequencies and linewidths of the Raman-active vibrational modes which was attributed to the fcc-rh orientational ordering transition [80]. Raman studies by Maksimov and coworkers exhibited two anomalies at around ≈ 2 GPa and ≈ 5.5 GPa, attributed to the features related to the orientational ordering of C_{70} molecules [81, 82].

The pressure-dependent infrared study on mixtures of C_{60} and C_{70} found splitting of a vibrational mode at 535 cm^{-1} [58]. On the other hand, infrared measurements on pure C_{70} found no discontinuous change in the pressure dependence of the vibrational modes [91]. Sundqvist *et al.,* proposed the p-T phase diagram of solid C_{70} based on these experimental investigations as shown in Figure 3.6. From the phase diagram it is obvious that pressure dependence of C_{70}, especially for pressures above $\approx$3 GPa, needs to be investigated further. The anomalies near 4-5 GPa in the phase diagram are connected with the polymerization observed in the spectroscopic studies by Iwasa *et al.,* [84].

The various pressure-dependent spectroscopic measurements exhibit discrepancies in the reported anomalies (see Figure 3.6). Therefore, there is still a need to clarify the discrepancies in the optical response of C_{70} under pressure and confirm the p-T phase diagram. Hence, the pressure-dependent infrared transmittance measurements on pure C_{70} for pressure up to 10 GPa were performed. A further aim is to search for additional anomalies at higher pressures ($p > 3$ GPa).

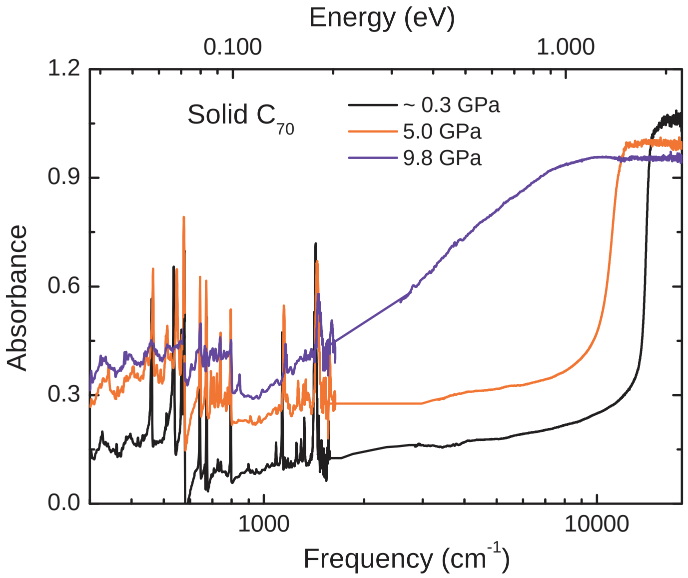

Figure 3.7: *Measured absorption spectra of C_{70} in the frequency range 300 cm^{-1} - 18000 cm^{-1} are shown for three pressures between 0-10 GPa.*

3.2.2 Pressure-dependent properties of C_{70}: An infrared spectroscopic study

The pressure-dependent transmittance measurements were performed on high-purity ($>$ 99%) C_{70} powder samples for pressures up to 10 GPa in the frequency range 300 cm^{-1} - 20000 cm^{-1}. The pressure transmitting medium used for these measurements is CsI. The studied C_{70} samples have an fcc phase at ambient conditions according to infrared studies showing phase transitions at 280 and 340 K [92] (the presence of admixture of another fullerene with C_{70} should lead to shift of lattice parameters and transition temperature [93, 94]).

The absorbance spectra of solid C_{70} over the whole measured frequency range are shown in Figure 3.7 for selected pressures between 0-10 GPa. The interference fringes in the spectra are due to multiple reflections of the incident radiation within the DAC. The low frequency part of the spectra is dominated by the vibrational modes of the fullerene molecules while the electronic absorption edge lies in the NIR-visible energy range.

Vibrational modes

The pressure-dependent absorbance spectra (shown with a vertical offset for clarity) of the vibrational modes of C_{70} are shown in Figure 3.8 for pressure up to 10 GPa. More than 20 infrared active modes are observed, among which some have very low intensity. In addition to the fundamental vibrations expected for the fullerene C_{70}, several weak bands are also observed in the infrared spectra.

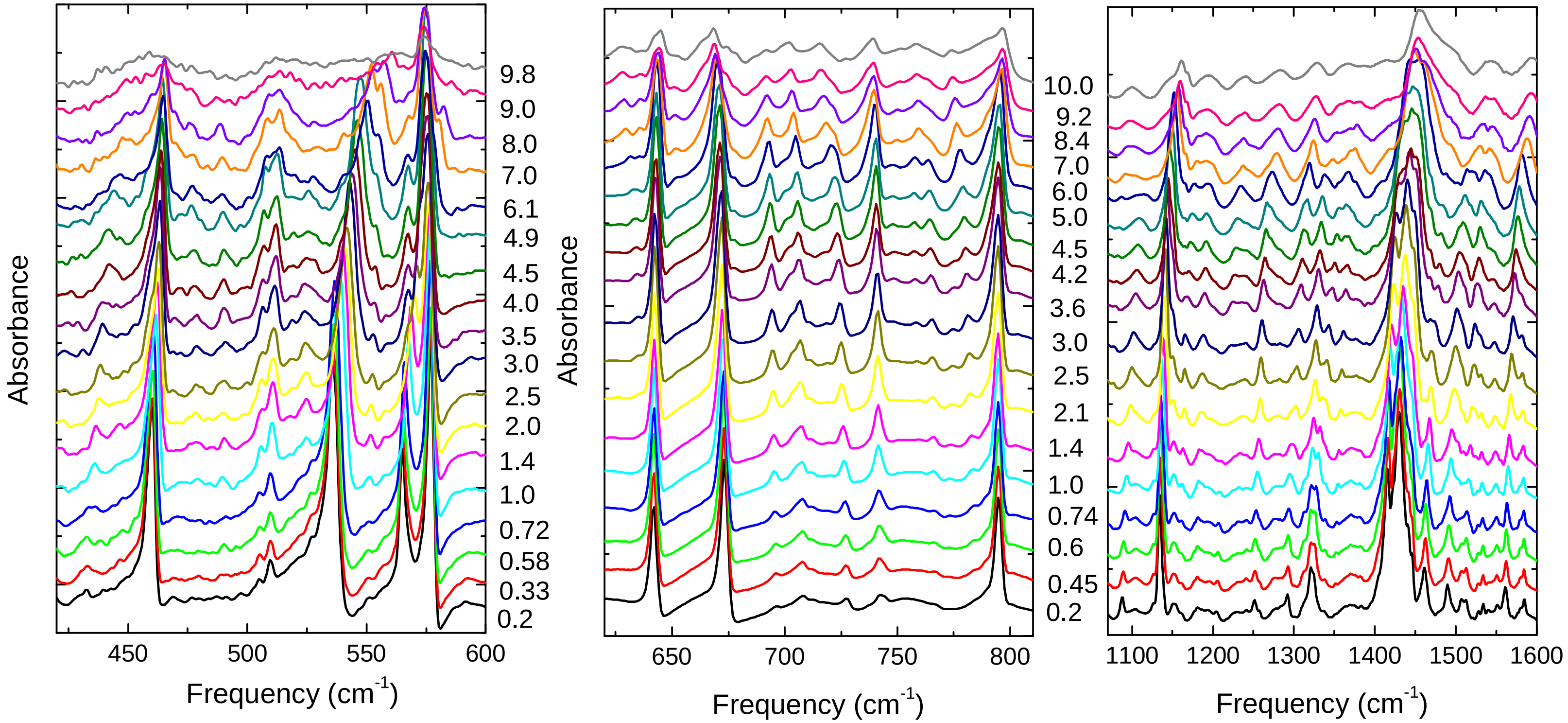

Figure 3.8: *Infrared absorbance spectra of* C_{70} *as a function of pressure for pressures between 0-10 GPa, presented with a vertical offset. The pressure in GPa corresponding to each spectrum is indicated next to it.*

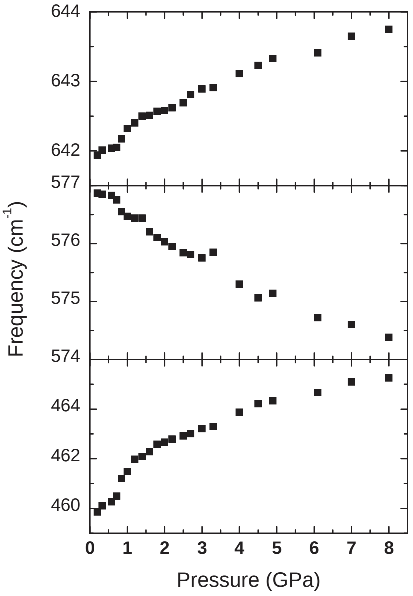

Figure 3.9: *Pressure-dependent frequencies of few vibrational modes of C_{70} for pressure up to 7 GPa.*

These weak bands were attributed to overtones and Raman or silent modes that are activated due to crystal field effects in the solid state and/or isotope effects [70, 95]. Such an activation of silent modes has been reported in C_{60} crystals [96, 97].

With increasing pressure, most of the vibrational modes of C_{70} shift to higher frequencies, except the modes at around 577 cm^{-1}, 673 cm^{-1}, 727 cm^{-1}, 742 cm^{-1} and 795 cm^{-1}. The redshift of the vibrational modes at 577 cm^{-1}, 673 cm^{-1} and 795 cm^{-1} with increasing pressure is in agreement with the earlier infrared studies under pressure [58, 91]. Although the intensity of some vibrational modes is reduced drastically at higher pressures, most of the vibrational modes persist up to 10 GPa.

The detailed quantitative information on the pressure dependence of the vibrational modes of C_{70} can be extracted by fitting the vibrational modes with Lorentzians. Such a fit allows an accurate determination of the characteristic energy of the vibrational modes. The extracted frequencies of some vibrational modes as a function of pressure up to 7 GPa are shown in Figure 3.9. The frequency of the vibrational modes exhibits a nearly linear pressure dependence with changes occurring at pressures below 4 GPa. Therefore, it is more appropriate to look at the pressure dependence of all vibrational modes at low pressures.

The extracted frequencies of the vibrational modes are shown in Figure 3.10 as a function of pressure up to 4 GPa. Despite the aforementioned nearly-linear behavior of the vibrational modes with increasing pressure, a clear anomaly is found at about 0.8 GPa. The pressure coefficients ($d\nu/dp$) of the vibrational modes for pressures $p<0.8$ GPa and $p>0.8$ GPa are different and also vary for each vibrational mode. The pressure coefficients of some vibrational modes are listed for both pressure regimes in

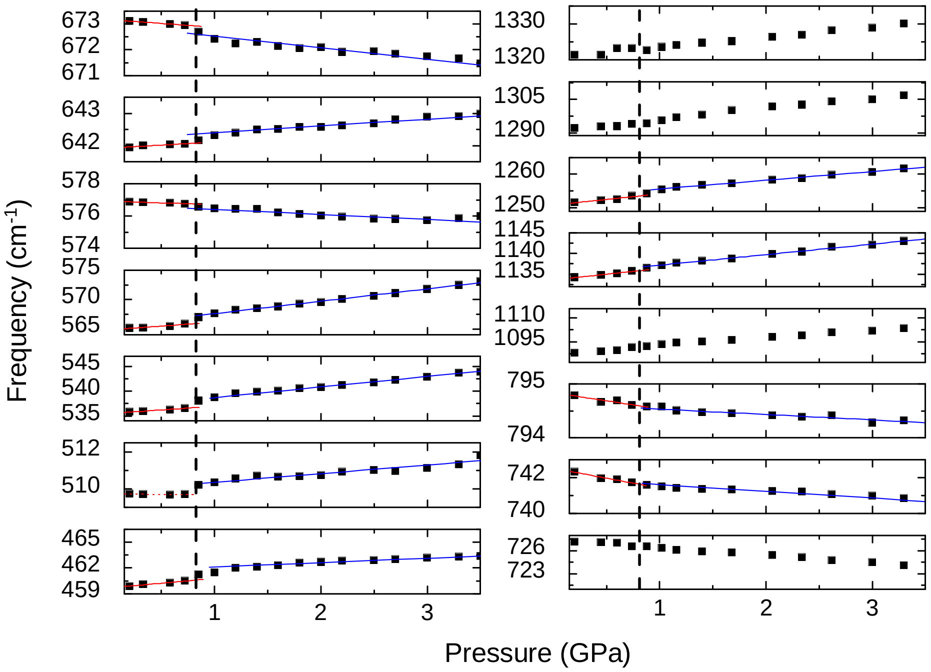

Figure 3.10: *Pressure-dependent frequencies of the vibrational modes of* C_{70} *in the pressure regime* $p < 4$ *GPa. The vertical dashed line indicates the pressure of the orientational ordering phase transition [98].*

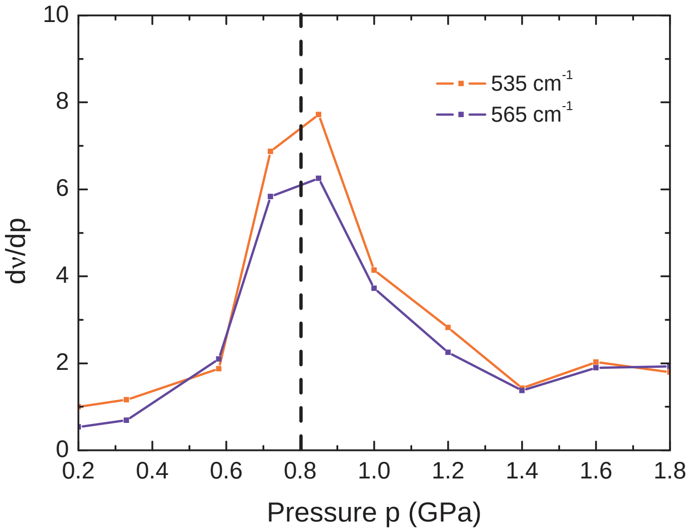

Figure 3.11: *Pressure derivative of the frequency of selected vibrational modes at 535* cm^{-1} *and 565* cm^{-1} *as a function of pressure. The broad anomaly around 0.8 GPa is clearly revealed by the maximum in the pressure derivative of the frequency of the vibrational modes [98].*

Table 3.2. These pressure coefficients though slightly different from previous works, lie in the same range [91].

Further confirmation of the anomaly can be obtained by checking for a maximum in the pressure derivative ($d\nu/dp$) of the frequency of the vibrational modes. Figure 3.11 shows the pressure derivative of the frequency of the vibrational modes at 535 cm^{-1} and 565 cm^{-1} as a function of pressure as an example. A broad maximum centered around 0.8 GPa is observed in the pressure derivative plot, clearly indicating the anomaly in the pressure dependence of the vibrational modes.

The change in the pressure coefficient of the vibrational modes at around 0.8 GPa is a clear sign for a phase transition. By means of energy-dispersive X-ray measurements, it was argued that the fcc to rh phase transition occurs around 0.9 GPa [79]. Therefore, the anomaly in the pressure dependence of the infrared-active vibrational modes of C_{70} can be attributed to the orientational ordering transition where the uniaxial motion of C_{70} molecules is completely restricted and the molecules are ordered. The transition is slow and appears to be sluggish. The reason for this sluggish transition could be a continuous change of the orientational order. An alternative explanation could be the presence of two similar phases of solid C_{70} at the transition pressure regime, causing a sluggish response to pressure or temperature. The slow change in the pressure dependence of the vibrational modes, is in fact similar to the pressure response observed in energy dispersive X-ray and thermal conductivity studies [78, 79]. The pressure of the ordering transition (0.8 GPa) is close to the value of 1 GPa reported in the Raman studies by Sood *et al.* [80].

At ambient pressures the uniaxial rotation of the C_{70} molecules averages out the distorting field of the neighboring molecules and the molecular symmetry remains in D_{5h} symmetry. After the phase transition the molecules stop, and the splitting of the vibrational lines due to the crystal-field distortion in the solid state is expected. In contrast, no splitting of the vibrational modes was observed up to 7 GPa.

In addition to the shift in the frequency of the vibrational modes, the intensity of the vibrational modes also exhibit changes with respect to the applied pressure. It can be seen from Figure 3.8 that the weak vibrational modes between 500-570 cm^{-1}, 680-795 cm^{-1} and 1200-1600 cm^{-1} gain intensity with increasing pressure up to 7 GPa. These vibrational modes which exhibit increasing strength with respect to pressure, include both weak fundamentals and crystal-field activated modes. Martin *et al.* also found an increase in intensity of some vibrational modes in the infrared transmission measurements on C_{60} single crystals after pressure treatment [46]. They argued that the vibrational lines that have a large increase in intensity at low temperature and/or high pressures are probably *ungerade* fundamentals [46]. Furthermore, it has

Table 3.2: The pressure coefficients $d\nu/dp$ of the vibrational modes, are tabulated for the pressure regimes below and above the critical pressure (p≈0.8 GPa) [98].

Mode frequency (cm^{-1})	$d\nu/dP$ for $p<0.8$ GPa (cm^{-1} GPa^{-1})	$d\nu/dP$ for $p>0.8$ GPa (cm^{-1} GPa^{-1})
460	1.12 ± 0.17	0.60 ± 0.04
510	-0.04 ± 0.03	0.47 ± 0.04
535	1.50 ± 0.18	1.95 ± 0.05
565	1.34 ± 0.37	2.11 ± 0.06
577	-0.20 ± 0.07	-0.30 ± 0.02
642	0.19 ± 0.06	0.21 ± 0.01
673	-0.29 ± 0.01	-0.45 ± 0.02
742	-1.11 ± 0.17	-0.38 ± 0.03
1134	2.77 ± 0.35	2.51 ± 0.07
1251	3.34 ± 0.75	2.30 ± 0.09

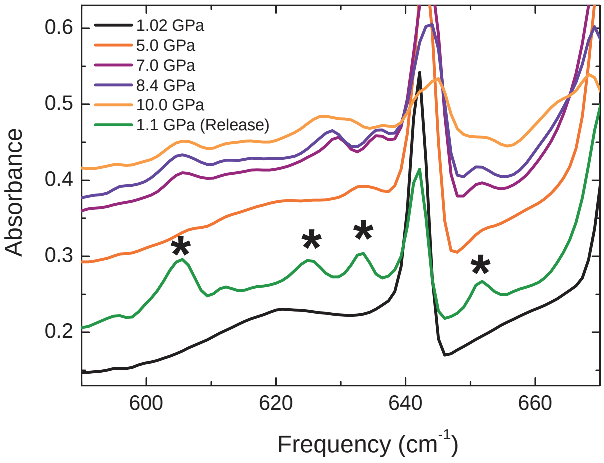

Figure 3.12: *Infrared absorbance spectra in the frequency range 570-670 cm^{-1} where the vibrational modes appear at pressure of about 7 GPa. These vibrational modes activated at high pressure remain (with even higher intensity) on releasing pressure.*

been suggested that the intermolecular interactions can activate silent modes in the infrared spectra of fullerenes [95]. Thus, the observation of increasing intensity of otherwise weakly-allowed modes with the application of pressure can be attributed to the symmetry breaking caused by the structural distortions and the increasing intermolecular interactions. It is worth noticing that the intensity increase sets in at about 1 GPa (most obvious in the weak modes in the ranges 500-570 cm^{-1} and 680-795 cm^{-1}; see Figure 3.8) around which the orientational ordering of the C_{70} molecules occurs. This implies that the symmetry change during the orientational ordering, activates the otherwise silent modes and the continuous increase of the intensity with further application of pressure is a signature of increasing intermolecular interactions.

At pressures above 7 GPa, almost all the vibrational modes begin to broaden and lose intensity drastically making their identification harder among the superimposed interference fringes. Furthermore weak modes appear at around 605 cm^{-1}, 625 cm^{-1}, 633 $cm^{-1}$and 652 cm^{-1} which persist even after pressure release (see Figure 3.12). However, the disappearance of existing modes was not observed. New modes at approximately same frequencies have been observed in earlier high-pressure-high-temperature polymerization studies [84, 99]. It is surprising that these modes have been observed by the earlier reports in the pressurized samples treated at temperatures as high as 300°C. Based on the X-ray and spectroscopic investigations, it was suggested that intermolecular bonds are formed in pressurized C_{70} and the appearance of new modes was attributed to the pressure-induced dimerization of C_{70} molecules [84,99]. The complete amorphization of C_{70} fullerene was reported only for pressures above 10 GPa which is the highest measured pressure in the high-pressure studies presented here [79, 100]. Thus, the observed changes at high pressures above 7 GPa up to 10 GPa can be attributed to the increasing structural distortions causing interlinking of fullerenes probably forming dimers, and the amorphization can be probably expected at pressures much higher than that reported here.

The p-T phase diagram might then be improved by incorporating the present results, as shown in Figure 3.13. The phase transition line (black dashed line) obtained by means of the X-ray diffraction from Kawamura *et al.* [85–87] has a steeper slope than the anomalies observed by several experimental investigations (see Section 3.2.1 and Figure 3.6 for more details on the earlier p-T phase diagram). The anomalies from the earlier experimental investigations together with that observed in this work, lie more or less in a line (represented by the pink dotted line) suggesting that the slope of the transition line obtained by Kawamura *et al.* is probably overestimated. This phase transition line drawn through the anomalies from various experiments gives rise to a broad phase transition regime at room temperature, which could also explain the

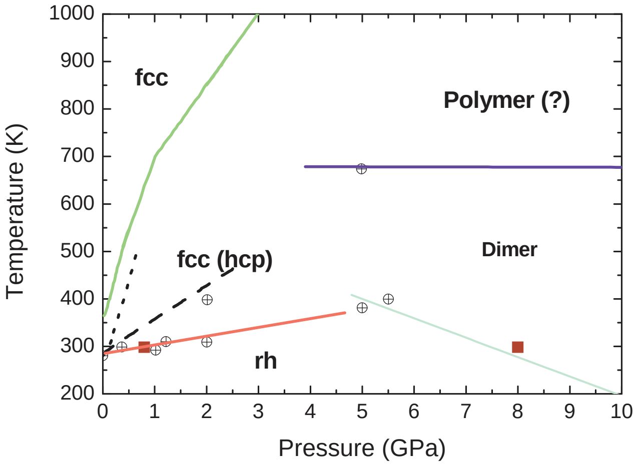

Figure 3.13: *The modified pressure-temperature phase diagram of the solid* C_{70} *(adopted from [60]). The open circle symbols with center cross represent the anomalies observed by various experimental investigations (see Figure 3.6 for details). The square solid symbols represent the pressures at which the anomaly (0.8 GPa) and major changes (8 GPa) occur in the infrared absorbance spectra.*

observed sluggish nature of the transition.

Also, the pressure of 8 GPa above which the vibrational modes lose intensity drastically was also considered as an anomaly. It can be seen that this pressure value agrees reasonably well with the monomer-polymer transition line proposed by Iwasa *et al.* [84]. Apparently, the transition line could rather be an onset of dimerization than the polymerization or amorphization.

Absorption edge

The absorption edge of C_{70} exhibits considerable changes with the application of pressure. The absorption spectra of the C_{70} in the NIR-visible frequency range in which the electronic absorption edge lies, is shown in Figure 3.14 for selected pressures between 0-10 GPa. The absorption edge energy decreases with increasing pressure up to 10 GPa.

The molecular orbital levels in van der Waals molecular crystals are broadened into bands due to intermolecular interactions at ambient conditions. The band broadening and hence the onset of the electronic absorption are very sensitive to changes in intermolecular interactions. Therefore, the energy of the onset of the electronic absorption can serve as a measure of the strength of intermolecular interactions.

Both external and chemical pressure will affect the intermolecular distances. Via both ways the importance of the intermolecular forces for the electronic properties can thus be clarified. In particular, the application of external pressure is a “clean” way to continuously tune the intermolecular distances, and the effect on the absorption edge can be studied.

For a quantitative analysis the absorption edge can be considered as the inflection

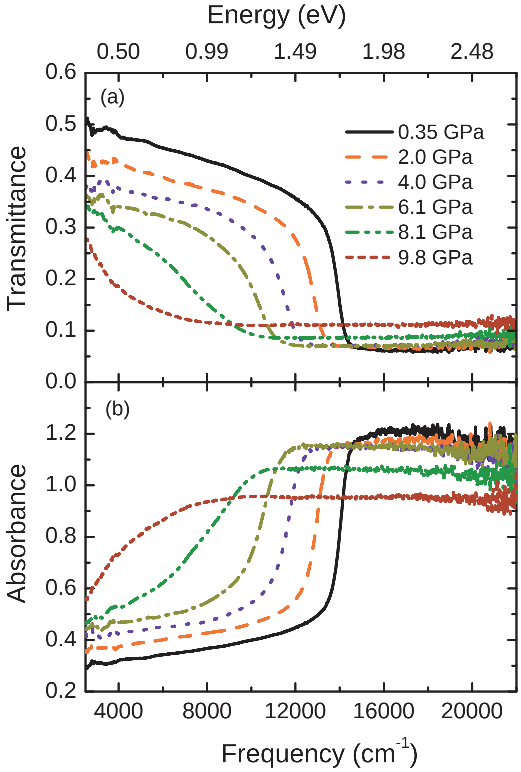

Figure 3.14: *(a) Transmittance and (b) absorbance spectra of* C_{70} *in the NIR-to-visible frequency range are shown for selected pressures between 0 and 10 GPa.*

Figure 3.15: *Absorption edge* E_a *of* C_{70} *as a function of pressure together with previous experimental results from Meletov et al. The inset shows, as an example, the derivative of the absorption spectrum at the lowest pressure with respect to frequency,* $dA/d\omega$*; the energy position of the maximum, as determined from a Gaussian fit (dashed line), served as an estimate for the size of* E_a*. The data point in green corresponds to* E_a *on releasing pressure.*

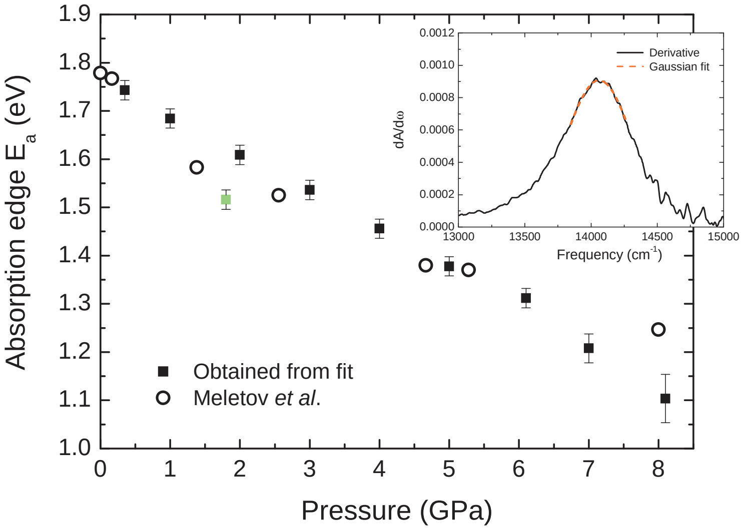

point of the absorption spectrum. Accordingly, the first derivative of the absorption spectrum shows a maximum (see inset of Fig. 3.15 for illustration) whose position serves as an estimate of E_a. The energy position was determined by a Gaussian fit. The resulting pressure dependence of E_a for C_{70} is shown in Fig. 3.15 in comparison with the results of Meletov *et al.* [101]. Although the bandgap decreases significantly, the complete closing of the gap is not observed in the measured frequency range. It can be seen from Figure 3.15 that these observations are consistent with the previous absorption studies on fullerite C_{70} by Meletov *et al.* The absorption edge at ambient pressure ($E_a(0)$) was found to be 1.77 eV. The pressure dependence of the bandgap is slightly nonlinear (nonlinearity factor of the order of 10^{-4}) with a pressure coefficient of about -0.077 eV/GPa. These values agree reasonably well with the previous high pressure studies [82, 101–103]. The pressure coefficient is also in agreement with the *ab-inito calculations* of the pressure derivative of the exciton energies in C_{60} [104]. The calculations were performed taking into account the changes in the transfer integrals due to the change in the separation between the adjacent molecules suggesting the importance of intermolecular interactions. In addition, because of the enormous strength of the intramolecular bonds [60], only minor contributions due to possible pressure-induced distortions of the fullerene “balls” are to be expected. Therefore, the observed pressure-induced redshift of the absorption edge in C_{70} is attributed to the increasing intermolecular interactions only [101, 105].

The pressure response of solid C_{70} may be compared with the one induced by chemical pressure as in the case of the new rotor-stator fullerene-cubane crystals. The rotor-stator compounds, $C_{60}{\cdot}C_8H_8$ and $C_{70}{\cdot}C_8H_8$, consist of fullerene and cubane molecules held by van der Waals forces. Before proceeding to the properties of the rotor-stator compounds, it is helpful to briefly review the properties of cubane.

3.3 Introduction to Cubane

Cubane, synthesized by Eaton and Cole in 1964, is an organic molecule with the chemical formula C_8H_8 [106]. The structure of cubane molecule is shown in Figure 3.16. Cubane is a unique molecule for its extraordinary C_8 cage. It has a very high symmetry, exceptional strain and unusual kinetic stability. Cubane is referred to as a hallmark in the world of impossible compounds, as the hybridization of the tetravalent carbon atoms is away from sp^3. The carbon-carbon bonds are *p*-rich, while the carbon orbital used for the C-H bond becomes *s*-rich. Due to their high heat of formation and reactivity, cubane and its functionalized derivatives find potential applications as high-energy fuels, explosives and propellants and intermediates in pharmaceutical

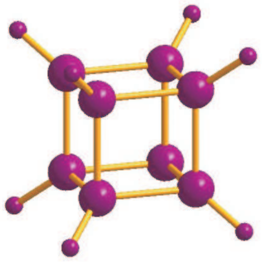

Figure 3.16: *The structure of cubane (C_8H_8) molecule.*

preparations [107].

The cubane molecules belong to the octahedral (O_h) point group, and the corresponding vibrations of cubane are $2A_{1g} + 2A_{2u} + 2E_g + 2E_u + 1T_{1g} + 4T_{2g} + 3T_{1u} + 2T_{2u}$. Among these vibrations only the $3T_{1u}$ vibrational modes of cubane are infrared-active [108]. The IR-active vibrational modes lie at energies 853 cm^{-1}, 1230 cm^{-1} and 2978 cm^{-1}. While the mode at 853 cm^{-1} corresponds to C-C stretch vibrations, the modes at 1230 cm^{-1} and 2978 cm^{-1} correspond to C-H wagging and stretching vibrations, respectively. The electronic absorption onset in cubane is at around 52000 cm^{-1} and other electronic transition lie at much higher energies [109], allowing the study of the electronic absorption edge of the fullerenes in these van der Waal crystals.

Very few studies have been performed so far to understand the temperature- and pressure-dependent properties of cubane. Raman spectroscopy, adiabatic and differential scanning calorimetry and NMR studies have demonstrated the presence of a first-order solid-solid phase transition in cubane at 394 K. Above this temperature the system enters an orientationally disordered phase that persists until the system melts at 405 K [110]. Recent theoretical calculation on the effect of pressure on cubane, predicts a complete pressure-induced orientational ordering in cubane at around 1.0 GPa, while its structure is expected to display only small changes with further increasing pressure up to 3 GPa [111]. Furthermore, from the first-principles investigations on the structural and electronic properties of cubane, it was suggested that cubane is twice softer than C_{60} according to the bulk modulus, but the pressure derivative of the bulk modulus was found to be the same as that for solid C_{60} [112]. An infrared absorption study on cubane (and 1,4-dinitrocubane) under pressure by Piermarini *et al.* [113] seems to be the only pressure-dependent experimental investigation on crystalline cubane. In this study, it was observed that cubane explodes spontaneously at room temperatures at pressures above 3 GPa [113].

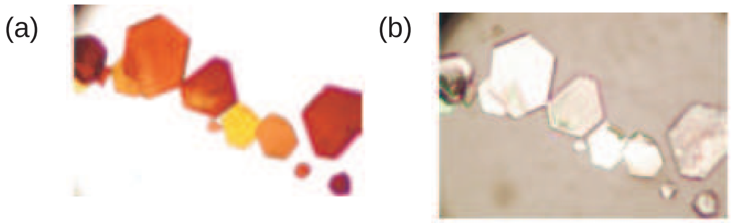

Figure 3.17: *(a) Optical transmission micrograph of $C_{60}{\cdot}C_8H_8$ crystal platelets; (b) Optical reflection micrograph of $C_{60}{\cdot}C_8H_8$ crystals [114].*

3.4 Novel rotor-stator compounds

The rotor-stator compounds $C_{60}{\cdot}C_8H_8$ and $C_{70}{\cdot}C_8H_8$ investigated within this work belong to the new family of heteromolecular crystals which consists of fullerene and cubane molecules [114]. The fullerenes with cubane form a high-symmetry molecular solid wherein the molecular species are held together due to molecular recognition between the convex surface of the fullerenes and the concave surface of the cubane. The heteromolecular crystals of fullerene and cubane occur in the rotor-stator phase only for fullerenes with ball diameters below 11.44 Å [114]. At higher ball diameters, the materials belong to the host-guest systems consisting of fcc framework of fullerenes with the octahedral voids occupied by orientationally disordered cubane molecules.

The stoichiometric samples of $C_{60}{\cdot}C_8H_8$ and $C_{70}{\cdot}C_8H_8$ were prepared by evaporating aromatic solutions of fullerene and cubane or by precipitating them with the addition of isopropyl alcohol [114]. The so-obtained crystals are platelet-shaped with typical sizes of 5-200 μm. The reflection and transmission micrographs of the pristine crystal platelets are as shown in Figure 3.17. A brief review of the physical properties of $C_{60}{\cdot}C_8H_8$ and $C_{70}{\cdot}C_8H_8$ and the pressure-dependent investigations within this project are presented in the forthcoming subsections.

3.4.1 $C_{60}{\cdot}C_8H_8$ and $C_{70}{\cdot}C_8H_8$

Crystal structure

At room temperature, the $C_{60}{\cdot}C_8H_8$ exists as a fcc crystal while $C_{70}{\cdot}C_8H_8$ occurs as body-centered tetragonal (bct) crystal. The crystal structure of both compounds at room temperature is shown in Figure 3.18. In these crystals, the fullerene molecules form an octahedral or trigonal prismatic configuration and the cubane molecules occupy the voids of the fullerene arrangement. The fullerene molecules rotate freely between the static cubane molecules forming a ball bearing arrangement. The C_{70} molecules in $C_{70}{\cdot}C_8H_8$ are in their first orientationally ordered state at room temperature where they rotate about the long axis (C_5) which in turn precesses about the

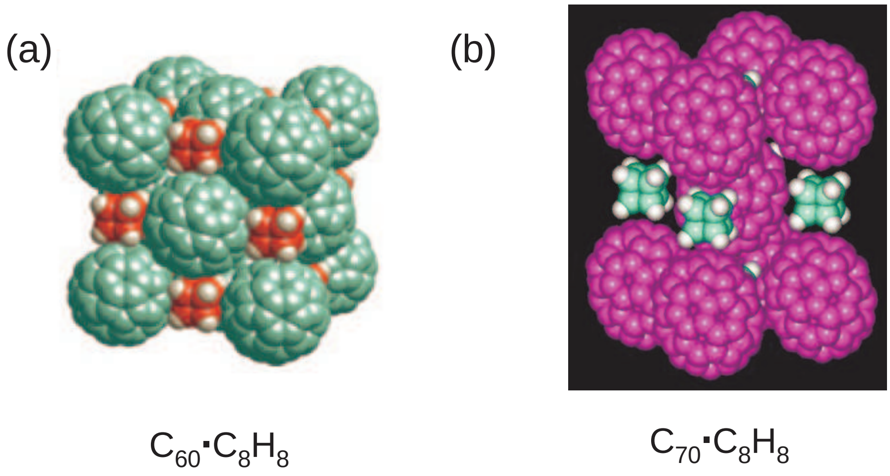

Figure 3.18: *Room temperature crystal structure of (a) $C_{60}{\cdot}C_8H_8$ and (b) $C_{70}{\cdot}C_8H_8$. The fullerenes form the cubic framework while cubane molecules occupy the octahedral voids between the fullerenes [92, 114].*

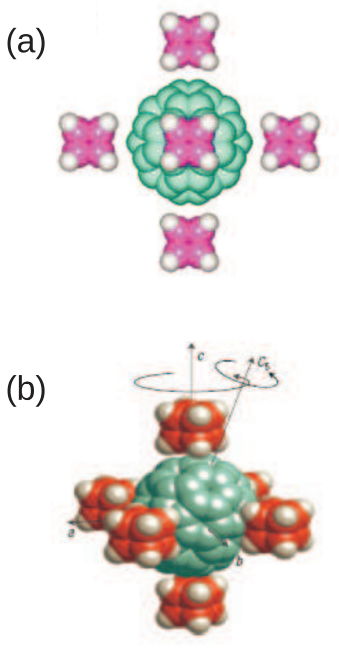

Figure 3.19: *(a) Octahedral coordination of C_{60} in $C_{60}{\cdot}C_8H_8$ [115]; (b) Coordination of C_{70} with respect to cubane in the elongated octahedron of $C_{70}{\cdot}C_8H_8$ [114]. The restricted motion of the C_{70} molecule in the rotor-stator phase in $C_{70}{\cdot}C_8H_8$ is also illustrated. The C_{70} in $C_{70}{\cdot}C_8H_8$ rotates about its long axis (C_5) which in turn precesses about the tetragonal c-axis.*

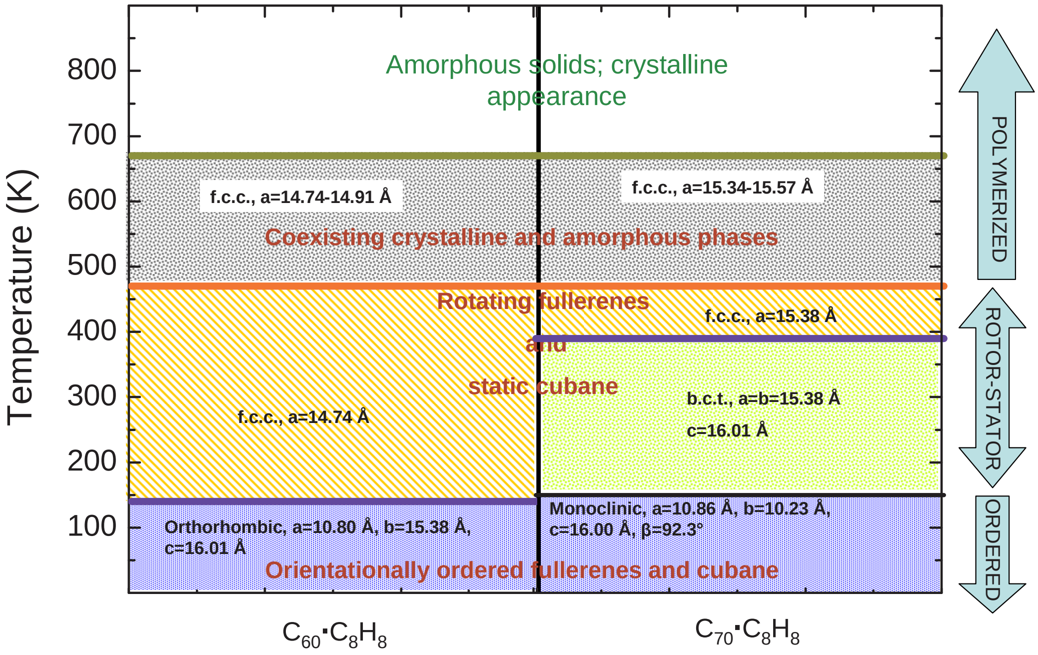

Figure 3.20: *Schematic phase diagram of* $C_{60}{\cdot}C_8H_8$ *and* $C_{70}{\cdot}C_8H_8$ *as a function of temperature (adopted from Ref. [114]).*

tetragonal c-axis. Figure 3.19 shows the coordination of the fullerene molecules in $C_{60}{\cdot}C_8H_8$ and $C_{70}{\cdot}C_8H_8$. The restricted motion of the C_{70} molecule is also illustrated here. The cubane molecules are aligned parallel with the faces of the unit cell with a higher symmetry environment than in their native crystals. The interfullerene distances in $C_{60}{\cdot}C_8H_8$ is enlarged in comparison with the solid C_{60}. On the other hand, the lattice expansion in $C_{70}{\cdot}C_8H_8$ is smaller than in $C_{60}{\cdot}C_8H_8$ due to more effective space filling facilitated by the prolate shape of C_{70}.

Temperature-dependent phase diagram

The crystal structures of both $C_{60}{\cdot}C_8H_8$ and $C_{70}{\cdot}C_8H_8$ were determined using powder and single-crystal X-ray diffraction [114, 116]. The temperature-dependent phase diagram of the rotor-stator compounds obtained from the X-ray diffraction measurements is shown in Figure 3.20. Similar to pure fullerenes, the rotational degrees of freedom of fullerenes in these high-symmetry crystals are restricted on lowering temperature leading to orientational ordering transitions. As can be seen from Figure 3.20, the orientational ordering in $C_{60}{\cdot}C_8H_8$ takes place at 140 K. This transition temperature is much lower than the transition temperature of 260 K in pure C_{60} due to the expanded lattice volume. During this phase transition, the symmetry of the crystal structure is

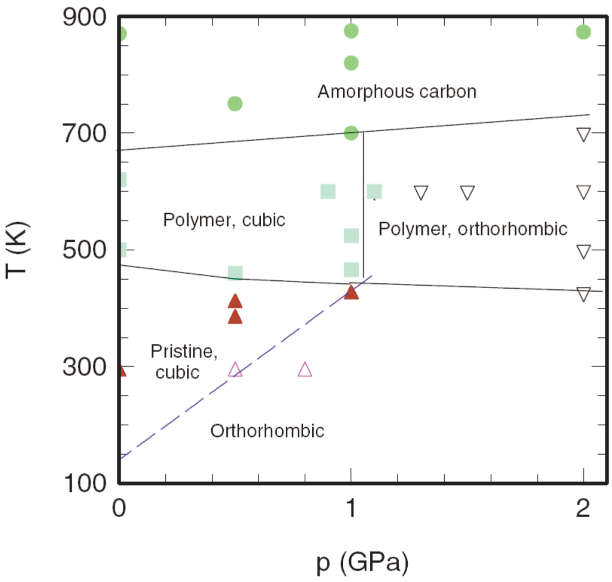

Figure 3.21: *Pressure-temperature phase diagram of $C_{60}\cdot C_8H_8$ obtained by means of X-ray diffraction and Raman spectroscopic studies by Sundqvist et al. [117].*

lowered by changing from fcc to orthorhombic. $C_{70}\cdot C_8H_8$ on the other hand undergoes two orientational ordering transitions. The first orientational ordering occurs above room temperature at 390 K accompanied by a structural phase transition from fcc to bct. At this transition, the free rotation of the C_{70} molecules is restricted to uniaxial motion about its C_5 axis which in turn precesses about the tetragonal c-axis (see Figure 3.19(b)). In pure fullerenes, the repulsive $\pi - \pi$ interactions give rise to orientational ordering transition. This interaction is much reduced in these rotor-stator compounds due to enlarged interfullerene distances. However, match of fullerene surface with the surface of cubane facilitates smooth rotation of fullerenes. This causes unusually low phase transition temperatures in these rotor-stator phases.

At high temperatures, both $C_{60}\cdot C_8H_8$ and $C_{70}\cdot C_8H_8$ remain in the rotor-stator phase up to 470 K. Above this temperature, the two molecular species in these heteromolecular crystals undergo solid-state reactions to form highly stable covalent derivatives due to polymerization. On further heating above 600 K, thermal decomposition of the compounds occurs causing mass loss.

In addition to the study of temperature-dependent properties, experimental investigations have been performed to understand the polymerization in $C_{60}\cdot C_8H_8$ under pressure and photo-irradiation [117–119]. The polymerization of $C_{60}\cdot C_8H_8$ at high temperature and pressure was investigated using Raman spectroscopy and X-ray diffraction at selected temperatures between 385-870 K and pressure up to 2 GPa [117, 118]. Polymerization was found to occur under pressure up to 2 GPa at temperatures above 400 K. Irradiation of green or blue light on $C_{60}\cdot C_8H_8$ was observed to induce photochemical reaction which leads to a product similar to that of the thermal polymerization [119]. The question whether polymerization can be achieved at pressures higher than 2 GPa at room temperature was yet to be answered.

High pressure technique is not only useful for polymerization studies but also to understand the complex interaction mechanism in these rotor-stator compounds. Pressure-dependent spectroscopic investigations enable us to study the effect of intermolecular interaction and structural changes on the properties of these materials. As the orientational ordering transitions occur at lower temperatures in comparison to pure fullerenes due to increased free volume in the lattice, the pressure-induced orientational ordering is expected to occur at higher pressures than that of the pure fullerenes. Recently, the pressure-induced phenomena in $C_{60}{\cdot}C_8H_8$ were investigated by pressure-dependent transmission measurements in the infrared frequency range [120]. It was found that the orientational ordering in $C_{60}{\cdot}C_8H_8$ indeed occurs at a pressure of about 0.8 GPa, which is significantly higher than for pristine C_{60}. Raman and X-ray diffraction investigations on $C_{60}{\cdot}C_8H_8$ also found that the pressure-induced phase transition from fcc to orthorhombic occurs around 0.5 GPa [117]. Based on the outcome of the pressure and temperature-dependent studies on $C_{60}{\cdot}C_8H_8$ the p-T phase diagram of $C_{60}{\cdot}C_8H_8$ (shown in Figure 3.21) was proposed by Sundqvist *et al.* [117]. As a part of the extended investigations of these new class of rotor-stator compounds, a detailed investigation of the optical properties of $C_{60}{\cdot}C_8H_8$ and $C_{70}{\cdot}C_8H_8$ under pressure by transmission measurements in the MIR up to the visible frequency range, was carried out in this project.

3.4.2 Pressure-dependent infrared studies on $C_{60}{\cdot}C_8H_8$ and $C_{70}{\cdot}C_8H_8$

The transmission measurements of a mixture of powder sample and the pressure transmitting medium were carried out for pressure up to 10 GPa over the frequency range 300 - 20000 cm^{-1}. The measurement resolution is 2 cm^{-1} in the MIR and 8 cm^{-1} in the NIR and visible frequency ranges. The quasi-hydrostatic pressure transmitting media used in the MIR was KCl. Transmission measurements in the NIR and visible frequency range were performed using KCl and argon as pressure transmitting medium, in order to check the possible effect of nonhydrostaticity on the pressure dependence of the absorption edge of $C_{60}{\cdot}C_8H_8$ and $C_{70}{\cdot}C_8H_8$.

The absorbance spectra of $C_{60}{\cdot}C_8H_8$ and $C_{70}{\cdot}C_8H_8$ over the whole measured frequency range are shown in Figure 3.22 for three pressures between 0-10 GPa. The interference fringes in the spectra are due to multiple reflections of the incident radiation within the DAC. The low frequency spectra consist of vibrational modes of

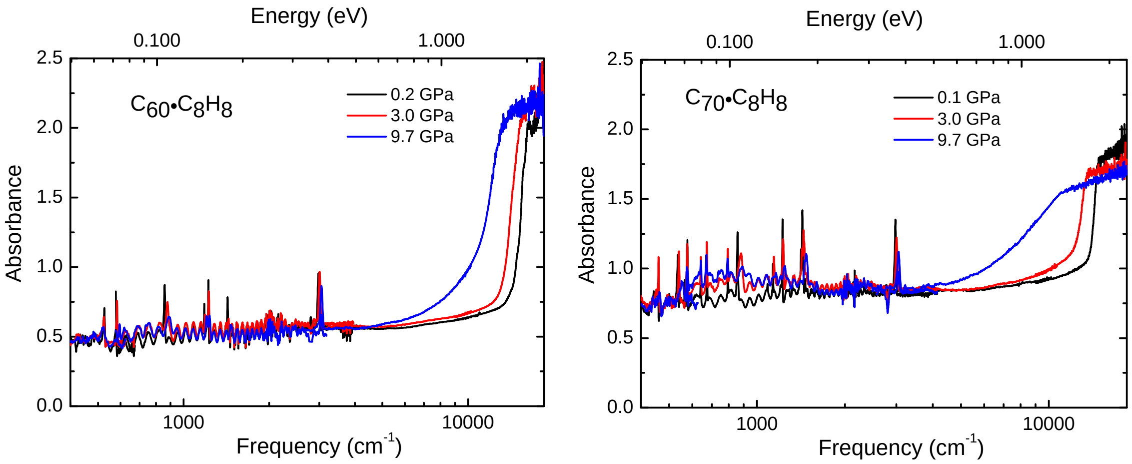

Figure 3.22: *Absorption spectra of $C_{60}\cdot C_8H_8$ and $C_{70}\cdot C_8H_8$ in the MIR-visible frequency range are shown for three pressures between 0-10 GPa.*

the fullerene and cubane molecules while the NIR-visible energy range consists of the electronic absorption edge of the rotor-stator compounds. The vibrational modes and the absorption edge show considerable changes with application of pressure. The following description of the properties of rotor-stator compounds under pressure, the pressure-induced changes in the vibrational modes and the absorption edge are discussed separately.

Vibrational modes

The fullerene and cubane molecules in the rotor-stator crystals $C_{60}\cdot C_8H_8$ and $C_{70}\cdot C_8H_8$ are held together by weak van der Waals interaction between the molecules and therefore the characteristic vibrational modes of both fullerene and cubane molecules can be observed in the infrared spectra of $C_{60}\cdot C_8H_8$ and $C_{70}\cdot C_8H_8$ with no shift of the fullerene modes and a slight red shift of the cubane modes, caused by the high polarizability of the fullerene environment [119]. It can be recalled that the infrared-active vibrational modes of C_{60}, C_{70} and C_8H_8 are $4T_{1u}$, $21E_1'$ and the A_2'', and $3T_{1u}$ respectively (see Sections 3.1.1, 3.2.1 and 3.3 for more details).

Figure 3.23 and Figure 3.24 show the absorption spectra of $C_{60}\cdot C_8H_8$ and $C_{70}\cdot C_8H_8$ as a function of pressure. Most of the modes exhibit a pronounced frequency shift and broadening under pressure. However, they could be observed up to the highest applied pressure of about 10 GPa. Furthermore, all the observed pressure-induced changes in the vibrational modes are reversible upon pressure release.

The behavior of the fullerene modes in both $C_{60}\cdot C_8H_8$ and $C_{70}\cdot C_8H_8$ under pressure is very similar to that observed in the pristine fullerenes [60]: In $C_{60}\cdot C_8H_8$ the

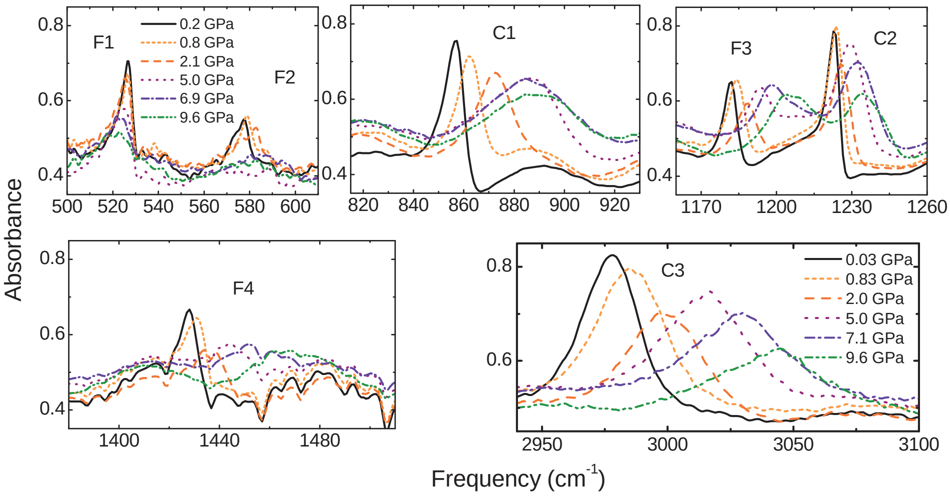

Figure 3.23: *Absorption spectra of $C_{60}{\cdot}C_8H_8$ in the mid-infrared frequency range for pressure up to 10 GPa [121]. The vibrational modes of the fullerene (cubane) molecules are denoted by F (C).*

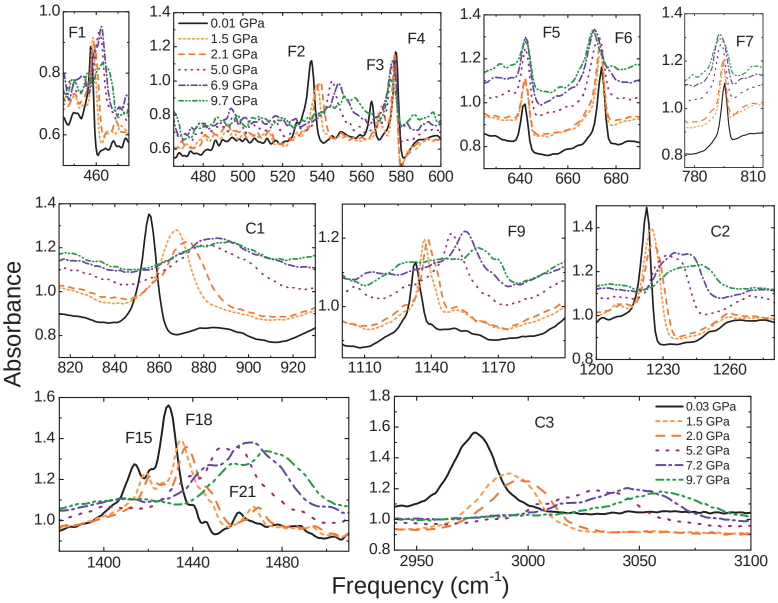

Figure 3.24: *Absorption spectra of $C_{70}{\cdot}C_8H_8$ in the mid-infrared frequency range for pressure up to 10 GPa [121]. The vibrational modes of the fullerene (cubane) molecules are denoted by F (C).*

Table 3.3: *Frequencies of the vibrational modes of $C_{60}{\cdot}C_8H_8$ at pressures ~ 0.5 GPa and 4 GPa [121]. The vibrational modes of the fullerene (cubane) molecules are denoted by F (C).*

Label	ν (cm^{-1}) at ~ 0.5 GPa	ν (cm^{-1}) at 4 GPa
F1	526	525
F2	577	584
C1	859	882
F3	1182	1191
C2	1223	1228
F4	1429	-
C3	2980	3008

fullerene modes harden with increasing pressure, except for the radial distortion mode at 527 cm^{-1}. In $C_{70}{\cdot}C_8H_8$ most of the fullerene modes shift to higher energies with increasing pressure, like in pristine C_{70}. Only the modes located at 577 cm^{-1}, 674 cm^{-1}, 795 cm^{-1}, and 1586 cm^{-1} shift to lower energies and exhibit a weak pressure dependence just like pristine C_{70} (see Section 3.2.2).

For both compounds the vibrational modes of the cubane molecules harden with increasing pressure. Interestingly, the pressure-induced changes for these modes are more pronounced than for the fullerene modes. In particular, in $C_{70}{\cdot}C_8H_8$ the cubane modes exhibit the signs of splitting together with broadening of the modes. Due to increasing width of the vibrational modes, the split modes are not well resolved and appear as shoulders in the broad absorption lines. Copolymerization is found to be induced by temperature, light [119] or high temperature and pressure [118]. Since the cubane lines are clearly visible up to 10 GPa, the occurrence of polymerization under high pressure at room temperature can be ruled out.

For a quantitative analysis of the pressure-induced changes in the absorption the frequencies of the vibrational modes of $C_{60}{\cdot}C_8H_8$ and $C_{70}{\cdot}C_8H_8$ were extracted by fitting with Lorentzian functions. The results are shown in Tables 3.3 and 3.4 for pressures 0.4 GPa and 4 GPa. The pressure dependence of two selected modes in both compounds are shown up to 10 GPa in Figure 3.25. The vibrational modes exhibit linear frequency shifts with changes in the slope at certain pressures in the low pressure regime, and the cubane modes in $C_{70}{\cdot}C_8H_8$ show a threefold splitting. For the discussion of the present results it is sufficient to focus on the pressure range up to 4 GPa, since the major changes occur here (as obvious from Figure 3.25). The pressure-induced frequency shifts of the vibrational modes of C_{60} and cubane in $C_{60}{\cdot}C_8H_8$ are

Table 3.4: *Frequencies of the vibrational modes of* $C_{70}{\cdot}C_8H_8$ *at pressures 0.4 GPa and 4 GPa [121]. The vibrational modes of fullerene (cubane) are denoted by F (C).*

Label	ν (cm^{-1}) at 0.4 GPa	ν (cm^{-1}) at 4 GPa
F1	458	460.6
F2	535.4	542.6
F3	565.8	575.2
F4	577.1	576.6
F5	641.8	642.2
F6	673.8	672.7
F7	795	793.7
C1	857.7	867.2
C	-	873.8
C	-	890.1
F8	1087.5	1101.0
F9	1134.4	1145.6
F10	1205.5	1220.2
C2	1223.5	1225.2
C	-	1229.5
C	-	1234.3
F11	1259	-
F12	1293	-
F13	1321.7	-
F14	1326.4	-
F15	1416.2	1425.2
F16	1422.8	1428.5
F17	1428.1	1434.6
F18	1432.4	1437.3
F19	1441.8	1445.2
F20	1446.9	1453.4
F21	1463	1470.5
F	-	1480.3
F22	1490	1502.9
F23	1533	-
F24	1562.9	1575.2
F25	1585.5	1583.7
C3	2979.3	2998.6
C	-	3017.2
C	-	3030.5

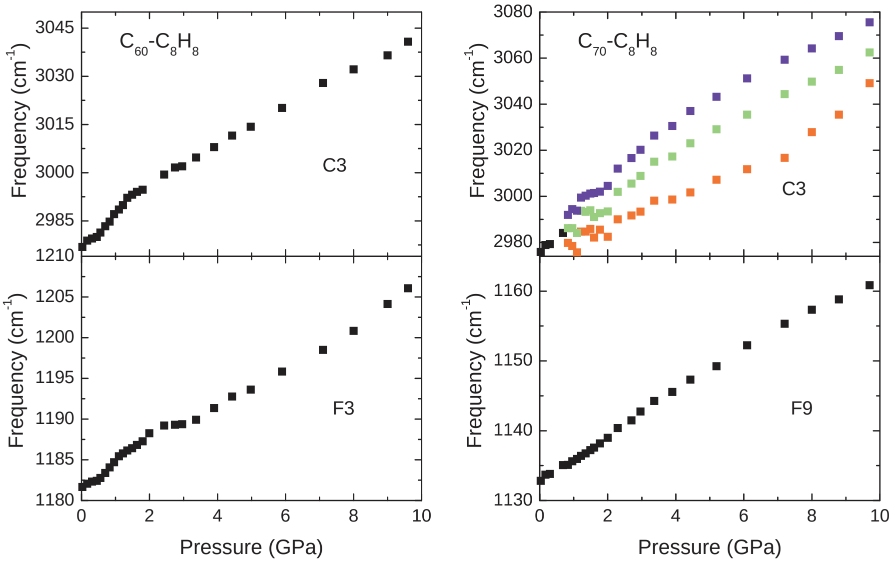

Figure 3.25: *Pressure dependence of two selected vibrational modes of* $C_{60}\cdot C_8H_8$ *and* $C_{70}\cdot C_8H_8$ *plotted as a function of pressure up to 10 GPa [121]. The vibrational modes of the fullerene (cubane) molecules are denoted by F (C); the labels are chosen in the order of increasing frequency.*

plotted in Figure 3.26. For C_{60}·C_8H_8 the anomalies occur at around 0.5 and 1.3 GPa.

The corresponding results of the vibrational modes of C_{70} and cubane in C_{70}·C_8H_8 are plotted in Figure 3.27. Since C_{70} has many infrared-active modes (see Table 3.4), only those with the strongest pressure dependence are shown in Figure 3.27. For C_{70}·C_8H_8 the observed anomalies in the pressure dependence of these modes are observed at around 0.8 and 1.75 GPa. The anomalies are pronounced for the cubane modes, while they are less obvious for the C_{70} modes. The overall pressure dependence of the fullerene in C_{70}·C_8H_8 can be compared to the pressure dependence in pristine C_{70} presented in Section 3.2.2. The pressure dependence of selected (low-frequency) vibrational modes of C_{70}·C_8H_8 shown along with the corresponding modes in pure C_{70} in Figure 3.28, confirms the consistent pressure dependence of the vibrational modes of fullerene C_{70}.

It is interesting to compare the results of C_{60}·C_8H_8 with the p-T phase diagram of pristine C_{60} (see Section 3.1.1 for detailed description) to get insight into the possible nature of the observed anomalies in C_{60}·C_8H_8. As previously discussed (see Section 3.4.1), an orientational ordering transition was found in C_{60}·C_8H_8 at 140 K at ambient pressure. At this transition, the rotational degrees of freedom of the fullerene molecules become restricted and the crystal structure changes from fcc to orthorhombic [60, 114, 116]. In analogy to the p-T phase diagram of C_{60} (see Figure 3.4), the

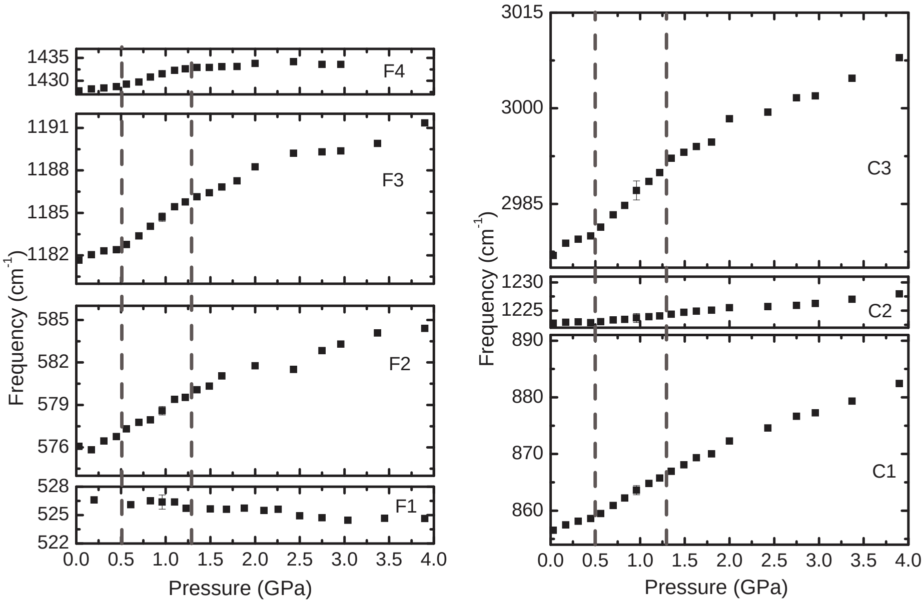

Figure 3.26: *Frequencies of the vibrational modes of $C_{60}{\cdot}C_8H_8$ plotted as function of pressure up to 4 GPa [121]. The vibrational modes of the fullerene (cubane) molecules are denoted by F (C); the labels are chosen in the order of increasing frequency.*

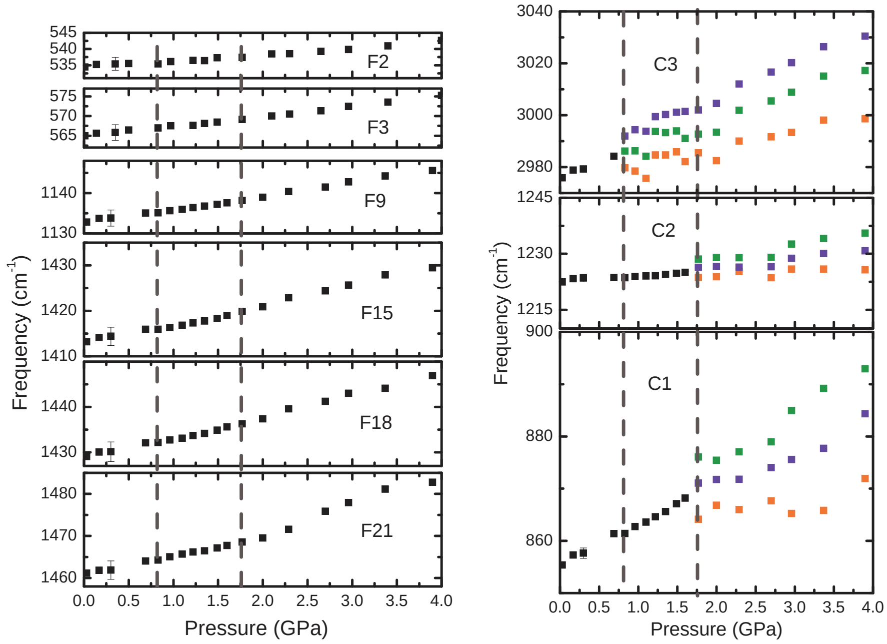

Figure 3.27: *Frequencies of the vibrational modes of $C_{70}{\cdot}C_8H_8$ plotted as function of pressure up to 4 GPa [121]. The vibrational modes of the fullerene (cubane) molecules are denoted by F (C); the labels are chosen according to Table 3.4. Only the fullerene modes with the largest pressure dependence are shown.*

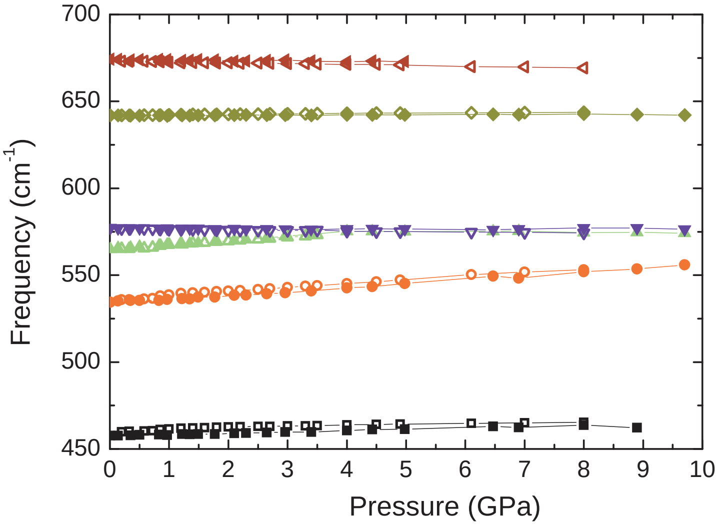

Figure 3.28: *Frequencies of the low-frequency (below 700 cm^{-1}) vibrational modes of $C_{70}{\cdot}C_8H_8$ (solid symbols) and the corresponding vibrational modes of C_{70} (hollow symbols) for pressure up to 10 GPa.*

anomaly at 0.5 GPa is attributed to the occurrence of an orientational ordering of the fullerene molecules in $C_{60}{\cdot}C_8H_8$, accompanied by the pressure-induced transition from an fcc to orthorhombic crystal structure as suggested by Raman and X-ray diffraction measurements under pressure [117].

In the fcc phase of $C_{60}{\cdot}C_8H_8$ the C_{60} molecules rotate so fast that the distorting potential field of the surrounding molecules is averaged out. The cubane molecules occupy O_h sites in these crystals, which is symmetry identical to the point group of the C_8H_8 molecule. This way no splitting is expected in the fcc phase. In the orthorhombic phase, on the other hand, the fullerene molecules are static. The highest possible site symmetry in orthorhombic $C_{60}{\cdot}C_8H_8$ is D_{2h}, and the irreducible representations of this point group are all one-dimensional. This means that splitting of both the C_{60} and the cubane lines should be present. As one unit cell of the orthorhombic phase contains 4 inequivalent molecules of fullerene (and cubane), Davydov splitting[1] should also be present. Any splitting up to the highest measured pressures was not observed, which means that the broadening due to the increase of pressure is larger than the magnitude of the splitting.

The anomaly at around 1.3 GPa cannot be assigned to the pressure-induced change of the orientational order in the p-T phase diagram of pure C_{60}, since the orthorhombic structure precludes orientational disorder. Besides, due to the larger interfullerene distances in $C_{60}{\cdot}C_8H_8$, the significant interaction is that of fullerene-cubane rather than fullerene-fullerene. Therefore, this transition may have its origin in fullerene-cubane interactions. Another indirect evidence for this assumption is that the infrared

---

[1] The (factor-group) splitting of bands in the electronic or vibrational spectra of crystals due to the presence of more than one (interacting) equivalent molecular entity in the unit cell.

Table 3.5: *Splitting of the originally infrared active molecular modes in the primitive monoclinic phase of $C_{70}\cdot C_8H_8$ according to group theory: a) the number of modes arising due to the lower site symmetry; b) the number of modes if we take Davydov splitting into account, as well [121]. The two possible splitting patterns are associated with different possible factor groups and site symmetries in the primitive monoclinic system.*

		a)	b)
C_{70}	A"$_2$	1	2
C_{70}	E'$_1$	2	4
C_8H_8	T_{1u}	3	6

modes of cubane follow the same pressure dependence as the fullerene lines showing anomalies at the same pressure values.

According to our results, the vibrational modes in $C_{70}\cdot C_8H_8$ exhibit a stronger and fundamentally different pressure dependence than those in $C_{60}\cdot C_8H_8$. The cubane modes split into several lines at 0.8 and 1.75 GPa where changes (although less pronounced) appear in the pressure dependence of the C_{70} modes as well. At room temperature the basic motion of the C_{70} molecules is a uniaxial rotation around the long molecular axis (C_5) [114,116]. This uniaxial rotation of the C_{70} molecules might stop at around 0.8 GPa, in analogy with the pressure-induced orientational ordering in pristine C_{70} at around 1 GPa [85,86,98].

In the bct phase of $C_{70}\cdot C_8H_8$ the cubane molecules occupy axially elongated O_h sites belonging to the D_{4h} point group. In this point group the T_{1u} modes split into A_{2u} and E_u, which are both infrared active. Consequently a twofold splitting of the cubane lines should be already present at ambient pressure. The size of the splitting, however, is below the resolution of the measurements, indicating only a slight elongation of the O_h site. C_{70} is rotating in this phase, and we indeed do not see any splitting of its lines.

In the primitive monoclinic phase the C_{70} molecules are not rotating any more, so splitting due to the lower site symmetry and the Davydov splitting can appear not only in the case of cubane, but also in the case of C_{70} lines. The highest possible site symmetry in this phase is C_{2h}. As this point group has only one-dimensional representations, the E_1' lines of C_{70} are expected to split twofold and the T_{1u} lines of cubane threefold (see column a) in Table 3.5). An additional twofold Davydov splitting of all the modes is expected, as the unit cell now contains two inequivalent

C_{70} (and C_8H_8) molecules (see column b) in Table 3.5). Of course, not all of the modes are infrared active. The number of these depends on the exact point groups appearing in the group theoretical derivation. If we consider all the possible cases of a primitive monoclinic $C_{70}\cdot C_8H_8$, the possible splitting patterns appearing in the infrared spectrum can be according to either column a) or column b) in Table 3.5. The splitting of C_{70} lines was not observed, but the cubane lines were indeed found to split with increasing pressure. It is interesting to note that the splitting of different T_{1u} lines of cubane does not happen at the same pressures. The origin of such difference remains an open question.

As mentioned earlier in Section 3.3, it was observed that cubane explodes spontaneously at room temperature at pressures above 3 GPa [113]. This decomposition is the result of the considerable internal strain caused by the unusual 90 degree bond angles, rendering the cubane molecule more sensitive to the application of external pressure than fullerenes. As the cubane sublattice is already ordered and there is no cubane-cubane contact, neither the orientational ordering calculated for the high-temperature phase of solid cubane [111] nor the bulk modulus estimation for the ordered phase [112] is relevant here; the principal factor determining the symmetry change is the ordering of the surrounding fullerene molecules. As we have seen, the splitting of the lines predicted by group theory is usually obscured by the linewidth, the only exception being that of cubane in $C_{70}\cdot C_8H_8$ under pressure. This indicates the sensitivity of the cubane molecule to pressure, and stronger intermolecular interactions in $C_{70}\cdot C_8H_8$ than in $C_{60}\cdot C_8H_8$.

Absorption edge

As explained in the discussion on the absorption edge of pure C_{70}, the energy of the onset of the electronic absorption can serve as a measure of the strength of intermolecular interactions. For the same reason, the absorption edge E_a in $C_{60}\cdot C_8H_8$ and $C_{70}\cdot C_8H_8$ and its dependence on external pressure were determined from our transmittance spectra. Figure 3.29 shows the absorbance spectra of both compounds in the NIR-visible frequency range for selected pressure up to 10 GPa. For both compounds the absorption edge shifts to lower energies on applying pressure. The absorption edge of $C_{70}\cdot C_8H_8$ lies at a smaller energy and shows larger pressure-induced shifts compared to $C_{60}\cdot C_8H_8$. The absorption strongly increases towards the low energy range due to the onset of the electronic excitations in fullerenes (cubane is transparent up to 50000 cm^{-1} [107]).

The quantitative analysis was performed similar to the analysis for the absorption edge of C_{70}, taking the first derivative of the absorption spectrum (see inset of Fig-

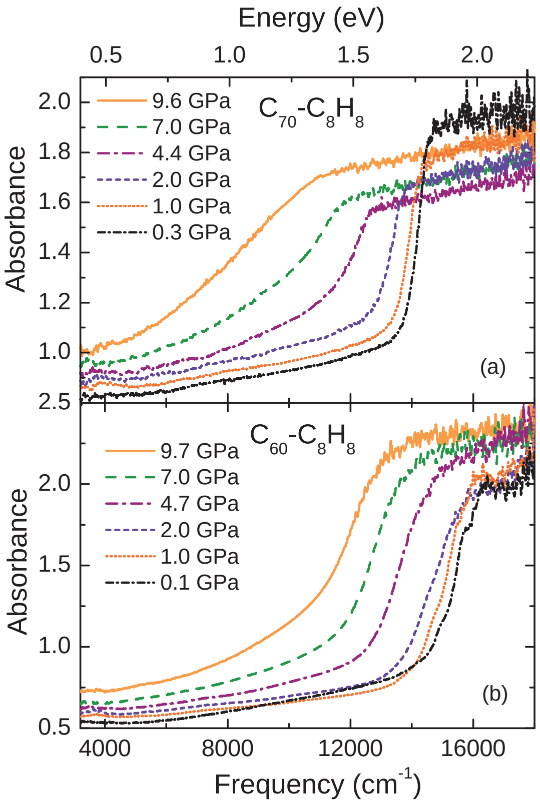

Figure 3.29: *Absorption spectra of (a)* $C_{60}{\cdot}C_8H_8$ *and (b)* $C_{70}{\cdot}C_8H_8$ *in the NIR to visible frequency range for selected pressures between 0 and 10 GPa, using KCl as pressure transmitting medium [121].*

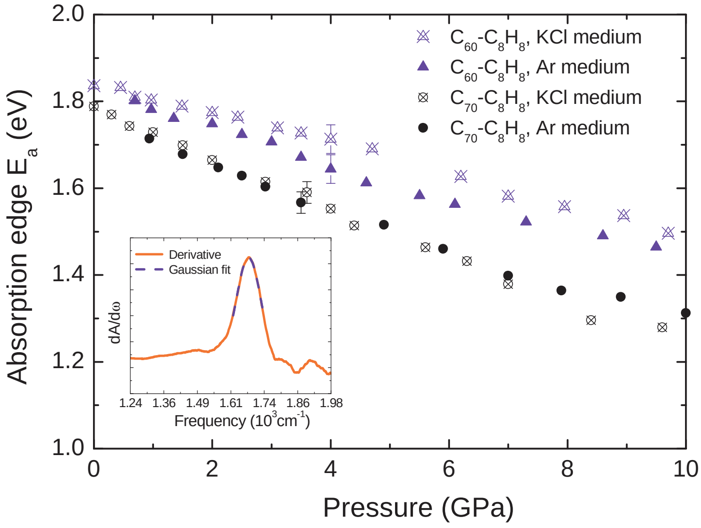

Figure 3.30: *Absorption edge* E_a *of* $C_{60}{\cdot}C_8H_8$ *and* $C_{70}{\cdot}C_8H_8$ *obtained from transmission measurements using KCl and argon as pressure transmitting media plotted as a function of pressure [121]. The inset shows, as an example, the derivative of the absorption spectrum measured at 1.5 GPa with respect to frequency,* $dA/d\omega$*; the energy position of the maximum, as determined from a Gaussian fit (dashed line), served as an estimate for the size of* E_a*.*

Table 3.6: *Ambient-pressure absorption edge E_{a0} and average interfullerene distance in various fullerene-based materials [43, 60, 85, 101, 105, 122, 126–132].*

Compound	E_{a0} (eV)	Intermolecular distance (Å)
C_{60}	1.73	10.01
C_{60}-clathrates	1.81	$\approx$ 10.1
$C_{60}\cdot C_8H_8$	1.84	10.42
C_{70}	1.79	10.61
$C_{70}\cdot C_8H_8$	1.77	10.88

ure 3.30 for illustration). The resulting pressure dependence of E_a for $C_{60}\cdot C_8H_8$ and $C_{70}\cdot C_8H_8$ is shown in Figure 3.30.

The results were rechecked using argon as pressure transmitting medium, in order to rule out possible non-hydrostatic effects. According to Figure 3.30 the values of E_a for the different pressure media agree reasonably well.

The dependence of E_a on pressure P for $C_{60}\cdot C_8H_8$ and $C_{70}\cdot C_8H_8$ is nonlinear and could be perfectly described by a second-order polynomial $E_a(P)=E_{a0}+ d_1\cdot P + d_2\cdot P^2$. The so-obtained fitting parameters are E_{a0}=1.84 eV (1.77 eV), d_1=-0.055 eV/GPa (-0.065 eV/GPa), and d_2=0.0015 eVGPa^{-2} (0.0018 eVGPa^{-2}) for $C_{60}\cdot C_8H_8$ ($C_{70}\cdot C_8H_8$). The nonlinear shift is analogous to that found in pristine C_{60} [60, 122, 123] and C_{70} (see Section 3.2.2), and the parameter d_1 for $C_{60}\cdot C_8H_8$ is comparable to that observed by Meletov *et al.*, [124–126] for the 1.7 eV threshold at low pressure.

The effect of the chemical pressure on the electronic properties of $C_{60}\cdot C_8H_8$ and $C_{70}\cdot C_8H_8$ was studied by a comparison with other fullerene-based materials regarding the absorption edge $E_a(0)$ and interfullerene distance. In Table 3.6 the results from this project are listed together with those for the pristine fullerenes and fullerene clathrates. The absorption threshold values for the other fullerene-derived compounds were determined by the same procedure described above, in order to be comparable. The size of $E_a(0)$ for $C_{60}\cdot C_8H_8$ is significantly larger than for pure solid C_{60} [60,105,122, 126]. A similar blueshift of the absorption edge compared to pure C_{60} was observed for the C_{60} clathrates [127]. Here it was argued that the blueshift results from the increase in molar volume, leading to a decrease in the molecular overlap between the C_{60} molecular orbitals: the guest molecules in the clathrates simply act as spacers, causing a lattice expansion, and no interaction is present between the host and guest molecules. A similar argument might hold in the case of $C_{60}\cdot C_8H_8$, but despite the much larger interfullerene distance than that in clathrates [116], the absorption edge does not differ much from that in the clathrates. This fact can be regarded as an evidence for the attractive fullerene-cubane molecular recognition [115] increasing the orbital overlap and thereby counteracting the spacer effect. Recent band-structure calculations [133] indeed raised the possibility of hybridization between cubane and C_{60}, which would have as a consequence the increase in heteromolecular overlap. It seems that in $C_{70}{\cdot}C_8H_8$ these two contributions nearly cancel each other, since no significant shift of the absorption edge compared to pristine C_{70} is observed. $C_{70}{\cdot}C_8H_8$ having a more effective space filling than $C_{60}{\cdot}C_8H_8$ explains the increased molecular recognition interaction which leads to both smaller increase in intermolecular distance and no shift (in fact, a slight redshift) in the absorption edge.

3.5 Summary

Pressure-dependent infrared spectroscopic measurements on fullerene-based compounds pristine C_{70}, $C_{60}{\cdot}C_8H_8$, and $C_{70}{\cdot}C_8H_8$ were performed over a broad energy range for pressure up to 10 GPa. Both vibrational and electronic properties of these compounds could be investigated under pressure.

Several fundamental vibrational modes of solid C_{70} could be identified and they were found to exhibit significant pressure dependence. In addition to the fundamental vibrational modes, few other modes which are probably Raman or silent modes activated due to intermolecular interactions and symmetry breaking effects, were also observed. An anomaly found in the pressure dependence of the vibrational modes of C_{70} at around 0.8 GPa, could be attributed to the orientational ordering transition where the uniaxial motion of the fullerenes is completely stopped. The orientational ordering transition is probably accompanied by a structural phase transition from fcc to rh. This conclusion is further supported by the fact that the weak vibrational modes begin to gain intensity with increasing pressure starting from the pressure around 1 GPa. The electronic absorption of solid C_{70} could be studied as a function of pressure from the NIR-visible spectra. The electronic absorption edge of the C_{70} was found at 1.77 eV. The optical absorption edge shifted to lower energies with increasing pressure due to increasing intermolecular interactions. The negative pressure coefficient of -0.077 eV/GPa agrees well with the expected deformation potential of C_{70}.

Pressure-dependent transmittance measurements over a broad frequency range (infrared to visible) on $C_{60}{\cdot}C_8H_8$ and $C_{70}{\cdot}C_8H_8$ reveal pressure-induced phase transitions and give an insight into the nature of interactions in this new class of rotor-stator compounds. The pressure dependence of the vibrational modes in $C_{60}{\cdot}C_8H_8$ shows anomalies at 0.5 and 1.3 GPa, the first of which could be assigned to a pressure-induced orientational ordering transition of the fullerene molecules; the second anomaly is probably correlated with fullerene-cubane interactions. According to the pronounced pressure-induced changes of the vibrational modes, the cubane molecules in $C_{70}{\cdot}C_8H_8$ are more sensitive to the application of pressure than in $C_{60}{\cdot}C_8H_8$, reflecting the stronger molecular recognition interactions in $C_{70}{\cdot}C_8H_8$ due to more effective space filling. The cubane modes exhibit pressure-induced splittings into several lines at 0.8 and 1.75 GPa, and are interpreted in terms of symmetry changes in the cubane molecules induced by distortions.

The energy of the absorption threshold in $C_{60}{\cdot}C_8H_8$ and $C_{70}{\cdot}C_8H_8$ could be followed as a function of pressure. For both compounds the threshold shifts to lower energies with increasing pressure due to an increasing overlap of the molecular orbitals, and the pressure dependence can be described by a second-order polynomial. The absorption threshold of $C_{60}{\cdot}C_8H_8$ is larger than that of pristine C_{60} but less than expected based on intermolecular distance, indicating that the cubane molecules do not simply act as spacers reducing the overlap of the C_{60} molecular orbitals, but heteromolecular overlap caused by molecular recognition plays a role as well. In $C_{70}{\cdot}C_8H_8$ practically no shift of the optical absorption edge is observed, in agreement with the enhanced molecular recognition interactions compared to $C_{60}{\cdot}C_8H_8$.

4 Single-walled Carbon nanotubes

In this chapter, the pressure-dependent investigations on the SWCNT films are presented. Investigations have been performed on both unoriented SWCNT films (an as-prepared SWCNT film and a purified SWCNT film) and oriented SWCNT films (oriented nanotubes in polyethylene matrix and magnetically-aligned nanotube film). An introduction to the properties of the SWCNTs is presented in the first section. The following sections explain the results of the various investigated films and the pressure-induced phenomena in SWCNTs.

4.1 Properties of Carbon Nanotubes

4.1.1 Structure

SWCNTs can be viewed as a hollow cylinder rolled from a graphitic sheet. Because the microscopic structure of SWCNTs is closely related to that of graphene, the tubes are usually labeled in terms of the graphene lattice vectors. Figure 4.1 illustrates the construction of a SWCNT from graphene sheet. The structure of the nanotubes can be specified by the wrapping vector (also known as chiral vector) $\mathbf{C}(n_1, n_2)$ which connects the crystallographically equivalent sites ($\mathbf{A}$ and $\mathbf{A}'$) on the graphene sheet. SWCNT's geometry is then completely specified by the pair of integers n_1 and n_2 denoting the relative position $\mathbf{C} = n_1\mathbf{a}_1 + n_2\mathbf{a}_2$ of the pair of atoms on a graphene strip which, when rolled onto each other, form a tube. The vectors $\mathbf{a}_1$ and $\mathbf{a}_2$ are the unit vectors of the hexagonal honeycomb lattice of the two-dimensional graphene. Depending on the wrapping vector $\mathbf{C}(n_1, n_2)$ and the chiral angle (the angle between the wrapping vector and zig-zag direction of graphene sheet; denoted as θ), the nanotubes are classified as *zig-zag*, *chiral* and *armchair* tubes (see Figure 4.2 for illustration). The tubes of type $n_2 = 0$ and $\theta = 0°$ are called zig-zag tubes. The tubes with $n_1 = n_2$ and $\theta = 30°$ are called armchair tubes and all other tubes are known as chiral tubes. The chiral vector defines the circumference of the tube and therefore the diameter (d) of the single-walled nanotubes is given by

$$d = \frac{|\mathbf{C}|}{\pi} = \frac{a_0\sqrt{n_1^2 + n_1 n_2 + n_2^2}}{\pi} \tag{4.1}$$

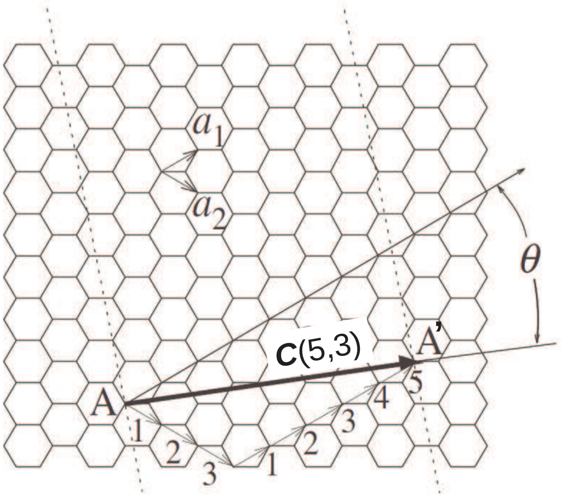

Figure 4.1: *Graphene honeycomb network with lattice vectors* $\boldsymbol{a}_1$ *and* $\boldsymbol{a}_2$. *The chiral vector* $\boldsymbol{C}_h = 5\boldsymbol{a}_1 + 3\boldsymbol{a}_2$ *represents a possible wrapping of the two-dimensional graphene sheet into a tubular form. The direction perpendicular to* $\boldsymbol{C}$ *is the tube axis. The chiral angle* θ *is defined by the* $\boldsymbol{C}$ *vector and the* $\boldsymbol{a}_1$ *zigzag direction of the graphene lattice [134].*

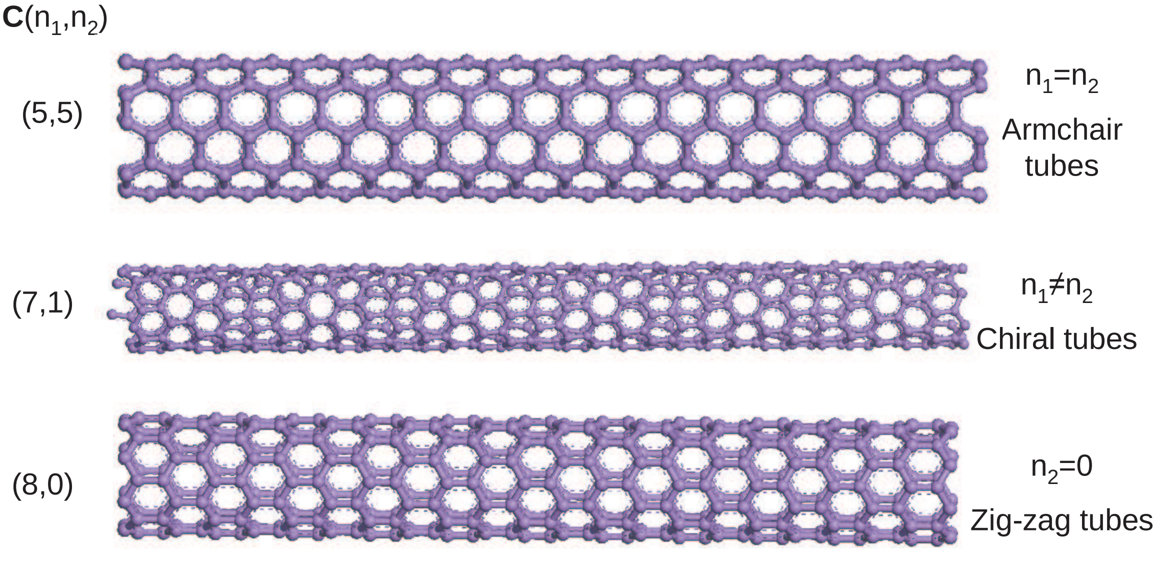

Figure 4.2: *Classification of the nanotubes based on the wrapping vector* $\boldsymbol{C}(n_1, n_2)$.

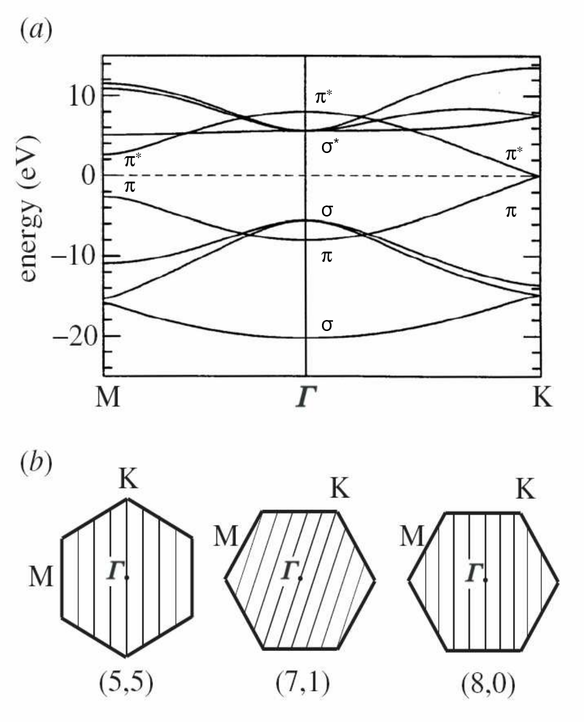

Figure 4.3: *(a) Band structure of the graphene based on the tight-binding model along the high-symmetry points (K, Γ and M). (b) Allowed **k** wavevectors of the (5,5), (7,1) and (8,0) tubes (solid lines) mapped onto the graphene Brillouin zone (hexagons) [135].*

where a_0 is the length of the basis vectors of the graphene lattice and is equal to 2.461 Å.

4.1.2 Electronic properties

The electronic properties of the SWCNTs can be obtained from the band-structure of graphene using the zone-folding approximation. The electronic band-structure of graphene is shown in Figure 4.3(a). The most widely used description of the electronic band structure of graphene is an empirical tight-binding model. This model includes only the π states perpendicular to the graphene sheet, i.e., the electrons in the p_z orbitals, and their interactions, because these states give rise to the electronic bands close to the Fermi level. Both the π valence band and the π^* conduction band cross at the $\boldsymbol{K}$ point of the Brillouin zone, while the σ bonding and σ^* antibonding bands are well separated in energy (see Figure 4.3(a)). Under the approximations which consider only the nearest-neighbor interactions in the graphene sheet and neglect the overlap between two π wavefunctions centered at different atoms, the π valence E^- and π^* conduction bands E^+ of graphene are given by the simple analytic expression [136,137]

$$E^{\pm}(k) = \pm\gamma_0\sqrt{3 + 2\cos(\mathbf{k}\cdot\mathbf{a}_1) + 2\cos(\mathbf{k}\cdot\mathbf{a}_2) + 2\cos(\mathbf{k}\cdot(\mathbf{a}_1-\mathbf{a}_2))} \quad , \qquad (4.2)$$

where γ_0 describes the interactions between two π electrons. $\mathbf{k}$ is the electronic wavevector for the graphene Brillouin zone.

Single-walled carbon nanotubes are one-dimensional solids: Due to this fact, the properties along the nanotube axis and perpendicular to tube axis differ significantly. Because of the periodic boundary conditions, the electrons, phonons and other quasiparticles can only have certain, discrete wavelengths along the nanotube circumference [137]. On the other hand, quasiparticles can travel along the nanotube axis. An infinitely long tube has continuous electronic and vibrational states in this direction. The quantization condition can be used to estimate the electronic band structure of carbon nanotubes from the electronic states of graphene. The electronic states are restricted to the $\boldsymbol{k}$ wavevectors that fulfill the condition $\mathbf{k} \cdot \mathbf{C} = 2\pi m$, where $\mathbf{C}$ is the chiral vector and m is an integer (see Figure 4.3(b) for illustration of the allowed $\boldsymbol{k}$ wavevectors for the three types of the nanotubes). It is this quantization condition that makes one-third of the nanotubes metallic while the others are semiconducting. The $\boldsymbol{K}$ point of graphene is at $\frac{1}{3}(\mathbf{k}_1 - \mathbf{k}_2)$ where $\mathbf{k}_1$ and $\mathbf{k}_2$ are the reciprocal lattice vectors of hexagonal graphene lattice; thus, a nanotube is a metal if

$$\mathbf{k} \cdot \mathbf{C} = \frac{1}{3}(\mathbf{k}_1 - \mathbf{k}_2)(n_1\mathbf{a}_1 + n_2\mathbf{a}_2) = \frac{2\pi}{3}(n_1 - n_2) = 2\pi m \tag{4.3}$$

i.e., the tubes with wrapping vector satisfying the condition,

$$3m = n_1 - n_2 \quad , \tag{4.4}$$

are metallic while other tubes are semiconducting. The armchair tubes with $n_1 = n_2$ are therefore always metallic while the zig-zag and chiral tubes are metallic when their chiral indices satisfy the condition specified in Eqn.(4.4). Inserting the allowed wavevectors (see Table 1 of [138] for more information) in the Eqn.(4.2), the electronic band structure of zig-zag, armchair and chiral SWCNTs can be obtained using zone-folding approximation as

$$\begin{aligned} E_{zz}^{\pm}(m, k_z) &= \pm\gamma_0 \sqrt{3 + 2\cos\left(2\pi\frac{m}{n}\right) + 4\cos\left(\pi\frac{m}{n}\right) \cdot \cos(\pi k_z)} \quad , && (4.5) \\ E_{ac}^{\pm}(m, k_z) &= \pm\gamma_0 \sqrt{3 + 4\cos\left(\pi\frac{m}{n}\right) \cdot \cos(\pi k_z) + 2\cos(2\pi k_z)} \quad , && (4.6) \end{aligned}$$

and

$$\begin{aligned} E_c^{\pm}(m, k_z) = \pm\gamma_0 \Bigg[3 &+ 2\cos\left(m\frac{2n_1 + n_2}{qnR} - \frac{n_2}{q}k_z\right) \\ &+ 2\cos\left(m\frac{2n_2 + n_1}{nqR} + \frac{n_1}{q}k_z\right) \\ &+ 2\cos\left(m\frac{n_1 - n_2}{qnR} - \frac{n_1 + n_2}{q}k_z\right)\Bigg]^{\frac{1}{2}} \quad , \end{aligned} \tag{4.7}$$

where the subscripts zz, ac and c refer to zig-zag, armchair and chiral tubes, respectively. k_z is the magnitude of the axial wavevector which is continuous. The number n is the greatest common divisor of the chiral indices n_1 and n_2. The parameters q is the number of graphene hexagons in the nanotube unit cell. The parameter R given in the dispersion relation for the chiral tubes is also a function of the chiral indices given as

$$R = \begin{cases} 3 & \text{if } (n_1\text{-}n_2)/3n = \text{integer} \\ 1 & \text{if } (n_1\text{-}n_2)/3n \neq \text{ integer} \end{cases}$$

The k_z wavevector at which the valence band crosses the conduction band in the nanotube Brillouin zone can be obtained by projecting **K** point along the nanotube axis as

$$k_z = \begin{cases} 0 & \text{if R=1} \\ 1/3 & \text{if R=3} \end{cases}$$

Thus, in metallic tubes with $R = 1$ like (n_1,0) zig-zag tubes, the valence and the conduction band cross at the Γ point. In $R = 3$ tubes, they cross at one-third of the k_z lattice vector at $2\pi/3a$.

Electronic density of states

Although the electronic band structure of the SWCNTs is in close analogy to that of graphene, the most important difference arises due to the reduced dimensionality. The density of states (DOS), *i.e.*, the number of available electrons for a given energy interval, is known to depend dramatically on the dimension of a system. It is this quantity that is extremely crucial for the experimental study of the electronic properties of the nanotubes and its applications. As carbon nanotubes are one-dimensional, $1/\sqrt{E}$-behavior for the DOS is expected, if $E \propto k^2$. It was indeed found that the DOS exhibited this behavior and an universal expression for the DOS of the carbon nanotubes was derived by Mintmire and White [139]. The DOS $n(E)$ for i one-dimensional electronic bands is given by

$$n(E) = \frac{2}{q|k_z|} \sum_i \int dk_z \delta(k_z - k_i) \left| \frac{\partial E^{\pm}(k_\perp, k_z)}{\partial k_z} \right|^{-1} \quad , \tag{4.8}$$

where k_i is given by $E - E^{\pm}(k_\perp, k_z) = 0$ and $q|k_z|$ is the total area of the nanotube Brillouin zone. The partial derivative of $E^{\pm}$ close to the Fermi level can be calculated by approximating the electronic bands of graphene as straight lines close to **K**. The electronic band of graphene close to **K** is then given as

$$E^{\pm}(\mathbf{k}) = \mp \frac{\sqrt{3}}{2} a_0 \gamma_0 \left| \mathbf{k} - \mathbf{k}_F \right| \quad . \tag{4.9}$$

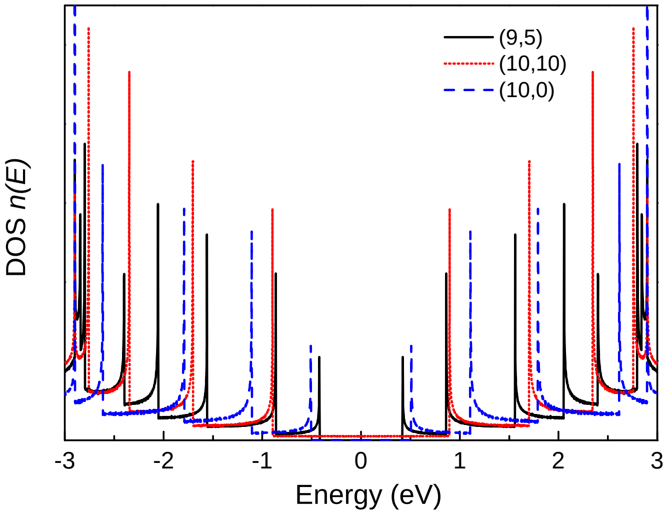

Figure 4.4: *Density of states of the nanotubes with chiral indices (9,5), (10,0) and (10,10) as examples for density of states of the chiral, armchair and zig-zag SWCNTs.*

An allowed wave vector of a tube is given by $m\mathbf{k}_\perp$ plus a vector along $\mathbf{k}_z$, thus

$$|\mathbf{k}-\mathbf{k}_F| = \sqrt{\Delta k_m^2 + \Delta k_z^2} \quad , \tag{4.10}$$

where Δk_m is the quantized component along $\mathbf{k}_\perp$, and Δk_z is the component parallel to $\mathbf{k}_z$ and can have continuous values. Δk_m can be obtained by projecting $(\mathbf{k}-\mathbf{k}_F)$ along $\mathbf{k}_\perp$ as

$$\Delta k_m = (\mathbf{k}-\mathbf{k}_F)\frac{\mathbf{k}_\perp}{|k_\perp|} = \frac{4\pi}{3\,|\mathbf{c}|}\,|3m - n_1 + n_2| = \frac{4}{3d}\,|3m - n_1 + n_2| \tag{4.11}$$

The inverse of the partial derivative in Eqn.(4.8) is then given by the expression

$$\left|\frac{\partial E^\pm(k_\perp,k_z)}{\partial k_z}\right|^{-1} = \frac{\sqrt{3}}{2}a_0\gamma_0\left|\frac{\partial\sqrt{\Delta k_m^2+\Delta k_z^2}}{\partial k_z}\right|^{-1} = \frac{\sqrt{3}}{2}a_0\gamma_0\frac{|E^\pm|}{\sqrt{(E^\pm)^2 - E_m^2}} \quad , \tag{4.12}$$

with

$$E_m = \frac{\sqrt{3}}{2}a_0\gamma_0\Delta k_m = |3m - n_1 - n_2|\,\frac{a_0\gamma_0}{\sqrt{3}d} \quad . \tag{4.13}$$

Inserting Eqn.(4.12) in to Eqn.(4.8) and integrating over k_z, the DOS of SWCNT is given as

$$n(E) = \frac{8}{q|k_z|}\sum_{m=-\infty}^{\infty}\frac{2}{\sqrt{3}a_0\gamma_0}g(E,E_m) \quad . \tag{4.14}$$

Since the volume of the Brillouin zone $q|k_z| = 4\pi^2 d/\sqrt{3}a_0^2$,

$$n(E) = \frac{4a_0}{\pi^2 d\gamma_0}\sum_{m=-\infty}^{\infty} g(E,E_m) \quad , \tag{4.15}$$

with

$$g(E, E_m) = \begin{cases} |E|/\sqrt{E^2 - E_m^2} & |E| > |E_m| \\ 0 & |E| < |E_m| \end{cases}$$

$g(E, E_m)$ for $E_m \neq 0$ shows the divergence at $E = E_m$. For $E_m = 0$, g is equal to 1 and refers to metallic tubes and the electronic bands that cross at the Fermi energy. The points of energies of vanishing slope for the different electronic bands are given by E_m which is defined as

$$E_m = |3m - n_1 - n_2| \frac{a_0 \gamma_0}{\sqrt{3}d} \tag{4.16}$$

Thus, the DOS of the SWCNTs depends on the chirality and is inversely proportional to the diameter (d) of the nanotubes. Figure 4.4 shows the DOS for (9,5) (chiral), (10,0) (armchair), and (10,10) (zig-zag) nanotubes as examples for the DOS of the three types of SWCNTs. The DOS consists of van Hove singularities (vHS) at various energies satisfying the condition $E = E_m$. Considering nanotubes with similar diameters, the first vHS in a semiconducting tube is found at lower energies than that of the metallic tubes. The $1/d$ dependence of the energy gap in the DOS relies on the assumption of a linear dispersion of the bands around E_F. In reality, the bands are not linear away from E_F, an effect called trigonal warping which induces a dependence of the band gap not only on the diameter, but on the (n_1,n_2) indices as well [140, 141].

Curvature effects

The electronic band structure of SWCNTs described in the previous section is a model based on the confinement of electrons around the tube circumference. Within this model, the curvature effects that arise due to the fact that the carbon atoms are placed on a cylindrical wall of the carbon nanotubes were neglected, since the states selected in the band-folding scheme were those of the planar graphene sheet. However the curved topology induces several effects different from those of a planar graphene sheet. They are:

- **Secondary gap/Curvature-induced gap:** The C-C bonds perpendicular and parallel to the axis are slightly different, so that the $\mathbf{a}_1$ and $\mathbf{a}_2$ basis vectors now have different lengths. Due to the bond length changes, a finite angle is formed between the two p_z orbitals located on bonds not strictly parallel to the axis . This yield differences in the three hopping terms γ_0 between a carbon atom and its three neighbors.

  The crossing of the valence and conduction bands at the Fermi level is therefore modified by the curvature of the nanotube. For armchair nanotubes, taking

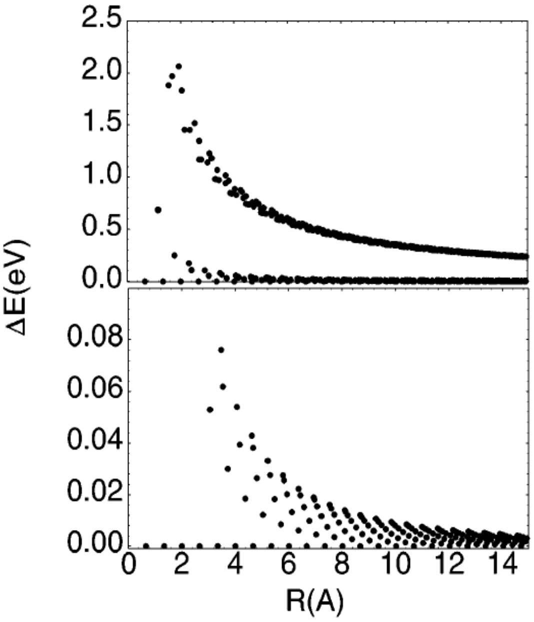

Figure 4.5: *Gaps calculated for all right circular tubes with radii less than 15 Å. Depending on the chirality and diameter, the tubes can be classified as those with primary gaps which scale as* $1/R$ *(top panel, top curve), those with zero primary gap but nonzero curvature induced gaps which scale as* $1/(2R)^2$ *(lower curve top panel, and shown in the expanded scale in the lower panel), and armchair tubes with zero primary gap and zero curvature induced gap [142].*

curvature into account shifts the Fermi wave vector along an allowed line of the graphene Brillouin zone, preserving their metallic character with finite curvature. However, for metallic nanotubes other than armchair tubes, k_F moves away from $\boldsymbol{K}$ point of the Brillouin zone perpendicularly to the allowed $\mathbf{k}$ lines such that the allowed 1D subband no longer crosses k_F, opening a very small band gap at E_F.

Thus, when accounting for curvature effects, the only zero-band-gap tubes are the (n_1,n_2) tubes with $n_1 = n_2$. The (n_1,n_2) tubes with $n_1 - n_2 = 3m$, where m is a nonzero integer, are tiny-gap semiconductors (gap of a few tenths of a meV) . All other nanotubes are intermediate-gap semiconductors (gap of a few 100 meV). For the tiny-gap semiconducting nanotubes, the so-called secondary gap or curvature-induced gap depends on the diameter and the chiral angle, and scales as $1/d^2$ (see Figure 4.5) [142]. Within the nearest-neighbor tight-binding description the secondary gap is given by

$$E_g = \frac{\gamma_0 a_0^2}{4d^2} \cos 3\theta \tag{4.17}$$

where a_0 is the lattice constant of graphene and θ is the chiral angle. The secondary gap is typically so small that, for most practical purposes, all $n_1 - n_2 = 3m$ tubes can be considered as metallic at room temperature. The DOS measurements by scanning tunneling spectroscopy confirm the expected $1/d^2$ dependence for three zigzag nanotubes and show that armchair nanotubes remain truly metallic [143].

- **Rehybridization effects:** The planar symmetry is broken so that the σ and the π states mix and form hybrid orbitals that exhibit partial sp^2 and sp^3 character. For small diameter tubes, the curvature is so strong that some rehybridization among the σ and π states appears. The first-principles pseudopotential local density functional (LDA) calculations indeed revealed that hybridization effects can occur in small diameter nanotubes sufficiently strong to significantly alter their electronic structure [144]. Strongly modified low-lying conduction band states are introduced into the band gap of insulating tubes because of hybridization of the σ^* and π^* states. As a result, the energy gaps of some small diameter tubes are decreased by more than 50% thus influencing the energies of the optical transitions. For nanotubes with diameters greater than 1 nm, these rehybridization effects may be unimportant. However, it can be understood in the later section that the deformation of these larger diameter nanotubes does influence the hybridization effects in SWCNTs, significantly (see Section 4.1.4).

Effect of nanotube bundling

SWCNTs grown by laser ablation, arc-discharge, or CVD method, always occur in bundles of 10-100 nanotubes. These bundles usually consist of nanotubes with different chirality and slightly different diameter. The understanding of the properties of a carbon nanotube bundle is even more complicated since even a “perfect” crystal made of identical tubes will alter the electronic properties (both close to and away from the Fermi level) of the constituent CNTs through interaction among different tubes.

- **Pseudogap:** The first-principles calculations revealed that the broken symmetry of the (10,10) tube caused by interactions between tubes in a bundle induces a pseudogap of about 0.1 eV at the Fermi energy [145]. This pseudogap strongly modifies many of the fundamental electronic properties of the armchair tubes, with a specific signature in the temperature dependence of the electrical conductivity and in the IR absorption spectrum.

  For example, in the limit of an isolated (10,10) tube, the crossing of the two bands at E_F is allowed due to the tube symmetry. Upon breaking of this symmetry by tube-tube interaction in the hexagonal bundle symmetry, these bands mix and repel at E_F (see Figure 4.6). This gap feature is distinct from the curvature-induced gaps discussed earlier, because the DOS are suppressed but not reduced completely to zero at E_F. For this reason, this feature is termed a pseudogap. The occurrence and the magnitude of this pseudogap which depends inversely on the nanotube radius, have been observed experimentally using low-temperature

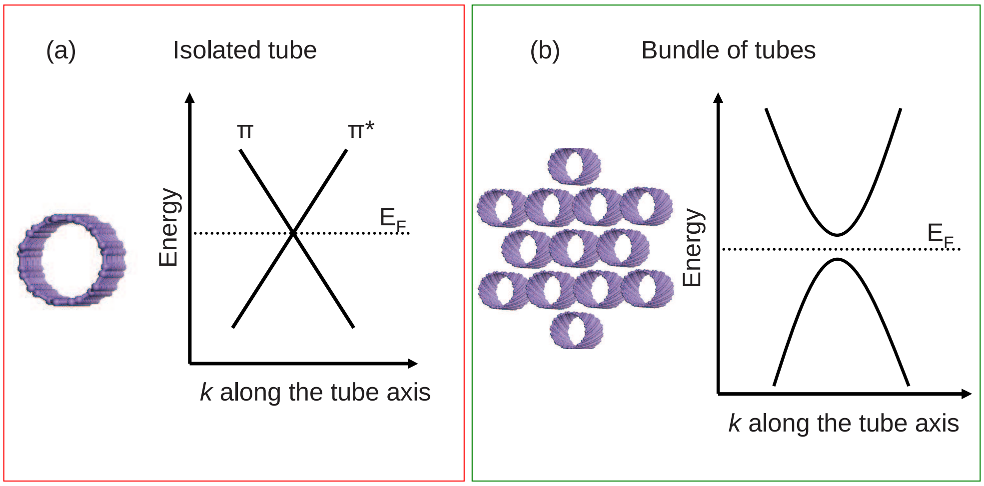

Figure 4.6: *(a) Schematic diagram of the crossing of the* π *and* π^* *bands at the Fermi level* (E_F) *for an isolated (n,n) carbon nanotube. (b) Simplified scheme of the repulsion of the bands at the* E_F *due to the breaking of mirror symmetry which leads to an opening of a gap [145].*

scanning tunneling spectroscopy [143]. In contrast, if (6,6) nanotubes are arranged in a hexagonal lattice its symmetry is preserved in the bundle, and the band gap due to these intertube interactions is not observed [146]. But, any small rotation of the (6,6) tubes in such an arrangement breaks the symmetry of the (6,6) bundle leading to an opening of the gap at the Fermi energy.

- **Influence on higher-energy electronic bands:** The symmetry breaking and the intratube dispersion perpendicular to tube axis not only affect the electronic structure close to the Fermi level but also the larger electronic energies. Figure 4.7 shows the comparison of the DOS calculated for few isolated and bundled armchair tubes. The intertube interactions induce shifts in the vHS in the DOS as high as 0.25 eV [148]. The vHS are also broadened due to the dispersion perpendicular to the 1D DOS and most of them consist of two peaks. The DOS was found to be more attenuated due to intertube interactions, and the spike structure of the singularities were smoothed out [149]. The valence and conduction bands exhibit splitting in the bundled nanotubes due to symmetry lowering. This effect of tube-tube interactions depends strongly on the nature of nanotubes, namely, the chirality. The changes in absorption bands due to the intertube interactions could be of the order 10 meV-1 eV [150].

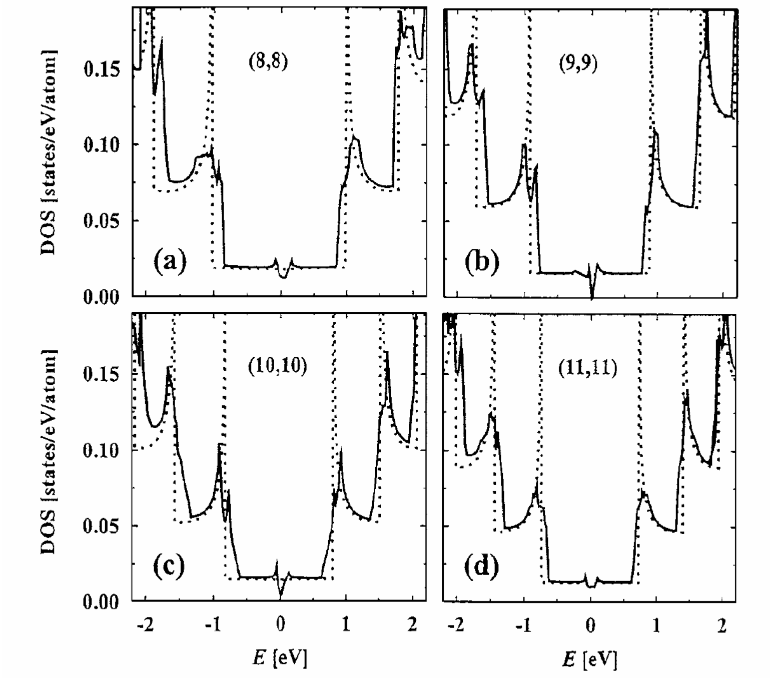

Figure 4.7: *Density of states of isolated (dotted lines) and bundled (solid lines) (a) (8,8), (b) (9,9), (c) (10,10), and (d) (11,11) carbon nanotubes. The attenuation, the broadening and the splitting of the vHS as isolated nanotubes bundle up into a close-packed triangular lattice are clearly visible [147].*

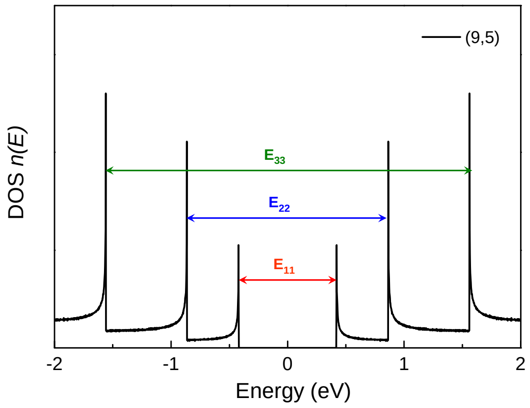

Figure 4.8: *Illustration of the optical transitions allowed according to the selection rules in (9,5) SWCNT. The optical transition occurs across the mirror image spikes of DOS within the single-particle picture.*

4.1.3 Optical properties

The optical spectroscopy of nanotubes is of major importance not only for potential applications of CNTs in optoelectronic devices, but for understanding the electronic properties. In particular, by means of optical investigations, it is possible to determine the chiral indices of the nanotubes. Moreover, by analyzing electronic properties of the carbon nanotubes, their electronic band structure may be understood.

Single-particle optical absorption and selection rules

Within the single-particle picture which ignores many-body effects, the absorption peaks can be mapped onto the energy differences between vHSs in the valence and

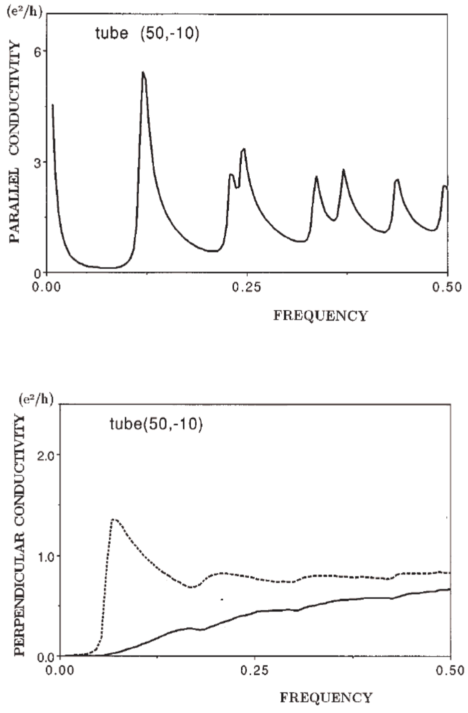

Figure 4.9: *Real part of parallel and perpendicular conductivity in units of* e^2/h *calculated for the (50,-10) tube of diameter 3.59 nm [152]. The optical conductivity for* $\mathbf{E}||$*tube axis is unaffected by the depolarization effect while that for* $\mathbf{E}\perp$*tube axis is strongly modified. The optical conductivities with and without depolarization effect for perpendicular to tubes axis are shown as broken and solid lines, respectively. It is also worth noticing that the energies of the peaks for polarization parallel and perpendicular to tube axis are different due to different absorption selection rules.*

conduction bands quite reliably. In the case of nanotubes, the optical spectrum is dominated by transitions between these spikes in the DOS [151]. Apart from the allowed vertical transitions ($\triangle k = 0$), the selection rules for these optical transitions in carbon nanotubes depend on the direction of the electric field vector relative to the tube axis. According to the selection rules, for the incident light polarized parallel to the tube the strongest optical transitions occur between the sub-bands with the same angular momentum, i.e., $\Delta q = 0$ where q is the angular momentum quantum number (the allowed optical transitions are shown in Figure 4.8). For the light polarized perpendicular to the tube axis, the angular quantum number changes by ±1. These selection rules yield the so-called E_{ii} transitions where i is the integer representing the number of the vHS involved. Thus, the optical transitions that are allowed in the optical absorption spectra of SWCNTs for $\mathbf{E}||$tube axis are E_{11}, E_{22}, E_{33} and so on, while those for $\mathbf{E}\perp$tube axis are E_{12}, E_{21} and so on.

Another important aspect of the optical absorption properties in carbon nanotubes is the strong quenching of the absorption by the depolarizing fields for light polarized in transverse directions known as depolarization or antenna effect. In this static approximation, this effect can be understood by considering the nanotubes as a long and narrow cylinder in an applied electric field. Therein, the polarization charges are not induced in an infinitely long cylinder for a field polarized along the tube axis, and the

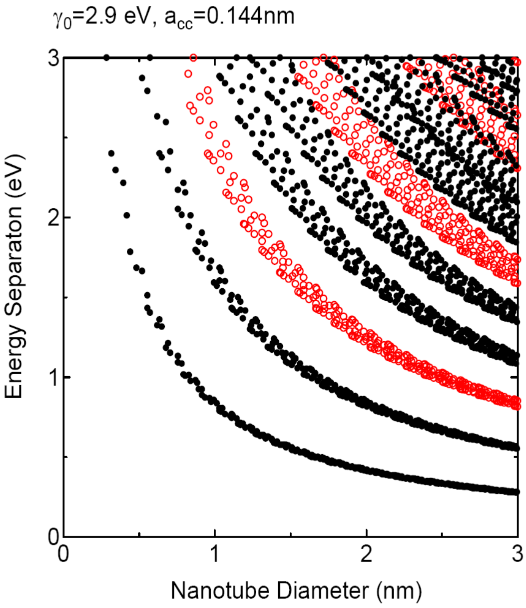

Figure 4.10: *Energy separation for all (n_1,n_2) calculated for SWCNTs of diameters up to 3 nm. The black and red symbols correspond to semiconducting and metallic nanotubes, respectively.*

electric field parallel to the cylinder length is equal to the applied field. In contrast, for the electric field applied perpendicular to the cylinder length, the charges are induced on the cylinder walls. The resulting polarization vector opposes the external field and therefore reduces the net field perpendicular to the cylinder length. This indeed strongly affects the optical absorption perpendicular to the tube axis. The effect of depolarization field on the optical conductivity for perpendicular to tubes axis is illustrated in Figure 4.9. The optical conductivity for polarization parallel to the tube axis consists of the optical absorption expected according to the selection rules without much influence of the depolarization effect. The optical transitions (in particular at lower energies) are instead almost completely screened out for perpendicular polarization when depolarization effect is taken into account.

As the DOS of the SWCNTs depends on the chirality, and is inversely proportional to the diameter of the nanotubes, the dependence of the energy of the optical transitions in SWCNTs may be mapped as a function of the nanotube diameter and chirality. This plot, known as Kataura plot, is shown in Figure 4.10. The spread of the transition energies within each curve corresponds to the differences arising due to strong chirality dependence of the transition energies (also known as family behavior). At higher energies, the spread of the closely-spaced transition energies makes the distinction between the various transitions rather difficult.

Excitonic effects

Although the standard single-particle band theory is sufficient to explain the basic properties of the carbon nanotubes, it is not sufficient to reach a complete understanding of the electronic properties as many-body correlation effects, especially excitonic effects are very important in this 1D system. This was realized when the absorption studies on well-calibrated (n_1,n_2) nanotubes showed evidence for some deviations from the analysis of Kataura *et al.* since the peaks in the absorption spectra and the E_{ii} transition energies in between vHS showed systematic deviations from that calculated using the single-particle picture [153, 154]. In particular, the ratio E_{22}/E_{11}, predicted to be equal to 2 in the approximation where bands are linear close to E_F [139], was found to be smaller [153]. Trigonal warping effects which can easily account for deviations from 2 of the E_{22}/E_{11} ratio in small SWCNTs could not account for the deviations in the limit of large tubes. This is the so-called ratio problem in SWCNTs [155]. Furthermore, a decrease of the photoluminescence intensity for SWCNTs with small chiral angles (zigzag tubes) was observed [153]. This effect could not be explained within the independent-electron model instead electron-hole interaction needs to be considered.

The electron-hole interaction when strong enough, leads to the formation of an exciton which is the bound state of a photo-excited electron and a hole. Generally, the binding energy of an exciton in 3D materials can be calculated using a hydrogenic model with a reduced effective mass and a dielectric constant. The energy levels of excitons with binding energy usually of the order of 10 meV appear as discrete levels just below the single-particle excitation spectra and therefore are observable in the optical absorption spectra only at low temperatures. However, in SWCNTs, the electron-hole interaction is larger and strong excitonic features are observable even at room temperature [156].

As the electron-hole interactions are screened by the itinerant carriers and electron-electron interactions, the excitonic effects will be predominant whenever the screening is weak i.e., in semiconducting tubes. Figure 4.11 illustrates the excitonic effect for a semiconducting (8,0) carbon nanotube calculated by Spataru *et al.* [157]. The optically-allowed interband transitions according to the single-particle band picture (labeled as A, B and C in Figure 4.11(a)) give rise to peaks (shown in Figure 4.11(b) with same labels) in the non-interacting optical spectrum. However, when electron-hole interactions are included, each non-interacting peak gives rise to series of visible exciton lines (labeled as A'_i, B'_i and C'_i where $i = 1, 2, 3\ldots$) with large binding energies. These exciton binding energies are significantly larger than the bulk semiconductors and qualitatively change the optical absorption spectrum. In the limit of an ideal 1D electron-hole system, the exciton binding energy becomes infinite [158]. This peculiar

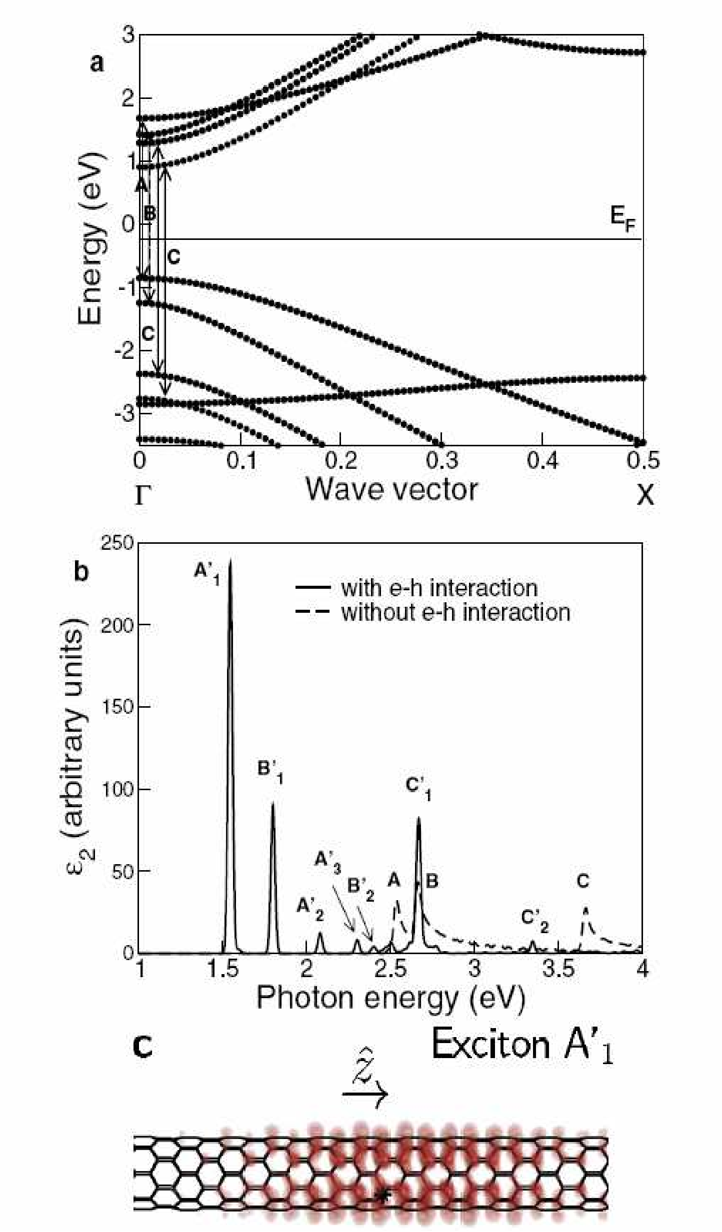

Figure 4.11: *Illustration of excitonic effect in nanotubes. (a) Quasiparticle band structure of (8,0) semiconducting nanotube; (b) Optical absorption spectra with and without electron-hole interaction for (8,0) tube (see text for detailed description); and (c) Real-space electron-hole pair probability distribution for a bound exciton [157].*

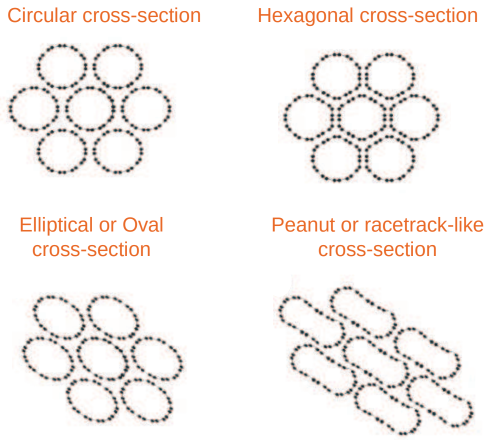

Figure 4.12: *Schematic sketch of (a) the original circular cross-section of single-walled carbon nanotubes arranged in a 2D triangular lattice, deforming under externally applied compression to (b) the hexagonal cross-section, (c) the elliptical or oval cross-section, and (d) the peanut or race-track-like cross-section [172].*

feature is the origin of the large enhancement of the oscillator strength of the 1D exciton. A considerable amount of the optical intensity is transferred to exciton bound states due to the 1D nature of the nanotubes [159].

4.1.4 SWCNTs under extreme conditions

An efficient approach towards understanding the properties of nanotubes under extreme conditions is to study the effect of temperature and pressure on the properties of carbon nanotubes

Earlier spectroscopic investigations show a very weak temperature dependence of the low energy properties of the SWCNTs [160–164]. This intriguing temperature-dependent property of nanotubes were suggested to be the consequence of the localization of carriers [162,165–167]. Recently, it was suggested that the weak temperature dependence is due to the significant spread of the chemical potential in a mixture of SWCNTs [168] Not only the low energy properties but also the optical band gaps at higher energies are expected to exhibit temperature dependence. The optical transitions shift to lower or higher energies with change in the temperature depending on the diameter and chirality of the nanotubes [169–171].

On the other hand, the application of high pressure affects the SWCNTs in the following way: (i) deformation of nanotubes due to external stress thereby inducing a structural phase transitions; (ii) changes in the intertube distances and in turn the effect of increasing interaction between adjacent tubes on the electronic properties of the SWCNTs; (iii) Effect of interaction of tubes with the surrounding environment (like surfactants, pressure transmitting medium etc.)

There is an enormous number of theoretical studies performed to investigate the pressure-induced structural deformations in nanotubes. The nanotubes deform on ap-

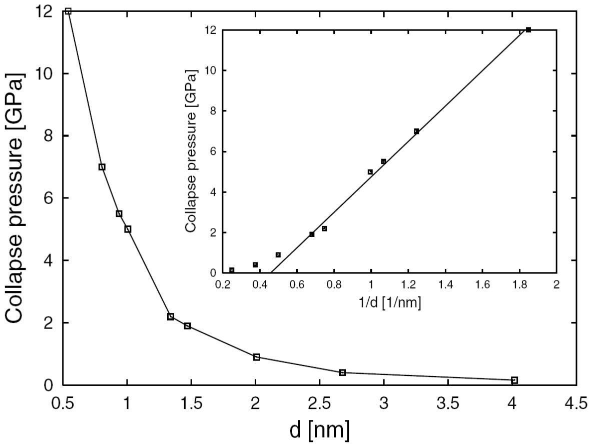

Figure 4.13: *Collapse pressure of SWCNT bundles as a function of tube diameter and (inset) as a function of reciprocal of diameter [173].*

plying pressure and the circular cross-section undergoes polygonization [174–176]. It has been suggested that the circular cross-section of nanotubes deforms to stabilize at oval, elliptical, racetrack-like or peanut-shaped cross-section (see Figure 4.12 for illustration of the cross-sections of deformed SWCNTs) [173, 175–180]. The nature of the phase transition and the deformation in the carbon nanotubes are extremely complex with the existence of metastable states, and high dependency on its diameter just like the other properties of nanotubes [173, 177, 181]. Although there are discrepancies in predictions of the high pressure phase of nanotubes, it is well established through both experimental and theoretical studies that the polygonization occurs at a certain critical pressure P_c. The value of P_c decreases with increasing nanotube diameter and follows the relation $\mathrm{P}_c \propto 1/\mathrm{d}^3$ (see Figure 4.13) for both individual nanotubes [178–181] and bundled nanotubes [173, 178–180].

The structural deformation in the carbon nanotubes induces significant changes in the electronic band structure [182–188]. The σ^*-π^* hybridization (see Curvature effects in Section 4.1.2) and symmetry-breaking effects become more important in polygonized or deformed tubes. The changes in the electronic properties of SWCNTs with polygonized cross-sections have been investigated theoretically by Charlier *et al.* using *ab-inito* local density functional calculations and simple tight-binding models [182]. It was found that the energy of the π^* states are dramatically reduced leading to a decrease in the bandgap in semiconducting carbon nanotubes. In addition to the enhanced rehybridization effects in the deformed tubes, the interaction between the facing layers in radially-deformed nanotube with oval or elliptical cross-section plays a very significant role [183, 184, 186]. Thus, the radial deformation in the SWCNTs could lead to the opening or closing of the gap at the Fermi level and thereby causing a an insulator-to-metal transition or vice-versa in metallic tubes or small-gap nanotubes [183–188].

Earlier investigations on the nature of the pressure-induced structural deformation of carbon nanotubes has been probed using Raman spectroscopy [189, 190], X-ray scattering [191, 192], neutron diffraction [193] and optical absorption [194]. The experimental studies present results with differences arising due to differences in the diameter distribution and chirality of the nanotubes present in the sample and its extremely sensitivity to synthesis and chemical processing like purification. In the high-pressure X-ray diffraction investigation, the decay of a diffraction peak for an as-prepared SWCNT bundles at ∼1.5 GPa was attributed to hexagonal deformation of the nanotube radius by Tang *et al.* [191] while this peak was observed up to 10 GPa for chemically-processed tubes by Sharma *et al.* [192]. Several Raman spectroscopic investigations also attribute the disappearance of the radial breathing mode (RBM) of the SWCNTs and a change in the pressure derivative of the frequency of the tangential mode ($\boldsymbol{G}$ band) at 1.5-2 GPa to radial deformation [172, 173, 189]. More recent high-pressure investigations on bundled SWCNTs estimates much higher collapse pressures. Raman spectroscopic investigations [195, 196] and the electrical transport measurement [197] found no signs for collapse or radial deformation of the SWCNTs for pressures up to 10-13 GPa. The absence of signatures for a structural deformation in SWCNTs in the Raman spectroscopic investigations were attributed to the effect of the interaction with the pressure transmitting medium [195, 196]. It was suggested that the adsorption and/or intercalation of the pressure transmitting media (especially argon) within the "open" nanotubes suppress the structural deformation in the high-pressure investigations [195, 196]. Furthermore, the resonant Raman studies on the individualized nanotubes under pressure also report higher critical pressures for radial deformation (10 GPa and 4 GPa for nanotubes of diameters 0.8-0.9 nm and 1.2-1.3 nm, respectively) [190]. It is obvious that in spite of the large numbers of extensive high-pressure investigations, the pressure-induced phenomena in the SWCNTs is yet to be throughly understood and the discrepencies have to be solved.

In general, many spectroscopic techniques like Raman spectroscopy and scanning tunneling spectroscopy, have been extensively used in the process of understanding the complex physics of carbon nanotubes. Infrared spectroscopy is a very useful tool that investigates the electronic properties of materials over a broad energy scale close to the Fermi level. Some investigations on nanotubes using infrared spectroscopy have been performed, in order to study the influence of temperature, doping and pressure [160, 164, 194, 198–200]. But many of the questions related to electronic properties especially low-energy properties, bandgap modifications, intertube interactions and also interaction between nanotubes and surrounding environment are yet to be answered.

Sample Type	Synthesis	d (nm)	Orientation	Avg. Thickness
As-prepared unoriented CNTs	Laser ablation	1.3 nm	-	200 nm
Purified unoriented CNTs	Laser ablation	1.3 nm	-	200 nm
Oriented SWCNTs embedded in polyethylene matrix	Laser ablation	1.4 nm	90% within 25°	25 μm
Magnetically-aligned SWCNT films	Laser ablation	1.34 nm	70%	10 μm

Table 4.1: *List of the samples investigated within this project and brief information on the morphological properties and synthesis technique.*

In an attempt to address the open issues, both temperature- and pressure-dependent investigations on the unoriented SWCNTs have been performed over a broad frequency range to compare the effect of the two extreme conditions, namely temperature and pressure. Furthermore, the infrared spectroscopic evidence for the pressure-induced structural phase transitions and its implications on the electronic band structure has been probed in both unoriented and oriented SWCNT films. Importantly, the pressure-induced changes in the electronic properties at energies below 50 meV, i.e., far-infrared (FIR) frequency range have been investigated for the first time for both unoriented and oriented SWCNT films.

4.2 Investigated nanotubes samples

Several nanotube films with both oriented and unoriented nanotubes have been investigated within this work. The unoriented SWCNT films were obtained from Dr. F. Hennrich from Institute of Nanotechnology at Forschungszentrum Karlsruhe, Germany. The film of oriented nanotubes in the polyethylene matrix was received from Prof. Y. Iwasa at Institute for materials research, Tohoku university, Japan while the magnetically-aligned film was obtained from Rice university, USA. Each nanotube film was prepared at specific conditions. The properties of the nanotubes, as mentioned in the Section 4.1, is highly dependent on the preparation and purification processes. It is therefore extremely important to understand the basic morphology of the samples before moving on to its electronic properties.

A general overview of the studied nanotube samples is shown in Table 4.1. The studied samples have been prepared by pulsed laser evaporation method and therefore the mean diameter ranges between 1.2 nm to 1.4 nm.

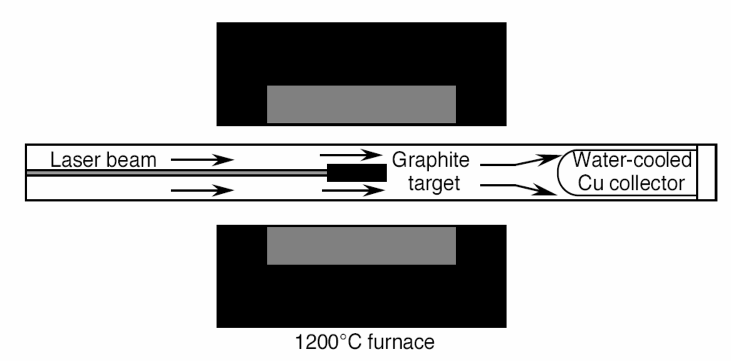

Figure 4.14: *Schematic representation of the pulsed laser vaporization setup used for producing carbon nanotubes [201].*

4.2.1 Synthesis of SWCNTs by laser ablation

In the laser evaporation method, a piece of graphite is vaporized by laser irradiation in helium or argon gas atmosphere [201]. The schematic representation of the laser evaporation apparatus is shown in Figure 4.14. The graphite target is placed in the middle of the furnace and temperature is raised to ≈ 1200°C. The tube is then filled with flowing inert gas. A laser beam focussed onto the surface of the graphite disk, scans the whole surface of the target maintaining a smooth and uniform face of vaporization. During the laser ablation process, the carbon species produced by the vaporization are pushed from the high-temperature zone of the furnace by the flowing inert gas and collected on a water-cooled cold finger. When a small amount of transition metal is added to the graphite target, SWCNTs are produced. A high yield of SWCNTs is obtained when Ni, Co and their mixtures are used. The ends of the produced SWCNTs are closed and the nanotubes are clean with no amorphous carbon layer. However, amorphous carbon particles, fullerenes, graphitic polyhedrons with enclosed metal particles are produced together with SWCNTs. Therefore, the end-product is purified extensively to remove substances other than nanotubes.

4.2.2 Unoriented SWCNT films

As-prepared unoriented nanotube film [202, 203]

- The SWCNTs were made by the laser ablation technique using 1:1 Ni/Co catalyst.

- Raw nanotube soot were ultrasonically dispersed in dimethyl-formamide (DMF) with a concentration of 1 mg/ml and ultracentrifuged at 20000g for 10 min.

- The supernatant liquid was decanted and solid was redispersed in DMF solution.

- After several cycles of centrifugation, the residual solid SWCNT material was

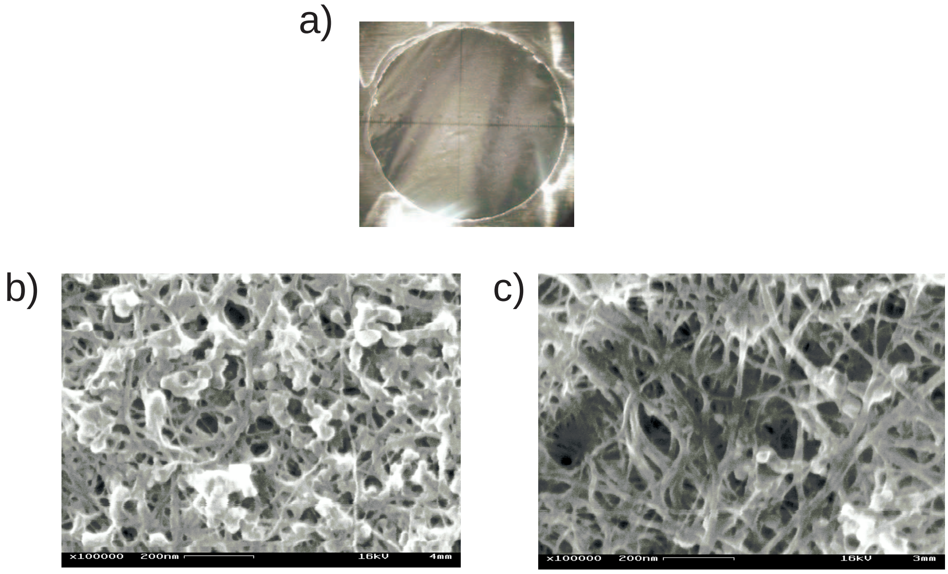

Figure 4.15: *a) Optical image of unoriented carbon nanotube film; b) Scanning tunneling microscopic (SEM) pictures of as-prepared unoriented carbon nanotube film; c) SEM pictures of purified unoriented carbon nanotube film*

suspended in water contained 0.2 wt% of Triton X-100 surfactant.

- In order to prepare as-prepared unoriented nanotube film, the suspension was diluted with DMF to obtain a concentration of 6-18 μg/ml.
- Approximately 50 ml of this dilute suspension was vacuum filtrated using 0.2 μm pore size membrane filters composed of regenerated cellulose.
- After filtration, the nanotube films were repeatedly washed with several ml of water or acetone in vacuum.
- The washed nanotube films were then transferred to vacuum chamber and evacuated to a final pressure 10^{-3} mbar at room temperature for 30 min.
- The films were finally removed from the filter by adhesive tape selectively applied to the top surface.
- The free-standing films were affixed to metal frame and further dried in high vacuum (10^{-6} mbar) at room temperature.

Purified unoriented nanotube film [202, 203]

- The raw nanotube soot was refluxed with 2-3 M HNO_3 for 48 h, after which the whole reaction mixture was centrifuged at 20000g.
- The remaining acid solution was removed by decanting.
- The solid residue was then re-suspended in water containing the surfactant Triton X-100. The concentration of SWCNTs was $\approx$ 0.3 mg/ml.
- To remove the small particles, this suspension was run over/through (and flushed with additional Triton X-100 solution) a ultrafiltration cell using 0.2 μm pore sized membrane filters.
- To make thin films, the SWCNT suspension was diluted in dimethyl formamide (DMF) solution such that the concentration of SWCNTs was about 6-18 μg/ml.
- The suspension was subsequently filter deposited on 0.2 μm pore sized membrane filters made of regenerated cellulose, vacuum dried and removed from filter using adhesive tape.
- The purified film was later annealed at 1200°C in vacuum.

The unoriented carbon nanotube films have an average thickness of about 200 nm and a diameter of about 15 mm. The average density of the nanotubes in these films were found to be 1.2 ± 0.1 gcm^{-3} [202]. The optical image (naked-eye view) of the unoriented nanotube film is shown in Figure 4.15. The scanning electron microscopic (SEM) images of the as-prepared and purified unoriented films, shown in Figure 4.15(b), illustrate the morphological differences between the two studied samples. It can be seen that the as-prepared film has cluster-like particles (catalyst impurities) while purified film is more clean. Although there is a difference in the amount of particles other than nanotubes in the two films, the volume fraction of the nanotubes in both films appears to be the same. From the SEM images, a rough estimation of the bundle diameters in both films could be made. The as-prepared and the purified films have bundle diameters in the range 60-250 Å and 120-400 Å, respectively. The larger bundle diameters observed in the SEM images of the purified film is similar to that observed by Martinez *et al.* [204]. The larger bundle size was suggested to be the result of re-bundling of purified and annealed carbon nanotubes. Thus, both the as-prepared and the purified SWCNTs should have small structural defects with purified film containing smaller amounts of non-carbonaceous impurities.

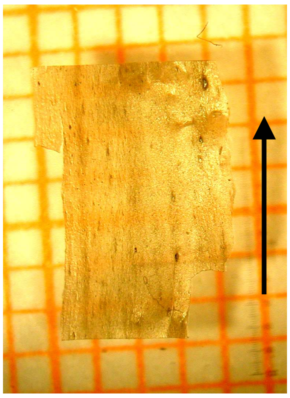

Figure 4.16: *Optical image of oriented nanotubes embedded in poylethylene matrix. The black arrow in the figure indicates the orientation of the nanotube axis in the matrix.*

4.2.3 Oriented SWCNTs in polyethylene matrix

Purification of SWCNTs [205]

The SWCNTs synthesized by laser evaporation, were purified as follows:

- Carbon soot containing SWCNTs was refluxed at 100 °C in an aqueous solution of H_2O_2 for 3 h.
- After removal of any amorphous carbon, the samples were treated with HCl overnight to eliminate the remaining catalytic metals (the metal contents were decreased to less than 3 wt%).
- Small particles of by-products in the H_2O_2 purification and amorphous carbons which covered the surface of the SWCNTs, were then removed by ultrasonication in NaOH (pH$= 10 - 11$) for 2 h.

Preparation of oriented SWCNT/polymer composite [206]

The picture of oriented nanotubes embedded in polyethylene matrix is shown in Figure 4.16. The direction of the orientation of the nanotube axis is indicated by the arrow.

- For the preparation of investigated 0.5 wt% of SWCNT/polyethylene composite, the SWCNTs were mixed with toulene and sonicated for 3 h for dispersion.
- The dispersed nanotubes were blended with polyethylene/toulene mixture at 160 °C and stirred till the toulene solvent evaporated.
- The heated composite was mechanically stretched and instantly cooled.

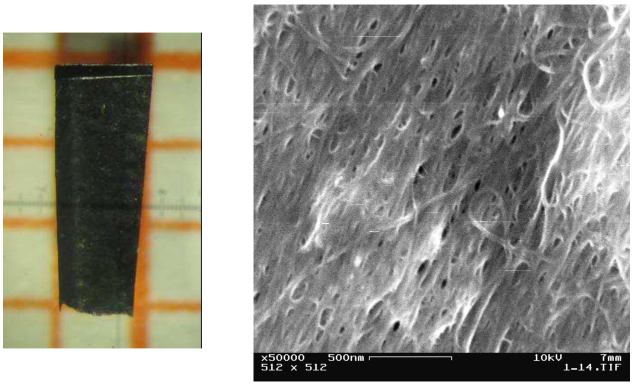

Figure 4.17: *Optical image (left) and SEM image (right) of the magnetically-aligned free-standing single-walled carbon nanotube film.*

- The drawing rate of the mechanical stretching was about 10-20, and the film thickness was about 10-30 μm.

4.2.4 Magnetically-aligned SWCNT film

The alignment of nanotubes using magnetic field is based on the fact that the metallic tubes are paramagnetic in nature and therefore should align themselves parallel to the direction of the magnetic field. The other nanotubes, that are diamagnetic and negative susceptibilities perpendicular to tube axis, align along the field vector. Macroscopic aligned membranes could be produced successfully using high magnetic field [207, 208].

- SWCNTs were prepared by laser ablation at 1100°C.
- SWCNTs were purified by acid treatment (mainly HNO_3) and sonicated after suspending in Triton X100 solution.
- The nanotubes were filter deposited from the dilute suspension on to a porous membrane arranged parallel to the strong magnetic field (about 7 or 25 T).
- A sonicated suspension of 20-40 mg/ml purified SWCNTs was flowed through the filters under a constant pressure of 20 psi.
- The robust thick films were removed from the filter membranes, pressed between Teflon disks for drying and annealed in vacuum at 1150°C using a slow ramp to drive off volatile substances and enhance crystallinity.
- The obtained films have a thickness of about 10 μm.

The image of the magnetically-aligned nanotube film investigated in this work and its SEM image is shown in Figure 4.17. About 70% of the tubes are oriented in the same direction. An estimation of various bundle diameter from the SEM image gives a value of 150-280 Å.

4.2.5 Effect of purification on carbon nanotubes

In addition to the preparation method, the post-synthesis chemical processes also affect the properties of the carbon nanotubes films. A large number of studies have been performed to understand the effects of various purification methods available. The purified nanotubes used in this study have been subjected to nitric acid treatment, and subsequent centrifugation and sonication processes. Although nitric acid reflux is a commonly used method to purify nanotubes, this acid treatment is known to digest not only the impurities but also the nanotubes [209, 210] (For example, the unoriented nanotube films used in our studies was treated for 48h in HNO_3 acid reflux [202]).

Due to the high reactivity of the nanotube caps and defect locations in the side walls, the nitric acid causes opening of the nanotube tips and loose ends in the side walls [211, 212]. The other chemicals, like DMF, used during the processing also have large effect on the nanotubes by opening tube tips and damaging side walls [211]. Furthermore, the processing steps like sonication breaks the tubes producing open tubes of shorter lengths. The annealing instead helps the removal of the carboxylic and other functional groups attached to the destroyed sidewalls and open tips during the chemical processes [213].

As all the nanotube samples used within this investigation have been purified and/or subjected to sonication with solvent, they are expected to be fragmented with more structural defects than the as-grown nanotubes, and also have shorter lengths.

As the chemically-treated nanotubes have open ends, the adsorption of argon which is used as pressure transmitting medium, are important and can not be ignored. Adsorption of argon occurs at interstitial channels between the adjacent tubes, grooves and surface sites at the outer surface of the bundle, and the adsorption sites inside the empty nanotubes [214]. As the nanotube films have not been subjected to the degassing procedure, it is not possible to estimate the amount of adsorbed argon which is even otherwise a difficult task.

4.3 Results and analysis: Ambient pressure studies

In this section, the infrared spectra of the studied SWCNT films at ambient pressure is presented. The analyses employed to extract the information related to the properties of the SWCNT films are also described in detail.

4.3.1 Unoriented SWCNT films

The two types of unoriented SWCNT films, namely, the as-prepared and the purified unoriented SWCNT films (see Section 4.2.2), were investigated in a wide frequency range (6-22000 cm^{-1}) at ambient pressure.

The transmittance and the absorbance spectra of the purified and the as-prepared films at ambient conditions are shown in Figure 4.18. The spectra can be separated into two main energy regions: the Region I dominated by a strong FIR absorption and the Region II with the excitonic optical transitions which have been previously assigned to the interband transitions across vHS in the DOS (see Section 4.1.3 for detailed information). The Region II (highlighted as a shaded area in Figure 4.18) consists of the optical transitions corresponding to both semiconducting and metallic nanotubes. The labels S_{11}, S_{22}, M_{11} and $S_{33/44}$ refer to the optical transitions of semiconducting (S) or metallic (M) tubes, with the subscripts according to the increasing energy of the involved electronic states (see inset of Figure 4.18). The Region II also contains a strong absorption in the background of the optical transitions. This absorption corresponds to the π-plasmon at 5 eV due to the collective excitations of π electrons in the graphene sheet [151, 215].

The low-energy spectra of the carbon nanotubes films are dominated by a strong absorption (see Region I in Figure 4.18(b)). In principle, the transmittance spectrum of a carbon nanotube film can be described by two different models:

(i) Drude-Lorentz (DL) model (see Section 2.2.2) which describes both the excitations due to itinerant charge carriers, and the excitations of the localized carriers and the interband transitions: The dielectric function of a nanotube film according to the Drude-Lorentz model is then given by the Eqn.(2.10). Within this model, the carbon nanotube film is considered as being dense enough to obtain the optical conductivity spectrum by applying the simple DL model to describe the transmittance spectrum of the carbon nanotube film. Thus, the transmittance of unoriented SWCNT film could be fitted using the coherent transmission function according to the DL model.

(ii) Maxwell-Garnett effective medium approximation (EMA model) (see Section 2.2.3) combined with the DL model for finite metallic particles embedded in a dielectric

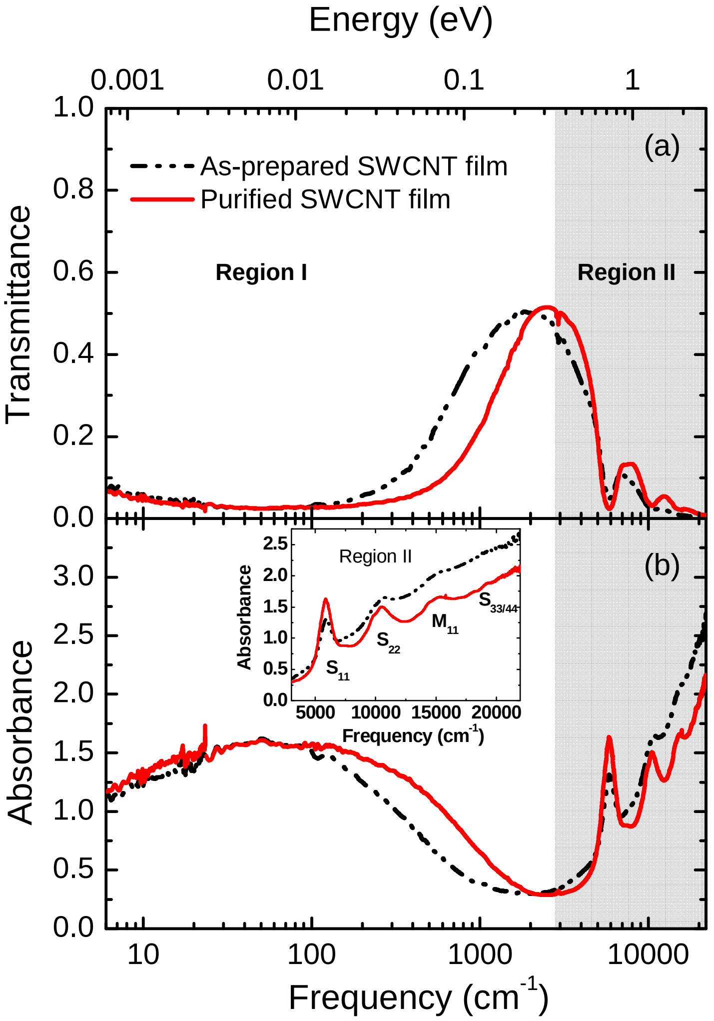

Figure 4.18: *(a) Transmittance and (b) absorbance spectra of the as-prepared and the purified unoriented SWCNT film at ambient conditions. Region I is the frequency range of low-energy excitations while Region II (shaded area) corresponds to the frequency range in which the other optical transitions lie. Inset shows the various contributions of semiconducting (marked as S) and metallic (marked as M) tubes in the Region II.*

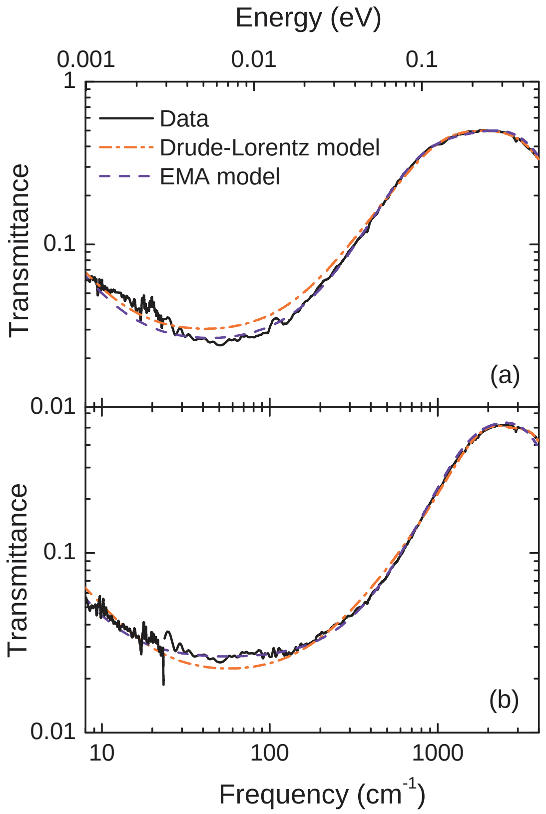

Figure 4.19: *Room-temperature transmittance spectra in Region I (see Figure 4.18 for definition) of (a) the as-prepared and (b) the purified SWCNT film together with the fits according to the Drude-Lorentz model and the effective medium approximation (EMA) model.*

medium [5]: Hereby, the nanotubes are considered to be metallic wires of finite length embedded in a dielectric host medium [198, 206]. The effective dielectric function of the carbon nanotube film is given by the expression

$$\epsilon_{eff} = \epsilon_i \frac{g + v(1-g)\epsilon_{NTs} + (1-g)(1-v)\epsilon_i}{g(1-v)\epsilon_{NTs} + (v \cdot g + 1 - g)\epsilon_i}, \tag{4.18}$$

where ϵ_i is the dielectric function of the insulating dielectric host (air in our case) and ϵ_{NTs} is the dielectric function of carbon nanotubes in the film, described by the DL model (Eqn.(2.10)). g is the geometrical factor which determines the shape of the particles embedded in the medium, and is equal to zero for an infinitely long needle. Therefore, as the particles are nanotubes, g tends to zero but not exactly zero. v is the volume fraction of the nanotubes in the dielectric medium ($v = 1 - x$ according to the Eqn.(2.17) in Section 2.2.3 where x is the volume fraction of the dielectric medium). According to the Marwell-Garnett effective medium approximation (EMA), the Drude peak due to the itinerant carriers is not centered at $\omega = 0$ but a finite frequency. Within this picture, the peak position should rather depend on the geometrical factor of the material in the dielectric medium than the carrier density [216].

The fits of the transmittance spectra of both SWCNT films using the two described models and the so-obtained optical conductivity spectra are shown in Figure 4.19 and

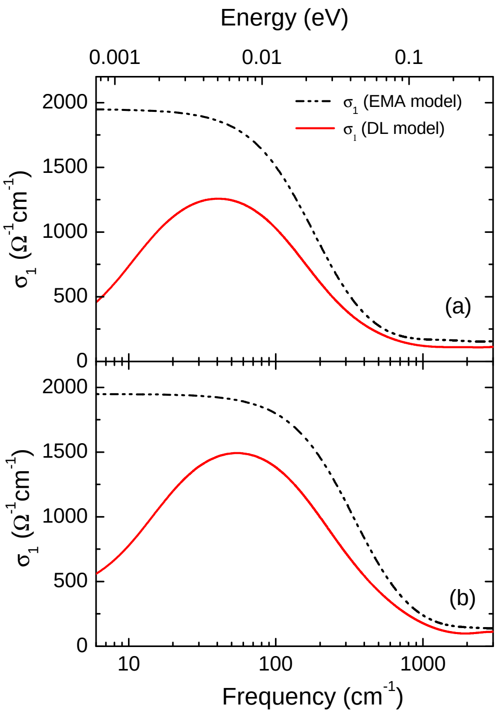

Figure 4.20: *Low-frequency optical conductivity of (a) the as-prepared and (b) the purified SWCNT film at ambient conditions obtained from the fit of the transmittance spectra using the DL model and the EMA model (see text for definitions).*

Figure 4.20, respectively. The two models give rise to optical conductivities that are significantly different. The optical conductivity obtained from the DL model decreases with decreasing frequency below 50 cm^{-1}, while optical conductivity obtained from EMA model increases continuously with decreasing frequency (see Figure 4.20).

Within the DL model, the FIR transmittance spectrum can be described by two components: a Drude contribution due to free-carriers in the metallic tubes and a band described by a Lorentzian term below 100 cm^{-1}. This gives rise to a maximum in the FIR optical conductivity, and the most of the spectral weight in the optical conductivity lies in the band (see Figure 4.20). The goodness of the fit can be illustrated using difference curves, i.e., by checking the difference between the measured spectrum and fit curve. Such difference curves for both models are shown in Figure 4.21 for both as-prepared and purified unoriented SWCNT films. It is obvious that the difference between the measured spectrum and fit curve obtained from the EMA model is much less than the difference obtained from the DL model fit. In addition, the uncertainty in the fitting parameters of the Drude and the Lorentzian terms is large even though a reasonable fit of the transmittance spectra could be obtained using this simple DL model.

Several experimental works which applied the DL model have attributed the origin of the non-metallic FIR contribution, namely the band centered below 100 cm^{-1}, to the gaps in the small-gap nanotubes and the curvature-induced gap in the quasi-metallic

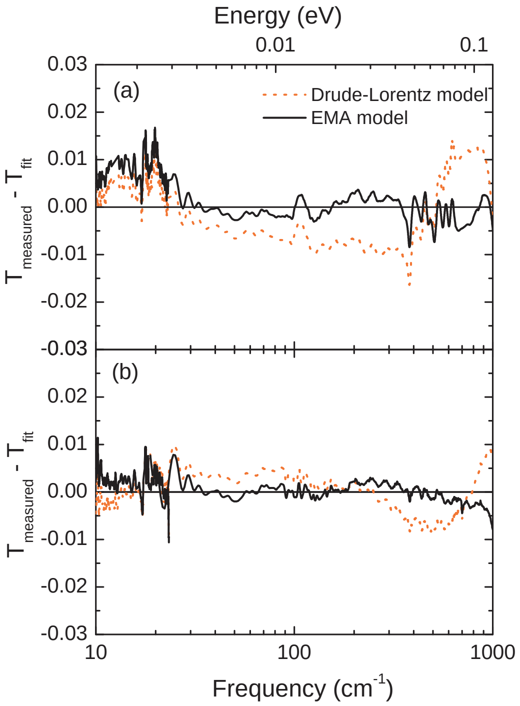

Figure 4.21: *Difference curves illustrating the deviation of the fit curve for both DL and EMA models from the measured transmittance spectrum of both (a) the as-prepared and (b) the purified SWCNT film at ambient conditions.*

nanotubes [160, 164, 168, 199]. However, an alternative explanation for the origin of this FIR peak, i.e., a conduction resonance due to finite size effect, was proposed based on the hole-doping studies [206]. According to this interpretation, the EMA model should best describe the low-frequency optical conductivity in the SWCNT films. Indeed, the fit using the EMA model is significantly better than that of the DL model (see Figure 4.19). The best fit of the EMA model was obtained for the values $g = 2.5 \times 10^{-4}$ and $v = 0.7$. The values of v, usually estimated based on the SEM images, lie in the expected range of 0.6-0.9 and the value of g is much smaller than 1 as expected for the nanotube bundles [198, 206]. Hereby, it was sufficient to use only a Drude term to describe the low energy optical response.

In contrast, some THz spectroscopic investigations use both the Drude term and the Lorentzian term, to describe low energy properties of SWCNT films within the EMA model [217, 218]. Jeon *et al.* related the Lorentzian term to phonon absorption, while Altan *et al.* suggested that the Lorentzian contribution arises from photoinduced localized carriers [217, 218]. The fitting, here in this study, required the use of only a Drude term and implies that the optical conductivity obtained using the EMA model is more likely due to the metallic charge carriers. The metallic charge carriers may be localized along the finite length of the nanotubes due to several factors like simple finite length effect, disorder and defects in the carbon nanotubes. As the EMA model describes the observed optical properties more reliably (see Figure 4.21), the EMA

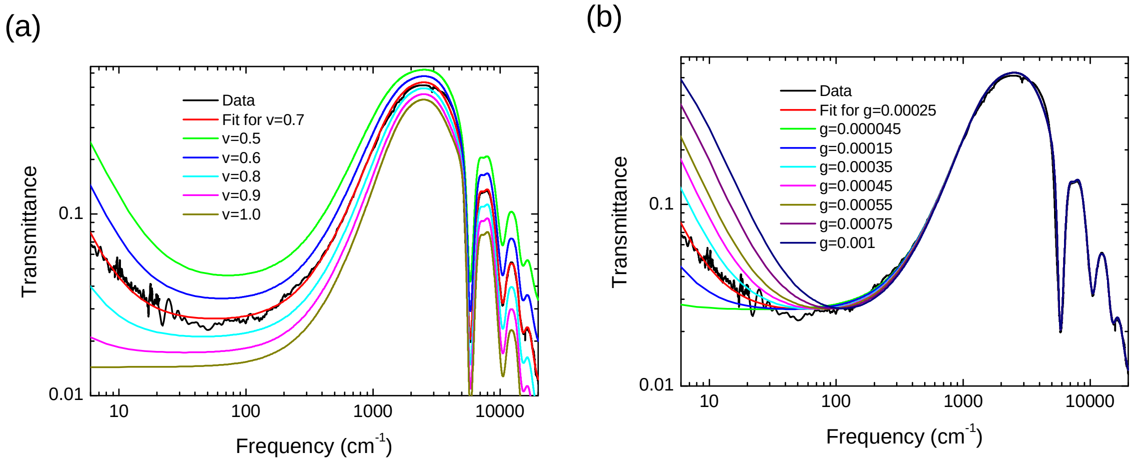

Figure 4.22: *(a) Variation of the fit of the ambient-pressure transmittance spectrum of the purified unoriented SWCNT film according to the EMA model with respect to change in depolarization factor (g). (b) Variation of the fit of the ambient-pressure transmittance spectrum of the purified unoriented SWCNT film according to the EMA model with respect to change in volume fraction (v).*

model is applied for the following FIR analyses presented in this project.

A quantitative analysis of the higher-energy side (Region II in Figure 4.18) of the transmittance spectra was also performed. This can be achieved using a simpler analysis without the EMA approximation. Figure 4.22 illustrates the effect of the parameters of the EMA model on the transmittance spectrum of the purified unoriented SWCNT film. As the depolarization factor is varied, the higher-energy region of the transmittance spectrum remains unaffected. The change in volume fraction obviously behaves similar to the change in the thickness of the sample, i.e., only the absolute value of

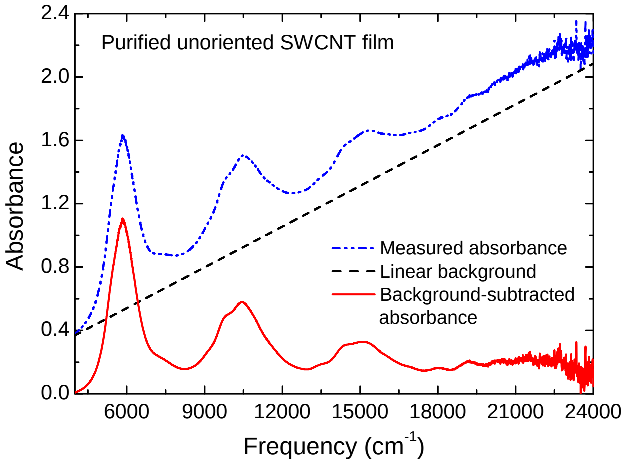

Figure 4.23: *Illustration of the background subtraction procedure. The measured and the background-subtracted absorbance spectra of the purified unoriented SWCNT film at ambient conditions are shown together with the linear background.*

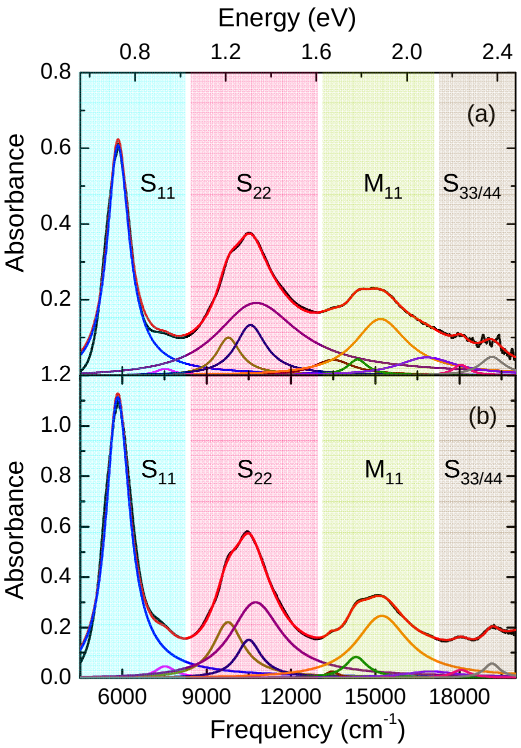

Figure 4.24: *Background-subtracted absorbance spectra of (a) the as-prepared and (b) the purified SWCNT film at ambient conditions, in the near-infrared and visible frequency ranges. The typical energy regimes of the optical transitions in the semiconducting (marked as S) and metallic (marked as M) tubes are represented by shaded areas of different colors.*

transmittance varies and not the energy of the optical transitions. For this reason, the energies of the optical transitions in the high-energy spectra of the various investigated SWCNT films are extracted without employing the EMA model in the forthcoming analysis of the Region II of the infrared spectra in all studied SWCNT films.

The energy of the optical transitions can be extracted in the following way: The background contribution in the MIR-visible absorbance spectra, corresponding to the π-plasmon absorption, can be considered nearly linear in the measured energy range [200, 219]. This linear background is subtracted from the measured spectra in order to obtain purely the absorptions due to optical transitions. Figure 4.23 illustrates the background subtraction procedure with the absorbance spectra of the purified carbon nanotube film at ambient conditions. The so-obtained background subtracted spectra were then fitted using Lorentz model to obtain the energy of the optical transitions. Figure 4.24 shows the background-subtracted absorbance spectra of the as-prepared and the purified films at ambient conditions together with the fitting curve and its components. The various contributions for the principle transitions observed in the absorbance spectra correspond to the various contributions from the nanotube bundles with different diameter and chirality distributions.

The temperature-dependent absorbance spectra of both the as-prepared SWCNT film and the purified SWCNT film are shown in Figure 4.25. It can be observed that the absorbance of both films are very similar and nearly temperature independent in

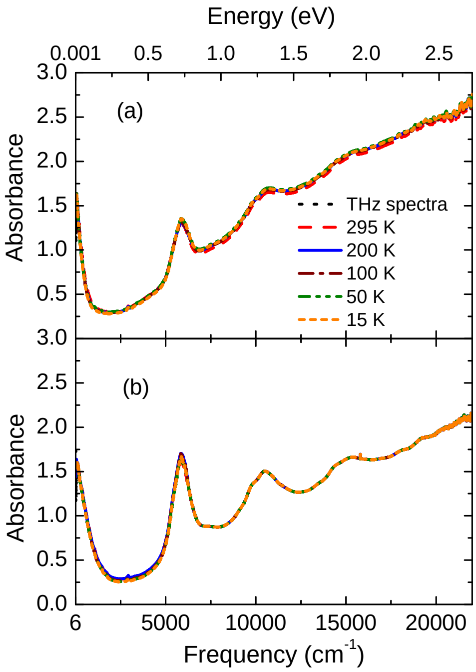

Figure 4.25: *Absorbance spectra of (a) the as-prepared and (b) the purified SWCNT film as a function of temperature between 15 K and 295 K over a broad frequency range (6-22000 cm^{-1}).*

the frequency range from 30 cm^{-1} to 22000 cm^{-1}. Even in the earlier temperature-dependent infrared spectroscopic measurements on unoriented SWCNTs an extremely weak non-metallic temperature dependence was observed in the temperature range from 8 K to 298 K [160, 161]. A more recent temperature-dependent studies on carbon nanotube networks by Borondics *et al.*, also revealed weak changes with respect to temperature in the FIR spectral regime [164]. Thus, the finding of a negligible temperature dependence of the studied as-prepared and purified SWCNT films is in qualitative agreement with earlier investigations.

4.3.2 Oriented SWCNTs in polyethylene matrix

The polarization-dependent transmittance measurements were performed on the SWCNT film which consists of oriented SWCNTs embedded in polyethylene matrix (see Section 4.2.3 for details on the sample) over the frequency range 100-20000 cm^{-1} at ambient pressure.

The transmittance and absorbance spectra of the nanotubes-polymer matrix is shown in Figure 4.26. The optical response of the nanotubes-polymer matrix is highly anisotropic for the polarization of the incident light parallel and perpendicular to the alignment direction of majority of the nanotubes in both Region I and Region II. The polarization of light incident parallel and perpendicular to the alignment direction will be referred as $\mathbf{E}\|$alignment direction and $\mathbf{E}\perp$alignment direction, respectively. For $\mathbf{E}\|$alignment direction, the low-energy excitation in the Region I which corresponds

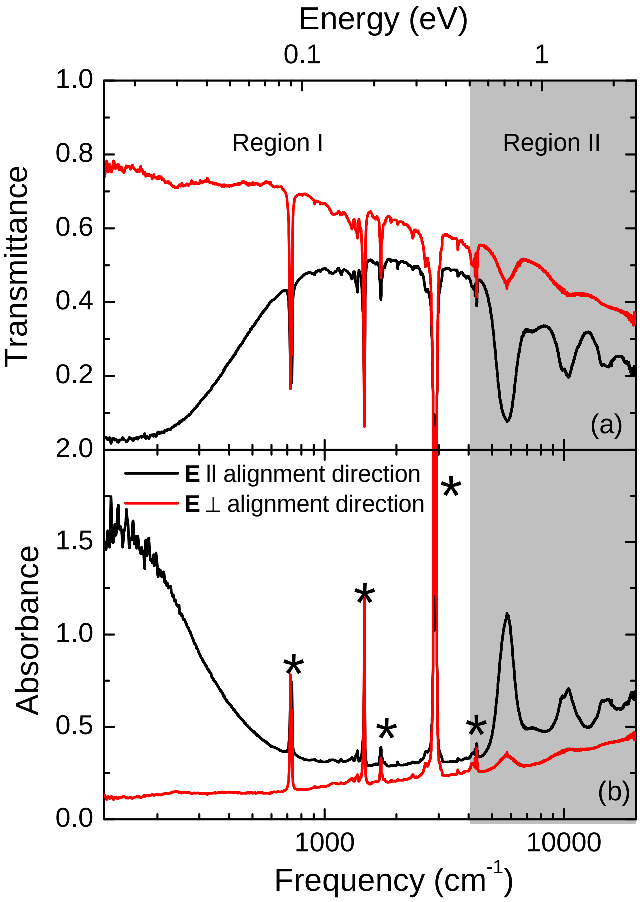

Figure 4.26: *(a) Transmittance and (b) absorbance spectra of the oriented nanotubes embedded in polyethylene matrix at room temperature for both polarizations* **E**$\|$ *alignment direction and* **E**$\perp$ *alignment direction. The vibrational modes corresponding to polyethylene (host medium) are marked by asterisks (*). Region I is the frequency range of low-energy excitations while Region II (shaded area) corresponds to the frequency range in which the other optical transitions lie.*

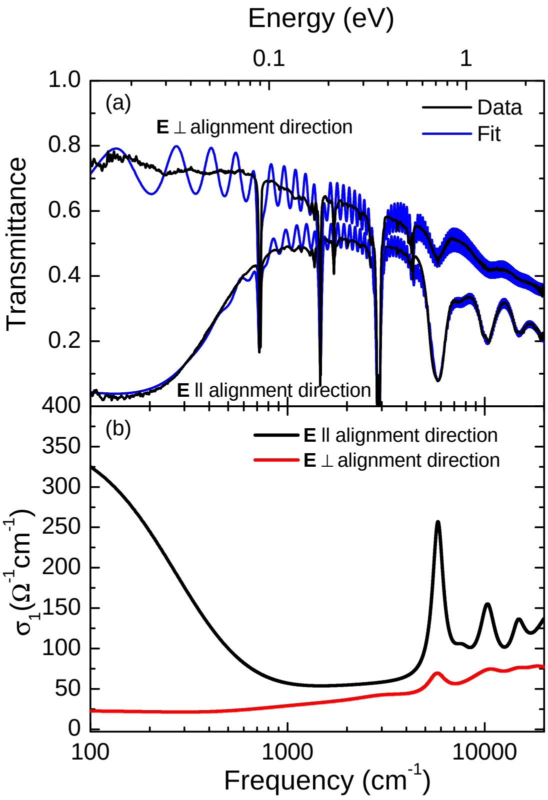

Figure 4.27: *(a) Room-temperature transmittance spectra of the oriented nanotubes in the polyethylene matrix for both* **E**$||$*alignment direction and* **E**$\perp$*alignment direction and the fits according to the EMA model. (b) Optical conductivity obtained from the fit of the transmittance spectra with EMA model (see text for definition).*

to the metallic-response, and the optical transitions in the Region II are very pronounced with large intensities whereas for **E**$\perp$alignment direction the excitations in both regions are strongly suppressed. This is in agreement with the selection rules (see Section 4.1.3). The extremely weak intensity transitions in Region II of the spectra for **E**$\perp$alignment direction are due to the contributions from 10% of the unoriented tubes present in the matrix and the unpolarized light "leakage" from the non-perfect polarizer.

The transmittance spectra of the nanotubes-polymer matrix for both polarizations were described by the EMA model using the coherent transmission function. The transmittance spectra together with the fit and the resulting optical conductivity are shown in Figure 4.27. The best fit of the EMA model for the whole spectrum was obtained for the depolarization factor of $g = 3 \times 10^{-3}$. The volume fraction (v) and the thickness were set to 0.05 (5 wt% concentration of nanotubes) and 22 μm (for the best fit for the whole spectrum), respectively. For **E**$\perp$alignment direction, the optical conductivity is very low with a non-metallic behavior. For **E**$||$alignment direction, the optical conductivity exhibits a metallic behavior at low frequencies and consists of strong optical transitions corresponding to the semiconducting and metallic tubes at higher energies.

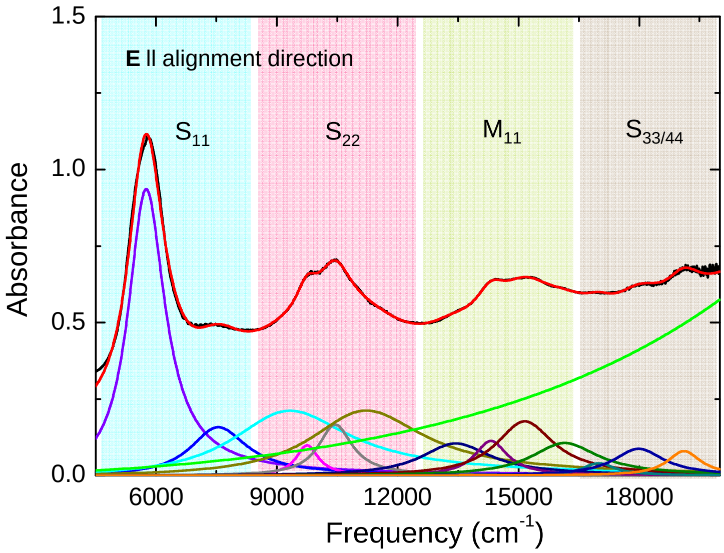

Figure 4.28: *Absorbance spectrum of the oriented nanotubes embedded in the polyethylene matrix for* **E**||*alignment direction in the Region II together with the Lorentz function fit and the fit components. The typical energy regimes of the optical transitions in the semiconducting (marked as S) and metallic (marked as M) tubes are represented by shaded areas of different colors.*

The energy of the optical transitions in the absorbance spectrum for **E**||alignment direction were obtained by fitting with Lorentz functions. The absorbance spectra of the nanotubes-polymer matrix consists of nonlinear background due to the contributions from the π-plasmon absorption at 5 eV as well as the high-energy excitations in the polyethylene host medium. Therefore, the linear background subtraction procedure which was used for the absorbance spectra of the unoriented SWCNT films, is not employed here. Figure 4.28 shows the absorbance spectrum together with the fit and its components. Similar to the absorbance spectra of the unoriented carbon nanotube films, the fine structure is due to various contributions from the nanotubes of different diameters and chirality.

4.3.3 Magnetically-aligned SWCNT film

The polarization-dependent reflectance measurements were performed on the magnetically-aligned SWCNT film (see Section 4.2.4 for detailed information on this film) over the frequency range 100-20000 cm^{-1} at ambient pressure.

Figure 4.29 shows the polarization-dependent reflectance spectra of magnetically-aligned SWCNT film at ambient conditions. As expected according to the selection rules (see Section 4.1.3), the reflectance spectrum for **E**||alignment direction exhibits metallic behavior with higher reflectivity in the Region I compared to the spectrum for **E**⊥alignment direction, and the optical transitions in the Region II are more pro-

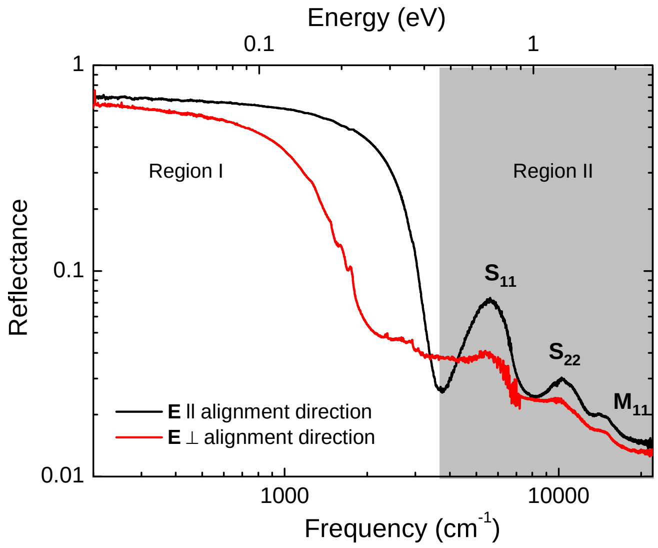

Figure 4.29: *Reflectance of magnetically-aligned SWCNT film for both* **E**$\|$*alignment direction and* **E**$\perp$*alignment direction at ambient conditions. Region I is the frequency range of low-energy excitations while Region II (shaded area) corresponds to the frequency range in which the other optical transitions lie.*

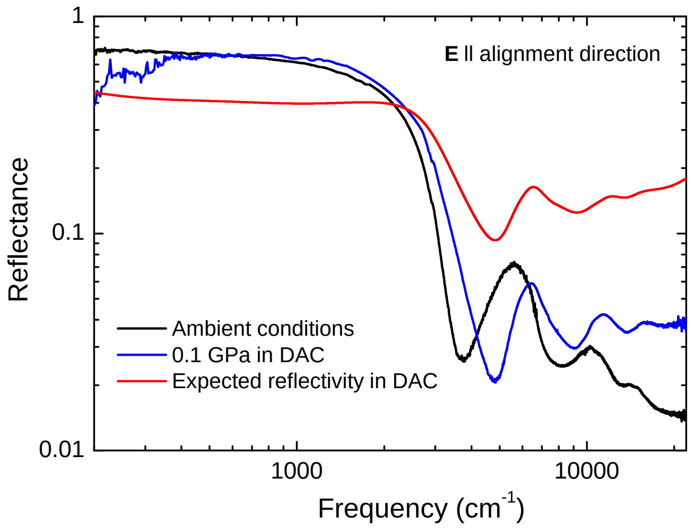

Figure 4.30: *Comparison of the reflectance spectrum for* **E**$\|$*alignment direction at ambient pressure with that at lowest measured pressure of 0.1 GPa and the simulated reflectance spectrum expected in the DAC.*

nounced for the polarization **E**||alignment direction. For **E**⊥alignment direction, although the reflectivity is low in both regions, the reflectivity qualitatively resembles the reflectivity for the **E**||alignment direction. This is due to the fact the 30% randomly-oriented nanotubes in the film contribute to the optical transitions observed for the **E**⊥alignment direction based on the selection rules. Please note that the polarization leakage due to non-perfect polarizer also contribute to the reflectivity for the **E**⊥alignment direction.

The reflectivity measured on the free-standing sample resulted to be too low due to the film's surface quality. This can be clearly understood when the expected reflectivity in DAC (can be calculated from the reflectivity of the free-standing sample), is compared with the reflectivity spectrum measured at 0.1 GPa. The latter shows higher reflectivity in the low-frequency region and a more pronounced drop of the reflectivity at the plasma edge (see Figure 4.30) than the simulated reflectivity. It is likely that the quality of the surface of the SWCNT film is significantly improved in the DAC, since the top surface of the SWCNT film is pressed on to the surface of the diamond anvil. For this reason, the reflectance measured at ambient pressure can not be quantitatively compared to the high-pressure reflectance data. Nevertheless, the metallic behavior at the low-energy region and the optical transitions in the Region II range are well-defined. Therefore, the energy of the optical transitions could be estimated by a fit of the Region II of the reflectance spectrum with Lorentz functions.

4.4 Results and analysis: High pressure studies

In this section, the results and analyses of the pressure-dependent infrared studies on the SWCNT films are presented.

4.4.1 Unoriented SWCNT films

The pressure-dependent transmission measurements were performed for pressures up to 8 GPa using argon as pressure transmitting medium over the frequency range 150-20000 cm^{-1}.

The as-prepared and the purified SWCNT films show considerable changes in the electronic properties with the application of pressure in both Regions I and II. Figure 4.31 and Figure 4.32 show the transmittance and absorbance spectra of the as-prepared and the purified unoriented SWCNT films for selected pressures up to 8 GPa in the FIR-visible frequency range. With increasing pressure, the optical transitions in the Region II shift to lower frequencies and also exhibit a significant broadening.

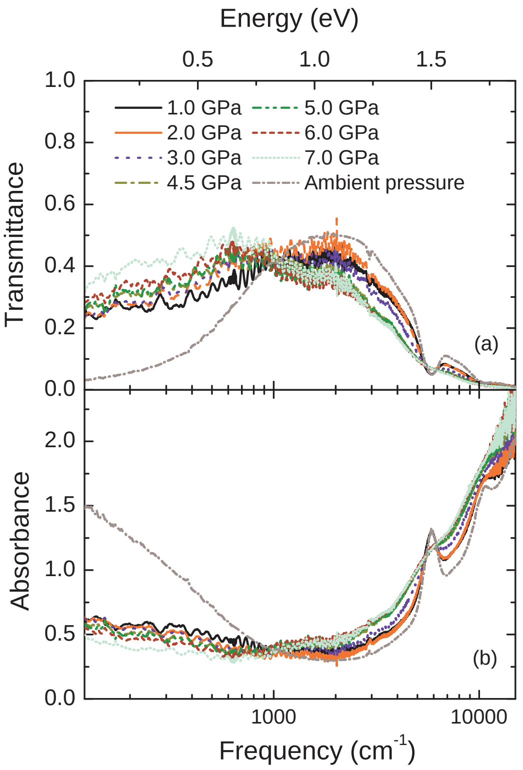

Figure 4.31: *(a) Transmittance and (b) absorbance spectra of the as-prepared SWCNT film for selected pressures up to 7 GPa over a broad frequency range (120-15000* cm^{-1}*).*

The intensity of the low-energy absorption (<1000 cm^{-1}) decreases with increasing pressure.

The low-energy absorbance spectra of the carbon nanotubes were found to be significantly affected by the application of pressure (see Figure 4.31 and Figure 4.32). In Figure 4.31 and Figure 4.32, the ambient pressure spectra measured on the free-standing samples are also presented. The absorbance of the SWCNT films at the lowest measured pressure (1 GPa) is significantly lower compared to that at the ambient pressure, with the effect being more drastic for the as-prepared SWCNT film.

Above 1 GPa, the absorbance of the SWCNT films in the FIR frequency region decreases continuously with increasing pressure. For the quantitative analysis of the pressure-induced changes in the low-energy infrared response of the carbon nanotubes, the transmittance spectra were fit with the EMA model using the coherent transmission function as described in Section 4.3. The parameters of the EMA model, namely, the geometrical factor and the volume fraction, were assumed as being constant with respect to pressure, in order to minimize the uncertainties in the analysis. This is also physically reasonable as these parameters can not be changed with the application of external pressure. Similar to the ambient-pressure spectra, the low-frequency part of the spectra can be described by one Drude contribution. Figure 4.33 shows the so-obtained optical conductivity spectra of the as-prepared and the purified SWCNT

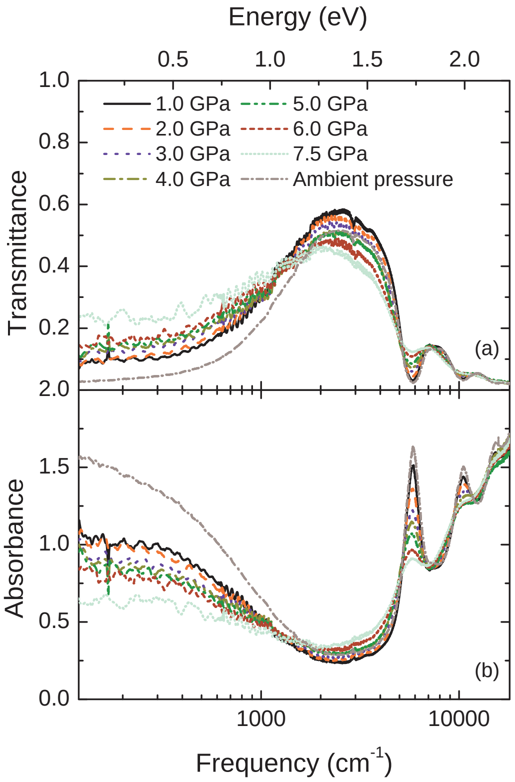

Figure 4.32: *(a) Transmittance and (b) absorbance spectra of the purified SWCNT film for selected pressures up to 7.5 GPa over a broad frequency range (120-20000 cm^{-1}).*

films for various pressures up to 7.5 GPa. The low-frequency optical conductivity decreases with increasing pressure, in good qualitative agreement with the absorbance spectra. The dc conductivity σ_{dc} and the plasma frequency ω_p of the Drude term obtained from the fitting, decrease with increasing pressure (see Figure 4.34). The pressure dependence of both SWCNT films are in qualitative agreement, although the metallic term of the purified film is better defined.

For quantitative analysis of the pressure-induced changes in the optical transitions their energies were extracted from the absorbance spectra for all measured pressures using the same procedure as for the absorbance spectra at ambient conditions (background subtraction and fitting with Lorentzian functions, see Section 4.3). For illustration, the background-subtracted absorbance spectra of the as-prepared and the purified SWCNT films for the lowest measured pressure are shown in Figure 4.35 together with the fitting curve and its components. It is obvious that the fine structure in the optical absorption bands observed in the spectrum at ambient pressure (see Figure 4.24) is obscured even at low pressures due to pressure-induced broadening effects. For the same reason, only the strong and most obvious transitions have been considered for the fitting using Lorentzian functions, and excellent fits were obtained.

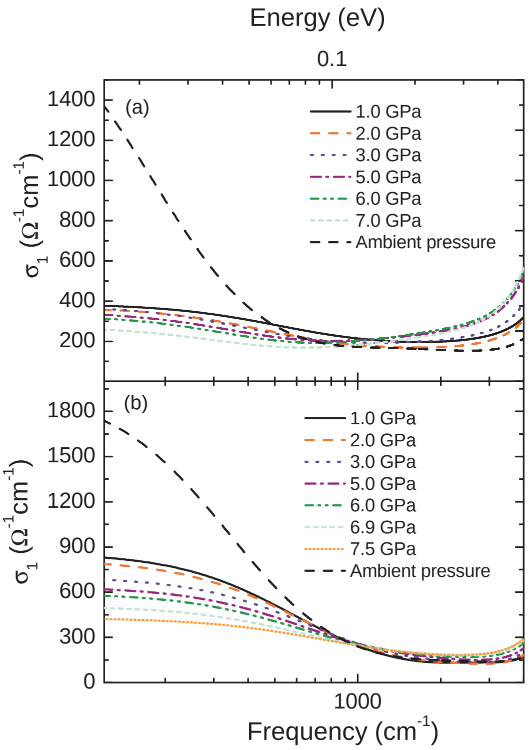

Figure 4.33: *Pressure-dependent optical conductivity spectra of (a) the as-prepared and (b) the purified SWCNT film below 3000* cm^{-1}*, obtained from the fit of transmittance spectra using the EMA model (see text for definition). The optical conductivity of both SWCNT films decrease monotonically with increasing pressure.*

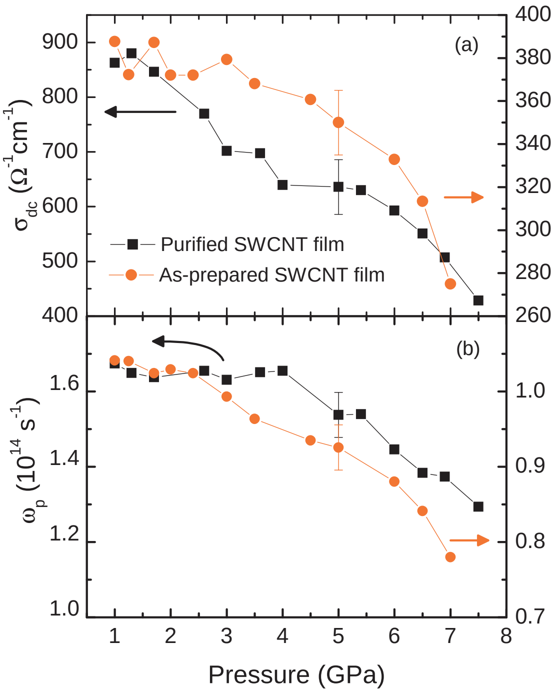

Figure 4.34: *Pressure dependence of (a) the dc conductivity* σ_{dc} *and (b) the plasma frequency* ω_p *of the Drude term in the FIR optical conductivity of both unoriented SWCNT films obtained from the fit using the EMA model (see text for definition).*

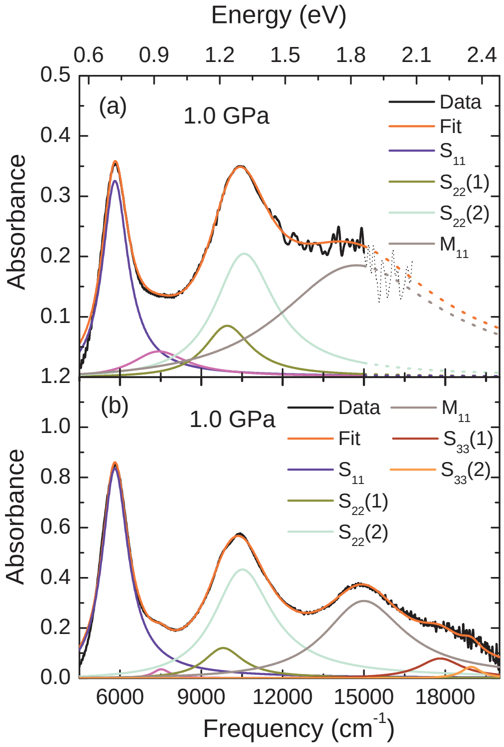

Figure 4.35: *Background-subtracted absorbance spectra of (a) the as-prepared and (b) the purified SWCNT film at lowest pressure together with the fit of the optical transitions using Lorentzian oscillators. Only the strong transitions are considered and labeled.*

4.4.2 Oriented SWCNTs in polyethylene matrix

The polarization-dependent investigations on the oriented nanotubes embedded in the polyethylene matrix were performed in the FIR-visible frequency range (150-22000 cm^{-1}) at pressure up to 8 GPa. The pressure-dependent transmission measurements were performed using argon as pressure transmitting medium.

Figure 4.36 shows the pressure-dependent transmittance and absorbance spectra of the nanotubes-polymer matrix for both polarizations. Interestingly, the Region I of the spectra shows very little changes with the application of pressure for both **E**$\|$alignment direction and **E**$\perp$alignment direction. However, the optical transitions in the Region II of the absorbance spectra for **E**$\|$alignment direction do exhibit a pressure dependence similar to those of the unoriented SWCNT films. The optical transitions shift to lower energies with increasing pressure together with broadening and loss of intensity. In the absorbance spectra for **E**$\perp$alignment direction, very small changes are observed in the weak contributions from the unoriented tubes.

Since the low-energy spectra hardly change with increasing pressure, the low-energy optical conductivity at high pressure can be considered the same as that at the ambient pressure.

In order to determine the energy of the optical transitions as a function of pressure, a fit of the Region II of the absorbance spectra was done using Lorentz functions sim-

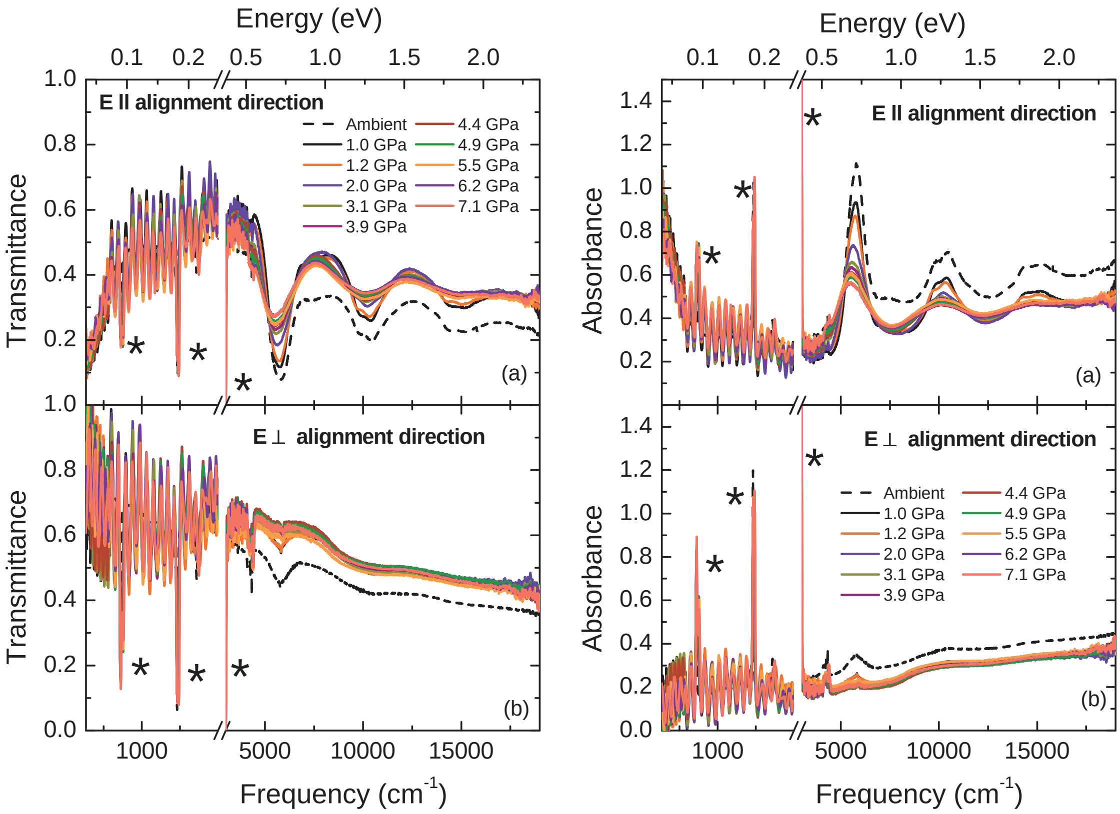

Figure 4.36: *(a) Transmittance and (b) Absorbance spectra of the oriented nanotubes embedded in the polyethylene matrix for both* **E**$\|$*alignment direction and* **E**$\perp$*alignment direction, for pressures up to 7.5 GPa. The interference fringes superimposed on the spectra are due to multiple internal reflections between the diamonds in the DAC. The vibrational modes corresponding to polyethylene (host medium) are marked by asterisks (*).*

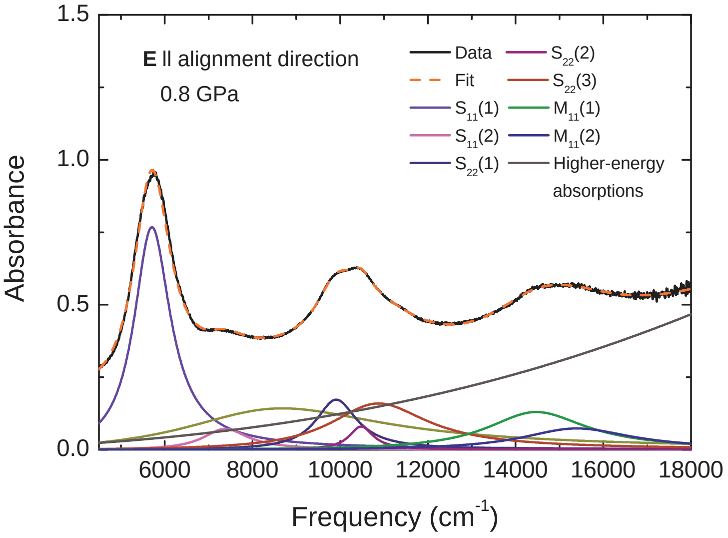

Figure 4.37: *Absorbance spectrum of the oriented nanotubes embedded in the polyethylene matrix for* **E**$\|$*alignment direction in the Region II together with the Lorentz function fit and the fit components for the lowest measured pressure of 0.8 GPa.*

ilar to the ambient-pressure absorbance spectrum. Figure 4.37 shows the absorbance spectra for **E**||alignment direction at the lowest pressure together with the fit and its components. As the absorbance spectra for **E**⊥alignment direction consist of low intensity absorption bands due to the 10% randomly-oriented nanotubes, no fits were performed for these spectra.

4.4.3 Magnetically-aligned SWCNT film

The polarization-dependent investigations on the magnetically-aligned SWCNT film were performed in the FIR-visible frequency range (150-22000 cm^{-1}) at pressures up to 8 GPa. The pressure-dependent reflection measurements were performed using CsI as pressure transmitting medium.

The pressure-dependent reflection measurements were performed as described in Section 2.3.4 to obtain the reflectivity of the magnetically-aligned nanotube film with respect to diamond as a function of pressure. Figure 4.38 shows the reflectivity (R_{s-d}) of the nanotube film in the FIR-visible frequency range for pressures up to 5 GPa, for both **E**||alignment direction and **E**⊥alignment direction. The reflectivity around 2000 cm^{-1} is dominated by the multiphonon absorption of the diamond anvils (see Section 2.3.4 for more details) and therefore is not shown. The optical transitions in the Region II of the absorbance spectra shift to lower energies with increasing pressure in consistence with the pressure-dependence of the optical transitions of other studied SWCNT films. They exhibit slight broadening and loss of intensity similar to the pressure-dependence of the optical transitions in the nanotubes-polymer matrix. The reflectance in the Region I of the absorbance spectra decreases slightly with increasing pressure.

The reflectance spectra of the magnetically-aligned SWCNT film for both polarizations were fit with the EMA model to obtain the optical conductivity. The best fit of the EMA model was obtained for the depolarization factor of $g = 0.01$. The volume fraction (v) and the thickness were taken as 0.7 and 10 μm, respectively. The FIR reflectance is described by a Drude term in agreement with that of the pressure-dependent transmission data on other SWCNT films. The so-obtained optical conductivity (below 3000 cm^{-1}) for both polarizations is shown in Figure 4.39. The dc conductivity (σ_{dc}) and the plasma frequency (ω_p) of the Drude term decrease with increasing pressure (see Figure 4.40) similar to the optical conductivity of the unoriented carbon nanotube films.

The pressure dependence of the optical transitions for the **E**||alignment direction was extracted using the procedure similar to the one employed in other SWCNT films (fit of the reflectance spectra with Lorentz functions). It is important to note that linear

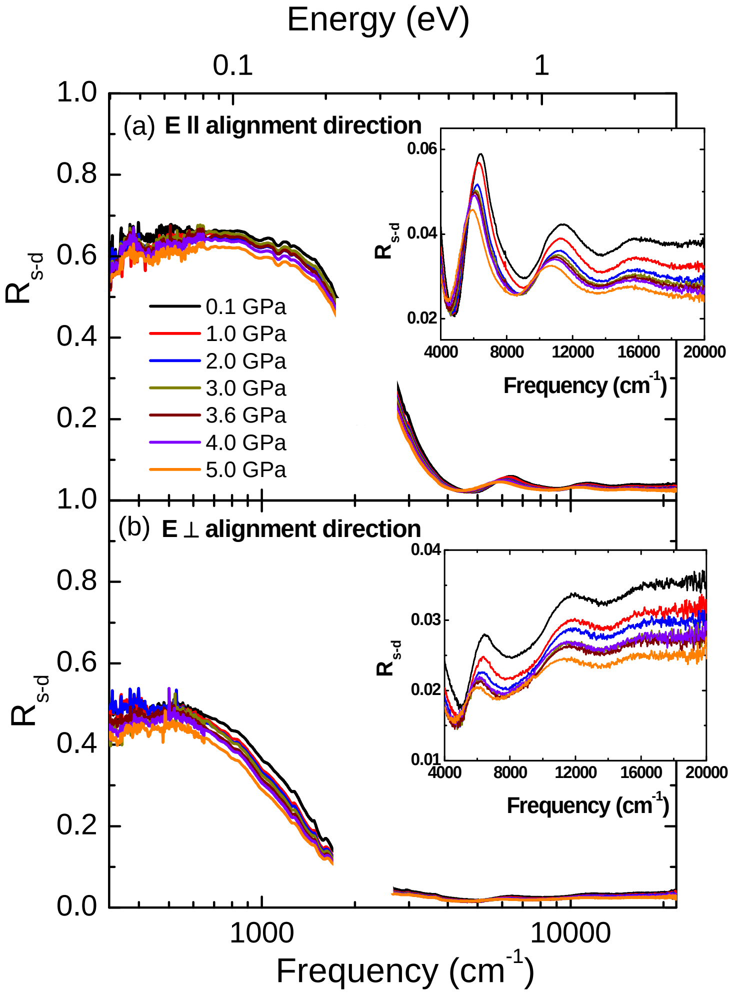

Figure 4.38: *Reflectance (R_{s-d}) with respect to diamond of the magnetically-aligned SWCNT film for both* $\mathbf{E}||$*alignment direction and* $\mathbf{E}\perp$*alignment direction, for pressures up to 5 GPa. Insets show the pressure-dependence of the reflectivity spectra in the Region II which consists of the optical transitions. The data around 2000 cm*$^{-1}$ *is unreliable due to the dominant contribution from the multiphonon absorption of the diamond anvils (see Section 2.3.4 for more details) and therefore not shown here.*

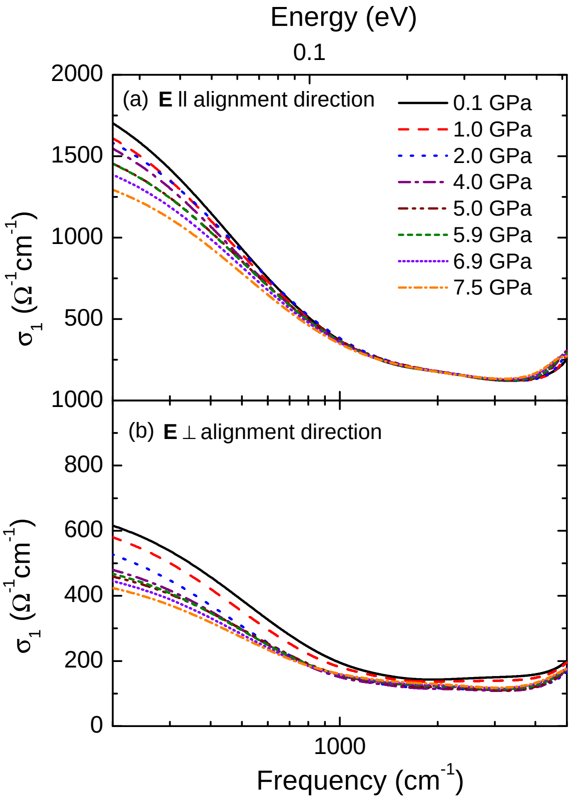

Figure 4.39: *Pressure-dependent optical conductivity spectra for (a)* $\mathbf{E}\|$*alignment direction and (b)* $\mathbf{E}\perp$*alignment direction obtained from the fit of the reflectance spectra using the EMA model (see text for definition).*

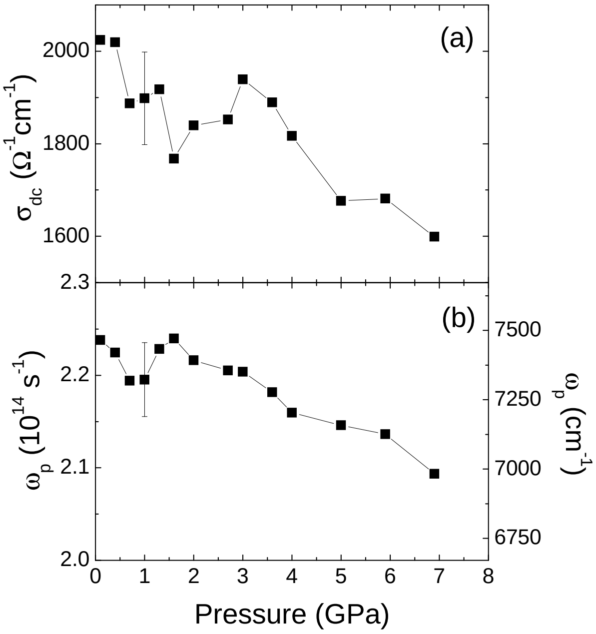

Figure 4.40: *Pressure dependence of (a) dc conductivity* σ_{dc} *and (b) plasma frequency* ω_p *of the Drude term in the FIR optical conductivity of the magnetically-aligned SWCNT film for* $\mathbf{E}\|$*alignment direction, obtained from the fit using the EMA model (see text for definition).*

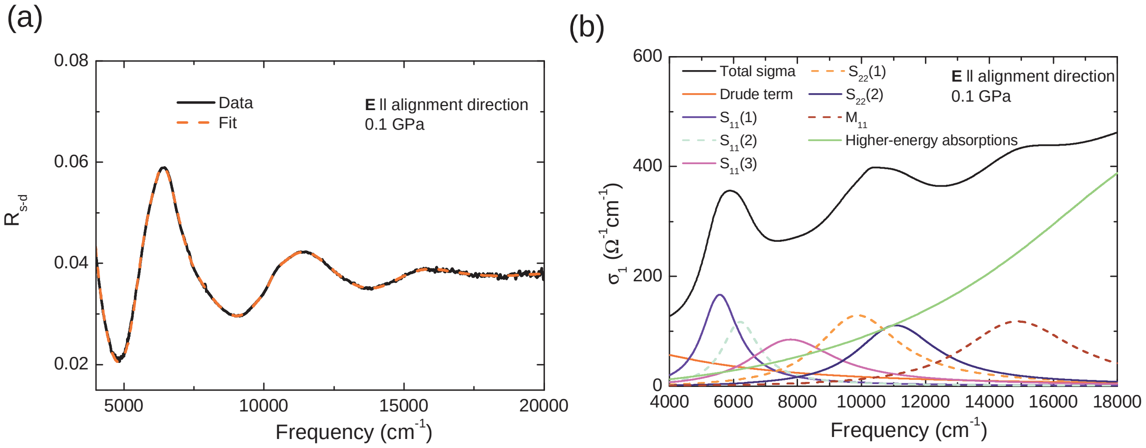

Figure 4.41: *(a) Reflectance spectrum of the magnetically-aligned SWCNT film for* **E**||*alignment direction at 0.1 GPa together with the fit using Lorentz functions. (b) Optical conductivity of the magnetically-aligned SWCNT film for* **E**||*alignment direction at 0.1 GPa obtained from the Lorentz function fit and the fit components.*

background subtraction can not be employed in the reflectivity spectra, and therefore background contribution due to π-plasmon absorption is described using a Lorentzian at around 35000 cm^{-1}. The fit of the lowest pressure reflectance spectra and the resulting optical conductivity and the fit components for **E**||alignment direction are shown in Figure 4.41. The corresponding analysis for **E**$\perp$alignment direction could not be performed reliably due to the presence of strong background in the reflectivity. Moreover, the optical transitions are broader than for **E**||alignment direction and have suppressed intensity giving rise to very large errors in the estimation of the maximum of the bands using Lorentz function fits. Therefore, only the optical transitions obtained for **E**||alignment direction will be considered for rest of the discussion.

Table 4.2: *List of the parameters obtained from the Drude fit of the ambient pressure spectra according to the EMA model for the investigated SWCNT films. As the ambient-pressure reflectivity spectrum of the magnetically-aligned film can not be used for quantitative analysis (see Section 4.3.3), the fit results for the reflectivity spectrum at 0.1 GPa has been used. For the nanotubes-polymer matrix and the magnetically-aligned film, the results only for* $\mathbf{E}\|$*alignment direction are considered.*

Parameter	As-prepared film	Purified film	Nanotubes-polymer matrix	Magnetically-aligned film
σ_{dc}	1949 Ω^{-1}cm^{-1}	1949 Ω^{-1}cm^{-1}	366 Ω^{-1}cm^{-1}	2024 Ω^{-1}cm^{-1}
ω_p	4639 cm^{-1} (139 THz)	6345 cm^{-1} (190 THz)	2480 cm^{-1} (74 THz)	7469 cm^{-1} (224 THz)
Γ	184 cm^{-1} (5.52 THz)	344 cm^{-1} (10.31 THz)	280 cm^{-1} (8.39 THz)	459 cm^{-1} (13.76 THz)

4.5 Discussion

In this section, the implications of the results described in the previous sections are discussed in detail. The comparison of the electronic properties of the studied films at ambient pressure is presented in the first subsection. The subsequent subsections explain the phenomena induced by extreme conditions.

4.5.1 Comparison of studied films at ambient pressure

It is worth understanding the similarities and differences in the electronic properties of the unoriented and oriented SWCNT films investigated within this project, before analyzing the electronic properties at extreme conditions.

In order to compare the low-energy conductivity of the investigated SWCNT films, the parameters of the Drude term obtained from the fit of the measured transmittance/reflectance with the EMA model are tabulated in Table 4.2. Although the plasma frequencies of the unoriented SWCNT films are comparable with one of the earlier works [160], the varied values of plasma frequency and scattering rate reported in different experimental investigations make the quantitative comparison rather difficult. It can be immediately noticed that the dc conductivity of the nanotubes-polymer matrix even for the polarization $\mathbf{E}\|$alignment direction is much lower than the other three films. This observation is reasonable as the nanotubes-polymer matrix consists

Table 4.3: *Energies of the optical transitions of the investigated SWCNT films, obtained from the fit of ambient-pressure absorbance/reflectance spectra.*

ν (cm^{-1}) Label	As-prepared film	Purified film	Nanotubes-polymer matrix	magnetically-aligned film
S_{11}	5843	5834	5756	5454
	7516	7516	7546	6206
				7780
S_{22}			9329	
	9771	9759	9752	9579
	10560	10500	10448	10242
	10764	10742	11222	11449
M_{11}	13500	13438	13443	
	14372	14319	14317	14463
	15190	15235	15157	
	16834	16982	16147	
			16993	
$S_{33/44}$	18053	18053	17986	17394
	19157	19157	19111	

of only a small fraction (5 wt%) of the SWCNTs in the insulating polyethylene matrix. The scattering rate of the SWCNT films also exhibits differences. The as-prepared film has a lower scattering rate than the other SWCNT films. This result is intriguing because one would naively expect the as-prepared SWCNT film with more carbonaceous impurities to have larger scattering rate. The higher scattering rate of the purified film suggests an influence of the purification process. The purified SWCNT film subject to acid treatment could have more side-wall defects than the as-prepared SWCNT film which leads to increase in the scattering rate of the carriers. The plasma frequency, which is a measure of the number of free carriers (see Eqn.(2.11)), is lower for the nanotubes-polymer matrix and the as-prepared unoriented SWCNT film than for the purified unoriented SWCNT film and the magnetically-aligned film. Therefore, the as-prepared unoriented SWCNT film and the nanotubes-polymer matrix seem to have more localized carriers. Thus, a close look at the differences in the Drude conductivity of the investigated SWCNT films suggest that the film morphology plays an extremely important role in determining the electronic properties of the SWCNT film.

Since the investigated SWCNT films have the same average diameter, it is also interesting to compare the optical transitions of these films at ambient pressure. The optical transitions obtained from the fit using Lorentz functions for the investigated films are tabulated in Table 4.3. The energies of the optical transitions of the unoriented nanotube films and the nanotubes-polymer matrix agree reasonably well. The fine structure in the optical transition bands due to the presence of nanotubes of different diameters and chiralities is obscured and less obvious in the magnetically-aligned nanotube film. Although the diameter distribution in the magnetically-aligned film and in the other studied SWCNT films are similar, the energies of the optical transitions in semiconducting tubes present in magnetically-aligned film appears to be lower than those in the unoriented SWCNT film and the nanotubes-polymer matrix. This intriguing result could imply that the excitonic effects and/or intertube interactions (see Section 4.1.2 for effect of nanotube bundling on the vHS) are more significant in case of the oriented SWCNT film than the unoriented SWCNT films.

4.5.2 Localization of the carriers

The FIR conductivity of the unoriented SWCNT films exhibits little temperature dependence (see Figure 4.25). The complex dielectric constant measurements by Hilt *et al.* [162] indicate that the transport properties of the SWCNT mats can be well described by a Drude model with a negligible temperature dependence. They observed that the conductivity at very low frequencies (around 285 GHz) was dominated by localized carriers. Temperature-dependent measurements on the unoriented carbon nanotubes including the nanotubes embedded in the polymer matrix, have suggested that there is localization of carriers in the bundles as well as along the tubes [162, 165, 166]. The theoretical studies have also found that localization of carriers plays a major role in determining the low-energy properties of the carbon nanotubes [167, 220]. An alternative explanation for very weak temperature dependence of the FIR conductivity was offered by Kampfrath *et al.* very recently [168]. The weak temperature dependence was attributed to the tube-to-tube variation of the chemical potential in the measured SWCNT film [168]. In addition to the temperature-dependent investigations on the low-energy optical absorption, the pressure-dependent low-energy optical studies should serve as an important tool in understanding the electronic properties of the unoriented SWCNT films, especially the FIR conductivity in SWCNT films.

The low-energy optical conductivity of the studied SWCNT films exhibits a qualitatively different pressure dependence. The low-energy absorbance of the nanotubes-polymer matrix exhibits nearly no change with application of pressure (see Figure 4.36) while those of unoriented films (see Figure 4.31 and Figure 4.32) and the magnetically-

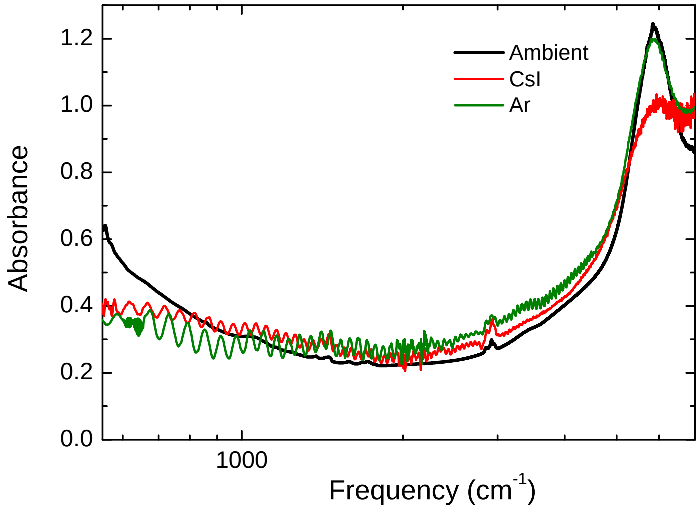

Figure 4.42: *Comparison of MIR absorbance spectrum of As-prepared SWCNT film at ambient pressure with the absorbance spectra at 1.0 GPa using argon and CsI as pressure transmitting medium.*

aligned film (see Figure 4.38) decreases with increasing pressure. Apparently, the nano-tubes-polymer matrix exhibits a different behavior under pressure compared to the other films but reasons for this behavior are still unclear.

Due to the structural changes in the nanotubes, the electronic band structure of the nanotubes is expected to change considerably under pressure. The deformation of the nanotubes induces symmetry breaking and σ^*-π^* hybridization effects due to the mixing of states. The interaction between the facing layers in the radially-deformed nanotubes further modifies the low-energy electronic structure strongly in the deformed tubes [183, 184, 186]. These changes eventually lead to the opening or closing of the gap at the Fermi level and thereby causing a metal-insulator/semiconductor transition or vice-versa in metallic tubes or small-gap nanotubes, respectively [182–188]. Such a transformation should lead to large changes in the low-frequency spectra. The Drude conductivity of both the as-prepared and the purified SWCNT films appears to be suppressed even at the lowest measured pressure of ≈0.7 GPa (see Figure 4.31 and Figure 4.32). This effect is more pronounced in the case of the as-prepared film compared to the purified film. The FIR absorption in the nanotubes-polymer matrix at the lowest measured pressure is consistent with that at the ambient pressure. Due to the reason explained in Section 4.3.3, the comparison of the optical conductivity of the magnetically-aligned SWCNT film at ambient and lowest-measured pressures was not possible.

In order to verify whether the suppression of the FIR is due to the pressure transmitting medium, the absorbance spectrum of the as-prepared SWCNT film at 1.0 GPa obtained using argon as pressure transmitting medium with that using CsI medium can be compared (see Figure 4.42). The absorbance spectrum obtained using CsI as pressure transmitting medium is very similar to that using argon except that the use

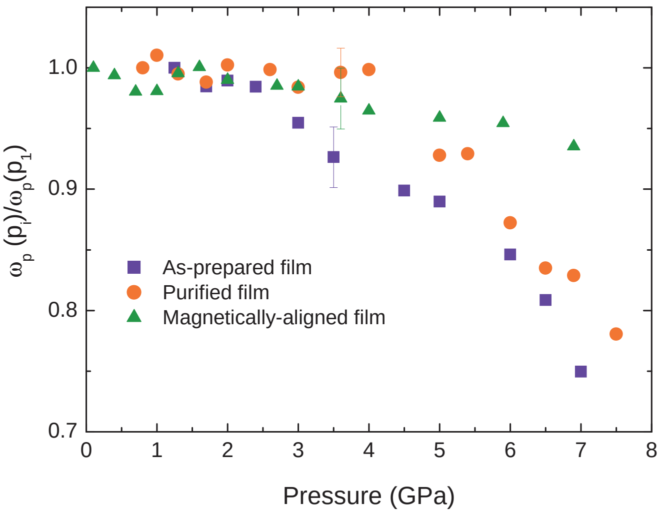

Figure 4.43: *Normalized plasma frequency of Drude term in the FIR optical conductivity of the unoriented SWCNT films and the magnetically-aligned SWCNT film obtained from the fit of transmittance/reflectance spectra using the combined EMA model.*

of CsI broadens the absorption bands and the intensity of the first optical transition is also suppressed. Although, optical conductivity in the FIR obtained using CsI as pressure medium is necessary to quantify the effect of the pressure medium, the qualitative agreement between the absorbance spectra measured using argon and CsI as pressure medium suggests that the suppression of absorption at low-energy is not due to the effect of argon adsorption but most likely an intrinsic property of the unoriented SWCNT film. This effect is probably due to pressure-induced suppression of the optical conductivity in the unoriented SWCNT films. The difference in the pressure dependence of the as-prepared and the purified SWCNT films at the lowest measured pressure further questions the interpretation of the FIR band in terms of pseudogap or gap of small-gap nanotubes as discussed earlier because the intrinsic properties of nanotubes should exhibit the same pressure-dependence at the lowest pressure in both SWCNT films.

The plasma frequency of the Drude term obtained from the fit, is plotted as a function of pressure in Figure 4.43 for the unoriented SWCNT films and the magnetically-aligned SWCNT film. The plasma frequency corresponding to the contributions from the free-carriers, decreases with increasing pressure for the SWCNT films. The pressure-dependence of all three films are comparable in the low pressure range even though there exists significant differences in the optical conductivity of the SWCNT films. At higher pressures (above 3 GPa), the optical conductivity of the magnetically-aligned film shows smaller changes. The decrease in optical conductivity with increasing pressure indicates that there is an increase in the localization effects with increasing pressure. However, this effect seems to be less pronounced in the oriented SWCNT film i.e., the magnetically-aligned film. This could be probably explained by the fact that the magnetically aligned films have less bends, kinks and cross-junctions compared to the “spaghetti-like” unoriented bundles of SWCNTs. Some recent theoretical investigations on the localization effects on deformed nanotubes also suggest that with increasing deformations, the localization length[1] of the carriers decreases leading to a decrease in the conductivity [220, 222]. Therefore, the decreasing low-energy conductivity is tentatively assigned to the increasing localization of carriers caused by defects and deformations induced under high pressure. The localization in case of the unoriented SWCNT film is much more dramatic than that in the magnetically-aligned film. This interesting observation calls for further investigations on the low-energy electronic properties of the carbon nanotubes.

The optical conductivity for $\mathbf{E}\perp$alignment direction in the magnetically-aligned SWCNT film exhibits a similar pressure dependence as that of the optical conductivity for $\mathbf{E}||$alignment direction. This suggests that only the fraction of unoriented SWCNT contribute to the Drude conductivity for perpendicular polarization, and the anisotropy in the optical response of the carbon nanotubes is preserved.

4.5.3 Optical transition energies at extreme conditions

The optical transitions of the carbon nanotubes are affected by pressure and temperature in a very different way. Although the electronic properties of both the as-prepared and the purified SWCNT films show considerable changes with the application of pressure, the two SWCNT films exhibit temperature-independent properties. The temperature-dependent energy shifts of the optical transitions of the SWCNTs observed in the photoluminescence measurement, could either be positive or negative depending on the chiral angle [223]. Recent theoretical studies found that the temperature-dependence of the bandgap of the carbon nanotubes is relatively small compared to the bulk semiconductors, and the maximum temperature-induced shift was calculated to be around 10 meV [170]. In addition to the small temperature-induced changes which are highly chirality dependent, it was suggested that the temperature-dependence of optical transition energies of the nanotubes in the bundles are dominated by the thermal expansion of the nanotubes environment [171]. Very recent experimental and theoretical temperature-dependent studies on the semiconducting nanotubes suggested that the positive or negative energy shifts could be attributed to the external strain while the broadening of

---

[1] Localization length is the distance along the length of the nanotube within which the electronic wave functions are restricted [221].

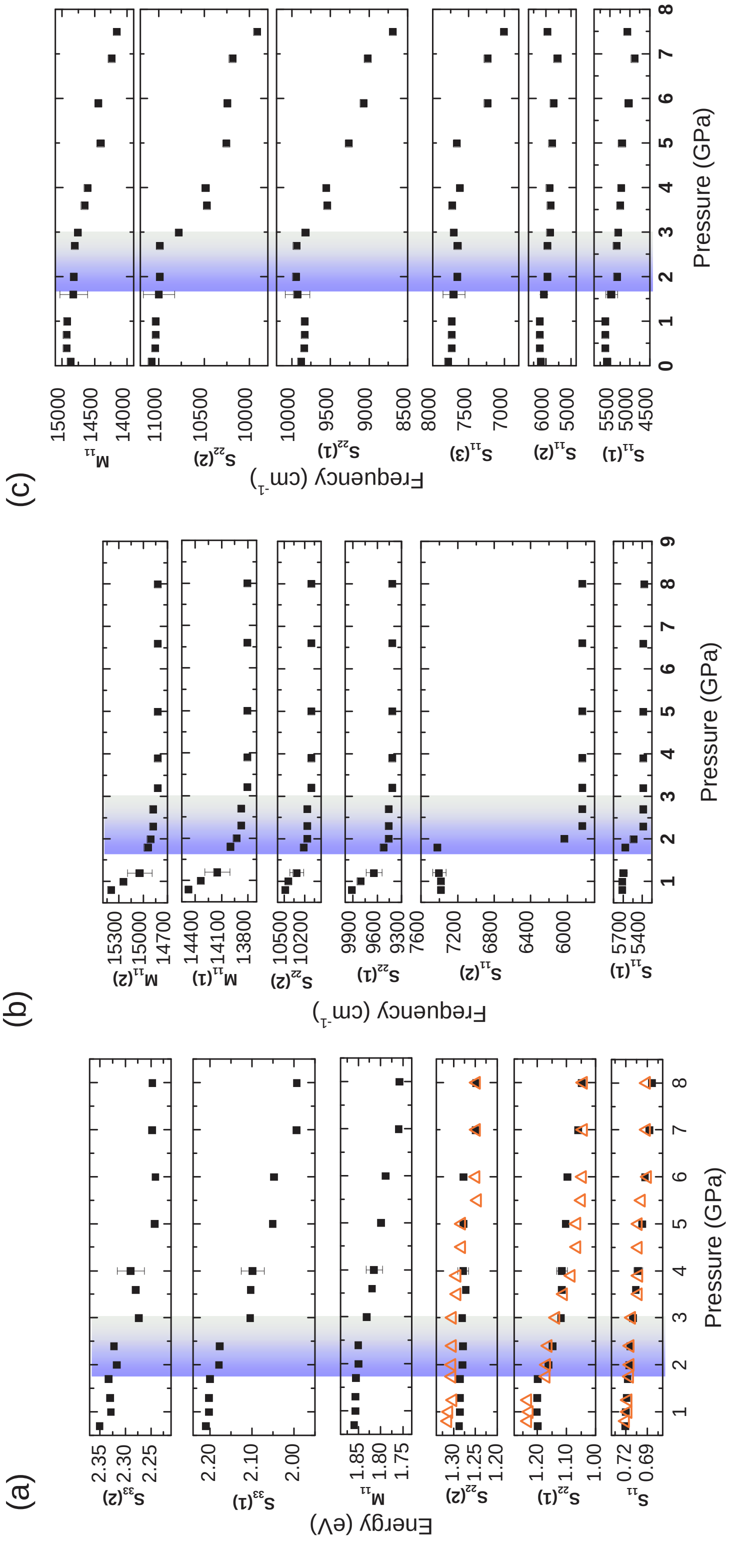

Figure 4.44: *Energies of the strong optical transitions of (a) the unoriented SWCNT films, (b) the oriented nanotubes in polyethylene matrix, and (c) the magnetically-aligned SWCNT film along* **E**‖ *alignment direction as a function of pressures up to 8 GPa. In (a), the pressure dependence of the first two optical transitions of as-prepared nanotube film (red symbols) are also shown together with that of the purified film (black symbols). The shaded area corresponds to the pressure regime in which the anomalies are observed.*

the transitions might be attributed to electron-phonon interactions [224]. The nanotube films studied within this work are free-standing films and therefore can not have effects due to the nanotube environment. The optical transitions of the unoriented and unsegregated nanotube films are generally convolutions of the transitions corresponding to the tubes of different diameters and chiralities. These transitions are therefore quite broad when compared to the small changes expected during the change in temperature. Therefore, the observation of an “averaged-out” temperature response in the nanotube films which give rise to the temperature-independent NIR-visible frequency absorbance spectra is plausible.

The pressure dependence of the optical transitions of the various investigated films can be obtained by plotting the optical transition energies obtained from the Lorentz function fits as a function of pressure. Figure 4.44 shows the pressure dependence of the optical transitions of the investigated SWCNT films as a function of pressure. The higher energy optical transitions in the as-prepared SWCNT film could not be extracted reliably due to very low transmittance of this film. It can be seen that the pressure dependence of the optical transitions in both films have good agreement with each other.

The important observations are as follows:
(i) All optical transitions shift to lower energies with increasing pressure;
(ii) There exists an anomaly at around ≈2.0 GPa in the pressure dependence of the unoriented SWCNT films and the nanotubes-polymer matrix [225]. The anomaly in case of the magnetically-aligned film is observed around 2.7 GPa [226]. The nature of this anomaly will be discussed in Section 4.5.4;
iii) The optical transitions of the unoriented SWCNT films and magnetically-aligned SWCNT film shift to lower energies more drastically for pressures higher than the anomaly while those of the nanotubes-polymer matrix exhibit no pressure dependence.

The changes in the optical transition energies under hydrostatic pressure were theoretically investigated by R.B. Capaz *et al.* [180, 227]. A “family behavior” in the pressure coefficients i.e., having positive or negative pressure coefficients depending on chirality, was observed for semiconducting SWCNTs. Similar behavior was also reported in the study of the band-gap changes under uniaxial stress [184, 228, 229]. However, experimentally an overall shift of the optical transitions to lower energies with increasing pressure has been observed in both bundled and individualized nanotubes [194,230,231]. The shift of the optical transitions to lower energies was generally attributed to the intertube interactions and/or symmetry breaking in the very early high-pressure optical absorption measurements [194]. However, the photoluminescence measurements on the individualized nanotubes in aqueous solution of surfactant showed that the negative pressure coefficient is an intrinsic property of the individual nanotubes and the intertube interactions do not play a role [230]. Furthermore, the effect of σ^*-π^* hybridization in the nanotubes was suggested as the mechanism that causes the overall negative pressure coefficient, at least in the low pressure regime (below 1.3 GPa) [230].

Deacon *et al.* suggested an alternative explanation for the observed downshift of the optical transitions [231]. The interaction of the nanotubes with the surrounding surfactant solution was cited as the reason for the significant changes in the Coulomb interactions. It was suggested that the increasing dielectric constant of the surfactant solution (which is the surrounding medium) could lead to a reduced total Coulomb interaction with the application of pressure. Also, a recent investigation on individual double-walled carbon nanotubes under pressure showed that the interaction of nanotubes with the surrounding medium is very important [232]. The pressure coefficients of the Raman bands were highly dependent on the pressure transmitting medium that was employed [232]. However, the lowering of the energy of the optical transitions has been observed also with the use of solid pressure transmitting medium for which adsorption of the pressure transmitting medium can be ruled out [194, 226]. Apparently, the decrease in energy of the optical transitions with increasing pressure can not be solely attributed to the effect of the surrounding medium and therefore the hybridization effects have to be considered.

The σ^*-π^* hybridization not only plays a significant role in the electronic band-structure of the small diameter tubes [144] but also in polygonized and deformed tubes. The changes in the electronic properties of the SWCNTs with polygonized cross-sections have also been theoretically investigated [182, 227]. According to these studies, the radial deformation of the nanotubes strongly influences the band-structure of the nanotubes, which could eventually be observed in the optical absorption. It was found that the hybridization effects and the symmetry-breaking due to radial pressure lower the conduction-band states towards the Fermi level [182, 227]. The present results, wherein the optical transitions of the SWCNTs shift to lower energies with increasing pressure, could therefore be attributed to the significant hybridization and symmetry-breaking effects arising from the pressure-induced deformation of the nanotubes.

The pressure-dependent investigations within this work have been performed on various nanotubes with different surrounding environments like argon, polyethylene, and CsI. The downshift of the optical transition energies has been observed in all films especially in the low-pressure regime. In the high-pressure regime (>3 GPa), the optical

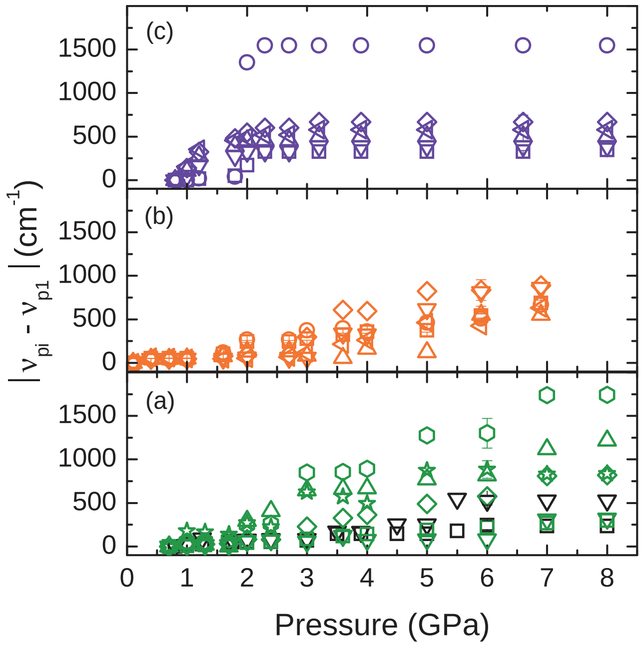

Figure 4.45: *Relative change in the energies of the strong optical transitions of (a) the unoriented SWCNT films, (b) the magnetically-aligned SWCNT film and (c) the nanotubes-polymer matrix with respect to the lowest pressure as a function of pressure. The optical transitions corresponding to both semiconducting and metallic tubes, i.e.,* $S_{11}(1)$ *(square),* $S_{11}(2)$ *(circle),* $S_{22}(1)$ *(up triangle),* $S_{22}(2)$ *(down triangle),* $M_{11}(1)$ *(diamond),* $M_{11}(2)$ *(left triangle),* $S_{33}(1)$ *(hexagon) and* $S_{33}(2)$ *(star), are shown here.*

transitions of the nanotubes in the polymer matrix shows very small changes. This difference is plausibly due to the bundle size and therefore the intertube and interbundle interactions or cross-junctions. The nanotube-polymer matrix should have smaller bundles dispersed in the polyethylene matrix unlike the unoriented SWCNT films and the magnetically-aligned SWCNT film where the SWCNTs form large bundles in contact with each other.

In order to check for further differences in the pressure dependence of the excitonic optical transitions of the SWCNT films, the relative changes in energies of the strong transitions in the unoriented SWCNT films, nanotubes-polymer matrix and the magnetically-aligned SWCNT film were plotted as a function of pressure. Figure 4.45 shows the relative changes of the energy of the optical transitions of the films with respect to the lowest pressure. It can be seen that the pressure-induced changes in the energy of the optical transitions in the investigated nanotube films are comparable for all investigated films. The maximum shift of the optical transitions with the application of pressures up to 7.5 GPa is around 1800 cm^{-1} ($\approx$ 220 meV). According to the pressure-dependent optical absorption studies, Kazaoui et al. suggested that the optical transitions of semiconducting tubes vanish at the pressure of about 4.1 GPa while the transitions corresponding to the metallic tubes persist in the optical absorption spectra [194]. In contrast, the pressure dependence of the optical transitions of both semiconducting and metallic tubes are very similar with comparable pressure-coefficients (see Figure 4.45). The overall red-shift of the optical transitions is in qualitative agreement with the previous pressure-dependent studies on SWCNTs [194,230]. However, the energy-shift of the optical transition with respect to pressure is much smaller than the earlier reports [194, 230]. For example, the shift of the energy of S_{11} transition in the measurements by Kazaoui *et al.* at 4 GPa is nearly twice as much as that observed in the measurements within this project [194]. This discrepancy is probably due to the less hydrostatic conditions that may have been present during the other experiments. The experiments on the unoriented SWCNT film within this project using more hydrostatic pressure medium (argon) could minimize strains due to non-hydrostaticity, reducing the extent of the red-shift and the broadening of the transitions.

4.5.4 Pressure-induced structural phase transition

On applying pressure, the optical transitions in the nanotubes show very small changes up to a certain pressure around 2 GPa in case of the unoriented SWCNT films and the nanotube-polymer matrix, and around 2.7 GPa in case of the magnetically-aligned SWCNT film (see Figure 4.44). Above this pressure, the energy of the optical transitions decreases more drastically with increasing pressure causing an anomaly at these pressures. Several Raman spectroscopic investigations also reported the disappearance or loss of intensity of the RBM of the nanotubes and anomalies in the tangential mode of the nanotubes at pressures around 1.5-2 GPa and were attributed to the deformation of the nanotubes [189].

With the application of pressure, the circular cross-section of nanotubes deforms to stabilize at an oval, elliptical, racetrack-like or peanut-shaped cross-section (see Section 4.1.4). This radial deformation of the SWCNTs is discontinuous and occurs at a certain critical pressure P_c. The value of P_c follows the relation $P_c \propto 1/d^3$. For nanotubes grown by laser ablation technique, with an average diameter of 1.2-1.5 nm, the critical transition pressure is expected in the range of 1.7-3 GPa [173,176,177,180,181]. The pressures at which the anomaly in the pressure dependence of the optical transitions occurs in case of all investigated SWCNT films (see Figure 4.44), lie in the range of the expected critical transition pressure. Furthermore, recent theoretical investigations on the nature of the deformation of the SWCNTs found that the SWCNTs of diameter less than 2.5 nm undergo a transition from a circular to an oval shape and do not collapse, while the tubes with larger diameters do collapse [181]. Hence, the anomaly found in the experiments within this project could be attributed to the structural phase transition in the nanotubes, where the circular cross-section is deformed to an oval shape.

Resonant Raman studies on individualized nanotubes under pressure report critical pressures for radial deformation as 10 GPa and 4 GPa for nanotubes of diameters 0.8-0.9 nm and 1.2-1.3 nm, respectively [190]. Furthermore, it is interesting to note that some experiments have found no significant deformation effects up to very high pressures in bundled nanotubes [195–197,233]. For example, no anomaly was observed in the resonant Raman spectroscopy on bundled carbon nanotubes for pressures up to 40 GPa [196]. The absence of any pressure-induced anomaly was suggested to be the result of the adsorption of argon in the tubes [196]. Other recent measurements on the purified nanotubes also suggest that the pressure transmitting media play a very important role in determining the critical pressure at which the structural phase transition occurs, due to adsorption effects [195, 234]. In contrast to these reports, the anomalies in the pressure dependence of the optical transitions which are reported here are observed irrespective of the pressure transmitting medium used. Of course, the observation of the anomalies can not exclude the physical adsorption of argon on the SWCNTs during the pressure measurements.

Although the electronic properties of the bundled carbon nanotubes are changed considerably with increasing pressure, the pressure-induced changes in the optical transition energies are almost completely reversible: The energies of the optical transitions were reversible on releasing pressure though the intensities of the optical transitions were not regained completely. The reversibility of the pressure-induced transformations in the nanotubes has been controversial [177,189]. Sluiter et al. suggested a phase diagram for SWCNT bundles which could explain the inconsistency in the reversibility of the pressure-induced changes in various experimental investigations [177]. According to this phase diagram, the critical pressure at which the radial deformation occurs is lower than the cross-linking pressure. At the cross-linking pressure, the deformed nanotubes in the bundles start linking to each other similar to a polymerization effect. Therefore, the reversibility of the experimental data may not be observed when the highest measured pressure is above the cross-linking pressure. Still, the cross-linking of the nanotubes cannot be completely ruled out during the pressure experiments within this work: Based on the density functional electronic structure simulations, it was also suggested that the cross-linking is reversible when the circumference of the nanotubes is greater than 38 Å [177]. The SWCNTs investigated within this work have an average circumference of 41 Å. This implies that the cross-linkings even if they occur would be completely reversible on pressure release.

Interestingly, no anomaly in the FIR optical conductivity is observed at 2 GPa corresponding to the anomaly observed in the pressure-dependence of the optical transitions even though the higher energy optical transitions exhibit evidence for the structural phase transition. Instead the pressure dependence of the Drude parameters exhibits a monotonic behavior (see Figure 4.34 and Figure 4.40 for pressure dependence of the Drude parameters obtained from the optical conductivity of the unoriented SWCNT films and the magnetically-aligned SWCNT film, respectively). The presence of the SWCNT of different diameters and chiralities present in the film may probably lead to the smearing out of the evidence for the structural phase transition in the low-energy optical conductivity of the SWCNTs. Such a smeared out tube-to-tube variation in the chemical potential was also cited as a reason for very weak temperature dependence of SWCNTs in the FIR energy range [168].

4.6 Summary

Pressure-dependent infrared spectroscopic measurements on both unoriented and oriented SWCNT films were performed over a broad frequency range for the first time for pressures up to 8 GPa. The pressure dependence of the optical transitions and the low-energy excitations have been investigated.

All investigated SWCNT films consist of contributions from both metallic and semiconducting tubes, i.e., a finite optical conductivity in the FIR due to the itinerant carriers in the metallic tubes and the optical transitions corresponding to both metallic and semiconducting tubes in the MIR-visible frequency range. In the oriented nanotube films, a strong anisotropy is observed in the optical conductivity for $\mathbf{E}\|$alignment direction and $\mathbf{E}\perp$alignment direction. The optical transitions at higher energies in all films shift to lower energies with increasing pressure. This red-shift of the optical transitions are most likely due to the significant $\sigma^* - \pi^*$ hybridization effects arising from the pressure-induced deformation of the nanotubes. The pressure dependence of the optical transitions exhibit an anomaly at around 2 GPa for the unoriented nanotube films and the nanotubes-polymer matric and at around 2.7 GPa for the magnetically-aligned SWCNT film. The critical pressure at which the anomaly occurs is in agreement with that expected according to the theoretical and Raman spectroscopic investigations. This anomaly, observed for the first time in the infrared spectroscopic measurements, is attributed to the pressure-induced structural phase transitions in the SWCNTs where the circular cross-section of the nanotubes is deformed to an oval shape. In contrast to the suggestions that the adsorption of argon used as pressure transmitting medium prevents observation of pressure-induced phase transition, the experiments performed within this work show clear anomalies corresponding to this structural phase transition irrespective of the pressure transmitting medium.

The FIR transmittance/reflectance could be described by the model using the effective medium approximation reliably using a Drude term. This suggests that the low-energy optical conductivity is dominated by the purely metallic carriers which are localized due to the finite length effects and defects along the SWCNTs. Both the as-prepared and the purified SWCNT films exhibit very little temperature dependence. The free-standing SWCNTs, both the unoriented and the oriented SWCNT films, exhibit very similar pressure dependence. For the unoriented SWCNT films and the magnetically-aligned SWCNT film, the low-energy optical conductivity decreases with increasing pressure while the low-energy optical conductivity of the oriented nanotubes in the polyethylene has a nearly pressure-independent behavior. The decrease in the optical conductivity may be attributed to the gradual increase in localization of carriers caused by defects and deformations induced under high pressure, leading to a metal-to-insulator transition. Thus, the various pressure-induced phenomena on the low-energy electronic properties including the FIR energy range, could be addressed using the infrared spectroscopy under high pressure.

5 Conclusions and outlook

As a part of this project, the pressure-dependent infrared spectroscopic measurements on the fullerene-based compounds pristine C_{70}, $C_{60}\cdot C_8H_8$ and $C_{70}\cdot C_8H_8$ were performed over a broad energy range for pressure up to 10 GPa. Both vibrational and electronic properties of these compounds could be investigated under pressure.

The fundamental vibrational modes of solid C_{70} exhibit significant pressure dependence. An anomaly found in the pressure dependence of the vibrational modes of C_{70} at around 0.8 GPa, could be attributed to the orientational ordering transition where the uniaxial motion of the fullerenes is completely stopped. In addition to the fundamental vibrational modes, few other modes which are probably Raman or silent modes activated due to crystal field effects, were also observed. The intensity of these weak vibrational modes increased gradually with increasing pressure starting from the pressure around 1 GPa. This suggests an increase in intermolecular interactions and structural distortion in the crystalline C_{70} with the application of pressure. The electronic absorption of solid C_{70} was also studied as a function of pressure from the NIR-visible spectra. The electronic absorption edge of the C_{70} was found at 1.77 eV. The optical absorption edge shifted to lower energies with increasing pressure due to increasing intermolecular interactions. The negative pressure coefficient of -0.077 eV/GPa is in good agreement with the expected deformation potential of C_{70}.

Pressure-dependent transmittance measurements over a broad frequency range (infrared to visible) on $C_{60}\cdot C_8H_8$ and $C_{70}\cdot C_8H_8$ reveal pressure-induced phase transitions and give an insight into the nature of interactions in this new class of rotor-stator compounds. The pressure dependence of the vibrational modes in $C_{60}\cdot C_8H_8$ shows anomalies at 0.5 and 1.3 GPa, the first of which is assigned to a pressure-induced orientational ordering transition of the fullerene molecules. The second anomaly is probably correlated with fullerene-cubane interactions. The cubane molecules in $C_{70}\cdot C_8H_8$ are more sensitive to the application of pressure than in $C_{60}\cdot C_8H_8$, reflecting the stronger molecular recognition interactions in $C_{70}\cdot C_8H_8$ due to more effective space filling. The cubane modes exhibit pressure-induced splittings into several lines at 0.8 and 1.75 GPa which are interpreted in terms of symmetry changes in the cubane molecules induced by distortions.

For both $C_{60}{\cdot}C_8H_8$ and $C_{70}{\cdot}C_8H_8$, the energy of the absorption threshold shifts to lower energies with increasing pressure due to an increasing overlap of the molecular orbitals. The absorption threshold of $C_{60}{\cdot}C_8H_8$ is larger than that of pristine C_{60} but less than expected based on intermolecular distance, indicating that the cubane molecules do not simply act as spacers reducing the overlap of the C_{60} molecular orbitals, but heteromolecular overlap caused by molecular recognition plays a role as well. In $C_{70}{\cdot}C_8H_8$ practically no shift of the optical absorption edge is observed, in agreement with the enhanced molecular recognition interactions compared to $C_{60}{\cdot}C_8H_8$.

Thus, the pressure-dependent investigations on the vibrational and electronic properties of the fullerene-based compounds identifies the various pressure-induced orientational ordering transitions and the dominant role of the intermolecular interactions in determining the electronic properties of these systems.

In order to understand the electronic properties of SWCNTS, the pressure-dependent infrared spectroscopic measurements on the SWCNT films were performed over a broad frequency range for pressures up to 8 GPa. The very first polarization-dependent infrared spectroscopic measurements on oriented SWCNT films, namely, the oriented nanotubes in polyethylene matrix and the magnetically-aligned SWCNT film, have been performed over a broad frequency range. A strong anisotropy is observed in the optical conductivity of SWCNT film for polarizations $\mathbf{E}\|$alignment direction and $\mathbf{E}\perp$alignment direction.

The FIR transmittance/reflectance could be described by a Drude term which corresponds to contributions from itinerant charge carriers using the effective medium approximation model reliably. This indicate that the low-energy optical conductivity is dominated by the purely metallic carriers which are localized due to the finite length effects and defects along the SWCNTs.

The unoriented SWCNT films exhibit significant pressure-induced changes in the electronic properties but very little temperature dependence. For the unoriented SWCNT films and the magnetically-aligned films, the low-energy optical conductivity decreases with increasing pressure while the low-energy optical conductivity of the oriented nanotubes in the polyethylene exhibited a nearly pressure-independent behavior. The decrease in the low-energy optical conductivity in the magnetically-aligned SWCNT film is less pronounced when compared to the unoriented SWCNT film. This decrease in the optical conductivity could be attributed to the gradual increase in localization of carriers caused by defects and deformations induced under high pressure which would eventually lead to a metal-to-insulator transition. In case of the magnetically-aligned film, the optical conductivity for $\mathbf{E}\perp$alignment direction exhibits a similar pressure dependence as that for $\mathbf{E}\|$alignment direction, suggesting that the main contribution arises from the fraction of unoriented SWCNTs in the film. Furthermore, no signatures for a pressure-induced dimensional-crossover is observed.

The optical transitions at higher energies in all studied films shift to lower energies with increasing pressure. This red-shift of the optical transitions are most likely due to the significant $\sigma^* - \pi^*$ hybridization effects arising from the pressure-induced deformation of the nanotubes. The optical transitions corresponding to both semiconducting and metallic tubes exhibit comparable pressure dependence. The pressure dependence of the optical transitions exhibit an anomaly at around 2 GPa for the unoriented nanotube films and the nanotubes-polymer matrix and at around 2.7 GPa for the magnetically-aligned SWCNT film. The critical pressure at which the anomaly occurs is in agreement with that expected according to the theoretical and Raman spectroscopic investigations. This anomaly, observed for the first time in the infrared spectroscopic measurements, is attributed to the pressure-induced structural phase transitions in the SWCNTs where the circular cross-section of the nanotubes is deformed to an oval shape. In contrast to earlier reports that the anomaly due to the structural phase transition can not be observed while using argon as pressure transmitting medium, the anomalies have indeed been observed in the investigations within this project irrespective of the pressure transmitting medium used.

Thus, the pressure-induced phenomena in the electronic band structure of the SWCNTs have been extensively studied by investigating the low-energy electrodynamics of both unoriented and oriented SWCNT films.

Bibliography

[1] F. Wooten, *Optical properties of Solids* (Academic press, USA, 1972).

[2] M. Fox, *Optical properties of Solids* (Oxford University press, New York, USA, 2001).

[3] M. Dressel and G. Grüner, *Electrodynamics of Solids* (Cambridge University press, UK, 2002).

[4] I. Webman, J. Jortner, and M. H. Cohen, Phys. Rev. B **15**, 5712 (19771).

[5] R. W. Cohen, G. D. Cody, M. D. Coutts, and B. Abeles, Phys. Rev. B **8**, 3689 (1973).

[6] J. A. Osborn, Phys. Rev. **67**, 351 (1945).

[7] M. Y. Koledintseva, R. E. DuBroff, and R. W. Schwartz, PIER **63**, 223 (2006).

[8] J. P. Marton and J. R. Lemon, Phys. Rev. B **4**, 271 (1971).

[9] A. Jayaraman, Rev. Sci. Instrum. **57**, 1013 (1986).

[10] M. I. Eremets, *High pressure experiemental methods* (Oxford university press, New York, 1996).

[11] A. Jayaraman, Rev. Mod. Phys. **55**, 65 (1983).

[12] G. J. Piermarini and S. Block, Rev. Sci. Instrum. **46**, 973 (1975).

[13] W. A. Bassett, T. Takahashi, and P. W. Stook, Rev. Sci. Instrum. **38**, 37 (1967).

[14] G. Huber, K. Syassen, and W. B. Holzapfel, Phys. Rev. B **15**, 5123 (1977).

[15] L. Merrill and W. A. Bassett, Rev. Sci. Instrum. **45**, 290 (1974).

[16] D. J. Dunstan, Rev. Sci. Instrum. **60**, 3789 (1989).

[17] D. J. Dunstan and I. L. Spain, J. Phys. E **22**, 913 (1989).

[18] S. Sugano and Y. Tanabe, J. Phys. Soc. Japan **13**, 880 (1958).

[19] S. Sugano and Y. Tanabe, J. Phys. Soc. Japan **13**, 899 (1958).

[20] R. M. Macfarlane, J. Chem. Phys. **42**, 442 (1965).

[21] D. F. Nelson and M. D. Sturge, Phys. Rev. **137**, A1117 (1965).

[22] K. Syassen, private communication.

[23] D. E. McCumber and M. D. Sturge, J. Appl. Phys. **34**, 1682 (1963).

[24] J. D. Barnett, S. Block, and G. J. Piermarini, Rev. Sci. Instrum. **44**, 1 (1972).

[25] C. Ulrich, E. Anastassakis, K. Syassen, A. Debernardi, and M. Cardona, Phys. Rev. Lett. **78**, 1283 (1997).

[26] G. J. Piermarini, S. Block, J. D. Barnett, and R. A. Forman, J. Appl. Phys. **46**, 2774 (1975).

[27] H. K. Mao, J. Xu, and P. M. Bell, J. Geophys. Res. **91**, 4673 (1986).

[28] L. Oriel, *MS260i imaging spectrograph information manual.*

[29] W. F. Sherman and A. A. Stadtmuller, *Experimental Techniques in high-pressure research* (John Wiley and Sons limited, Great Britain, 1987).

[30] I. F. Silvera and R. J. Wijngaarden, Rev. Sci. Instrum. **56**, 121 (1985).

[31] D. H. Liebenberg, Phys. Lett. A **73**, 74 (1979).

[32] R. L. Mills, D. H. Liebenberg, J. C. Bronson, and L. C. Schimdt, Rev. Sci. Instrum. **51**, 891 (1980).

[33] J. M. Besson and J. P. Pinceaux, Science **206**, 1073 (1979).

[34] M. I. Eremets and Y. A. Timofeev, Rev. Sci. Instrum. **63**, 3123 (1992).

[35] E. D. Palik, *Handbook of optical constants of solids* (Academic press, USA, 1998).

[36] M. Born and E. Wolf, *Principles of optics: Electromagnetic theory of propagation, interference, and diffraction of light* (Pergamon Press, London, 1959).

[37] K. Urban, C. M. Schneider, T. Brückel, S. Blügel, K. Tillmann, W. Schweika, M. Lentzen, and L. Baumgarten, *Probing the nanoworld - Microscopies, scattering and spectroscopies of the solid state* (Forschungszentrum Jülich, Germany, 2007).

[38] Y. L. Mathis, H. O. Moser, and R. Steininger, Ferroelectrics **249**, 11 (2001).

[39] T. Baumbach, J. Göttlicher, and M.Hagelstein, *ANKA Instrumentation Book*, 2005.

[40] Cryovac, *Cryovac konticryostat instruction manual*, 2003.

[41] M. S. Dresselhaus, G. Dresselhaus, and P. C. Eklund, *Science of fullerenes and carbon nanotubes* (Academic Press, USA, 1996).

[42] R. E. Stanton and M. D. Newton, J. Phys. Chem. **92**, 2141 (1988).

[43] W. Krätschmer, L. D. Lamb, K. Fostiropoulos, and D. R. Huffmann, Nature **347**, 354 (1990).

[44] W. Krätschmer, K. Fostiropoulos, and D. R. Huffmann, Chem. Phys. Lett. **170**, 167 (1990).

[45] D. S. Bethune, G. Meijer, W. C. Tang, H. J. Rosen, W. G. Golden, H. Seki, C. A. Brown, and M. S. de Vries, Chem. Phys. Lett. **179**, 181 (1991).

[46] M. C. Martin, X. Du, J. Kwon, and L. Mihaly, Phys. Rev. B **50**, 173 (1994).

[47] S. Saito and A. Oshiyama, Phys. Rev. Lett. **66**, 2637 (1991).

[48] E. L. Shirley and S. G. Louie, Phys. Rev. Lett. **71**, 133 (1993).

[49] G. Gensterblum, J. J. Pireaux, P. A. Thiry, R. Caudano, J. P. Vigneron, P. Lambin, A. A. Lucas, and W. Krätschmer, Phys. Rev. Lett. **67**, 2171 (1991).

[50] R. W. Lof, M. A. van Veenendaal, B. Koopmans, H. T. Jonkman, and G. A. Sawatzky, Phys. Rev. Lett. **68**, 3924 (1992).

[51] C. Hartmann, M. Zigone, G. Martinez, E. L. Shirley, L. X. Benedict, S. G. Louie, M. S. Fuhrer, and A. Zettl, Phys. Rev. B **52**, R5550 (1995).

[52] M. S. Golden, M. Knupfer, J. Fink, J. F. Armbruster, T. R. Cummins, H. A. Romberg, M. Roth, M. Sing, M. Schmidt, and E. Sohmen, J. Phys.: Condens. Matter **7**, 8219 (1995).

[53] G. A. Samara, L. V. Hansen, R. A. Assink, B. Morosin, J. E. Schirber, and D. Loy, Phys. Rev. B **47**, 4756 (1993).

[54] J. E. Schirber, G. H. Kwei, J. D. Jorgensen, R. L. Hitterman, and B. Morosin, Phys. Rev. B **51**, 12014 (1995).

[55] K. P. Meletov, D. Christofilos, G. A. Kourouklis, and S. Ves, Chem. Phys. Lett. **236**, 265 (1995).

[56] K. P. Meletov, D. Christofilos, S. Ves, and G. A. Kourouklis, Phys. Rev. B **52**, 10090 (1995).

[57] S. J. Jeon, D. Kim, S. K. Kim, and I. C. Jeon, J. Raman Spectrosc. **23**, 311 (1992).

[58] Y. Huang, D. F. R. Gilson, and I. S. Butler, J. Phys. Chem. **95**, 5723 (1991).

[59] V. D. Blank, S. G. Buga, G. A. Dubitsky, N. R. Serebryanaya, M. Y. Popov, and B. Sundqvist, Carbon **36**, 319 (1998).

[60] B. Sundqvist, Advances in Physics **48**, 1 (1999).

[61] E. Burgos, E. Halac, and H. Bonadeo, Phys. Rev. B **49**, 15544 (1994).

[62] B. Sundqvist, O. Andersson, A. Lundin, and A. Soldatov, Solid State Commun. **93**, 109 (1995).

[63] A. Lundin and B. Sundqvist, Europhys. Lett. **27**, 463 (1994).

[64] O. Andersson, A. Soldatov, and B. Sundqvist, Mater. Res. Soc. Symp. Proc. **359**, 549 (1995).

[65] J. A. Wolk, P. J. Horoyski, and M. L. W. Thewalt, Phys. Rev. Lett. **74**, 3483 (1995).

[66] O. Blaschko, W. Rom, and I. N. Goncharenko, J. Phys:. Condens. Matter **8**, 4235 (1996).

[67] R. Komori, T. Nagaosa, T. Hatae, and Y. Miyamoto, Jpn. J. Appl. Phys. **36**, 5600 (1997).

[68] K. Raghavachari and C. M. Rohlfing, J. Phys. Chem. **95**, 5768 (1991).

[69] A. von Czarnowski and K. H. Meiwes-Broer, Chem. Phys. Lett. **246**, 321 (1995).

[70] P. Bowmar, W. Hayes, M. Kurmoo, P. A. Pattenden, M. A. Green, P. Day, and K. Kikuchi, J. Phys:. Condens. Matter **6**, 3161 (1994).

[71] R. E. Stratmann, G. E. Scuseria, and M. J. Frisch, J. Raman spectrosc. **29**, 483 (1998).

[72] W. Andreoni, F. Gygi, and M. Parrinello, Chem. Phys. Lett. **189**, 241 (1992).

[73] M. Sprik, A. Cheng, and M. L. Klein, Phys. Rev. Lett. **69**, 1660 (1992).

[74] G. B. M. Vaughan, P. A. Heiney, D. E. Cox, J. E. Fischer, A. R. McGhie, A. L. Smith, R. M. Strongin, M. A. Cichy, and A. B. S. III, Chem. Phys. **178**, 599 (1993).

[75] G. A. Samara, L. V. Hansen, B. Morosin, and J. E. Schirber, *High pressure science and technology* (American Institute of Physics, New York, 1994), p. 643.

[76] G. A. Samara, L. V. Hansen, B. Morosin, and J. E. Schirber, Phys. Rev. B **53**, 5211 (1996).

[77] A. Lundin, A. Soldatov, and B. Sundqvist, Europhys. Lett. **30**, 469 (1995).

[78] A. Soldatov and B. Sundqvist, J. Phys. Chem. Solids **57**, 1371 (1996).

[79] C. Christides, I. M. Thomas, T. J. S. Dennis, and K. Prassides, Europhys. Lett. **22**, 611 (1993).

[80] A. K. Sood, N. Chandrabhas, D. V. S. Muthu, Y. Hariharan, A. Bharathi, and C. S. Sundar, Phil. Mag. B **70**, 347 (1994).

[81] A. A. Maksimov, K. P. Meletov, Y. A. Ossipyan, I. I. Tartakovskii, Y. V. Artemov, and M. A. Nudel'man, JETP Lett. **57**, 816 (1993).

[82] K. Meletov, A. Maksimov, Y. Ossipyan, and I. Tartakovskii, Mol. Cryst. Liq. Cryst. **256**, 909 (1994).

[83] D. W. Snoke, Y. S. Raptis, and K. Syassen, Phys. Rev. B **45**, 14419 (1992).

[84] Y. Iwasa, T. Furudate, T. Fukawa, T. Ozaki, T. Mitani, T. Yagi, and T. Arima, Appl. Phys. A **64**, 251 (1997).

[85] H. Kawamura, M. Kobayashi, Y. Akahama, H. Shinohara, H. Sato, and Y. Saito, Solid State Commun. **83**, 563 (1992).

[86] H. Kawamura, Y. Akahama, M. Kobayashi, H. Shinohara, H. Sato, Y. Saito, T. Kikegawa, O. Shimomura, and K. Aoki, J. Phys. Chem. Solids **54**, 1675 (1993).

[87] H. Kawamura, Y. Akahama, M. Kobayashi, Y. Hasegawa, H. Shinohara, H. Sato, and Y. Saito, Jpn. J. Appl. Phys. **32**, L101 (1993).

[88] A. Lundin, A. Soldatov, and B. Sundqvist, Mat. Res. Soc. Symp. Proc. **359**, 555 (1995).

[89] Y. Maniwa, A. Ohi, K. Mizoguchi, K. Kume, K. Kikuchi, K. Saito, I. Ikemoto, S. Suzuki, and Y. Achiba, J. Phys. Soc. Jpn. **62**, 1131 (1993).

[90] H. Kawamura, Y. Akahama, M. Kobayashi, H. Shinohara, and Y. Saito, J. Phys. Soc. Jpn. **63**, 2445 (1994).

[91] H. Yamawaki, M. Yoshida, Y. Kakudate, S. Usuba, H. Yokoi, S. Fujiwara, and K. Aoki, J. Phys. Chem. **97**, 11161 (1993).

[92] K. Kamarás, private communication.

[93] A. R. McGhie, J. E. Fischer, P. A. Heiney, P. W. Stephens, R. L. Cappelletti, D. A. Neumann, W. H. Mueller, H. Mohn, and H. U. ter Meer, Phys. Rev. B **49**, 12614 (1994).

[94] K. Kniaz, J. E. Fischer, A. R. McGhie, L. A. Girifalco, R. M. Strongin, and A. B. S. III, Solid State Commun. **96**, 739 (1995).

[95] V. Schettino, M. Pagliai, and G. Cardini, J. Phys. Chem. A **106**, 1815 (2002).

[96] P. H. M. van Loosdrecht, P. J. M. van Bentum, M. A. Verheijen, and G. Meijer, Chem. Phys. Lett. **198**, 587 (1992).

[97] Z. H. . Dong, P. Zhou, J. M. Holden, P. C. Eklund, M. S. Dresselhaus, and G. Dresselhaus, Phys. Rev. B **48**, 2862 (1993).

[98] K. Thirunavukkuarasu, C. A. Kuntscher, F. Borondics, G. Klupp, and K. Kamarás, phys. stat. sol. (b) **245**, 2006 (2008).

[99] M. Premila, C. S. Sundar, P. C. Sahu, A. Bharathi, Y. Hariharan, D. V. S. Muthu, and A. K. Sood, Solid State Commun. **104**, 237 (1997).

[100] S. Wasa, K. Suito, M. Kobayashi, and A. Onodera, Solid State Commun. **114**, 209 (2000).

[101] K. P. Meletov, V. K. Dolganov, and Y. A. Ossipyan, Solid State Commun. **87**, 639 (1993).

[102] V. K. Dolganov, O. V. Zharikov, I. N. Kremenskaja, K. P. Meletov, and Y. A. Ossipyan, Solid State Commun. **83**, 63 (1992).

[103] M. Ichida, M. Sakai, T. Karasawa, T. Komatsu, and A. Nakamura, Solid State Commun. **118**, 119 (2001).

[104] E. L. Shirley, L. X. Benedict, and S. G. Louie, Phys. Rev. B **54**, 10970 (1996).

[105] A. K. Sood, N. Chandrabhas, D. Victor, S. Muthu, A. Jayaraman, N. Kumar, H. R. Krishnamurthy, T. Pradeep, and C. N. R. Rao, Solid State Commun. **81**, 89 (1992).

[106] P. E. Eaton and T. W. C. Jr., J. Am. Chem. Soc. **86**, 3157 (1964).

[107] P. E. Eaton, Angew. Chem. Int. Ed. Engl. **311**, 1421 (1992).

[108] E. W. Della, E. F. McCoy, H. K. Patney, G. L. Jones, and F. A. Miller, J. Am. Chem. Soc. **101**, 7441 (1979).

[109] V. Galasso, Chem. Phys. **184**, 107 (1994).

[110] M. A. White, R. E. Wasylishen, P. E. Eaton, Y. Xiong, K. Pramod, and N. Nodari, J. Phys. Chem. **96**, 421 (1992).

[111] N. A. Murugan, J. Chem. Phys. **123**, 244514 (2005).

[112] T. Yildirim, S. Ciraci, C. Kilic, and A. Buldum, Phys. Rev. B **62**, 7625 (2000).

[113] G. J. Piermarini, S.Block, R. Damavarapu, and S. Iyer, Prop. Expl. Pyro. **16**, 188 (1991).

[114] S. Pekker, É. Kováts, G. Oszlányi, G. Bényei, G. Klupp, G. Bortel, I. Jalsovszky, E. Jakab, F. Borondics, K. Kamarás, M. Bokor, G. Kriza, K. Tompa, and G. Faigel, Nature Materials **4**, 784 (2005).

[115] S. Pekker, É. Kováts, G. Oszlányi, Gy. Bényei, G. Klupp, G. Bortel, I. Jalsovszky, E. Jakab, F. Borondics, K. Kamarás, and G. Faigel, phys. stat. sol. (b) **243**, 3032 (2006).

[116] G. Bortel, G. Faigel, É. Kováts, G. Oszlányi, and S. Pekker, phys. stat. sol. (b) **243**, 2999 (2006).

[117] B. Sundaqvist, A. Iwasiewicz-Wabnig, E. Kováts, and S. Pekker, Mater. Res. Symp. Proc. **987**, PP03 (2007).

[118] A. Iwasiewicz-Wabnig, B. Sundaqvist, É. Kováts, I. Jalsovszky, and S. Pekker, Phys. Rev. B **75**, 024114 (2007).

[119] G. Klupp, F. Borondics, É. Kováts, Á. Pekker, G. Bényei, I. Jalsovszky, R. Hackl, K. Kamarás, and S. Pekker, J. Phys. Chem. B **111**, 12375 (2007).

[120] C. A. Kuntscher, S. Frank, K. Kamarás, G. Klupp, É. Kováts, S. Pekker, G. Bényei, and I. Jalsovszky, phys. stat. sol. (b) **243**, 2981 (2006).

[121] K. Thirunavukkuarasu, C. A. Kuntscher, G. Bényei, I. Jalsovszky, G. Klupp, K. Kamarás, E. Kovats, and S. Pekker, J. Phys. Chem. C **112**, 17525 (2008).

[122] D. W. Snoke, K. Syassen, and A. Mittelbach, Phys. Rev. B **47**, 4146 (1993).

[123] B. Sundqvist, phys. stat. sol. (b) **223**, 469 (2001).

[124] K. P. Meletov, V. K. Dolganov, O. V. Zharikov, I. N. Kremeenskava, and Y. A. Ossipyan, J. Phys. Paris **2**, 2097 (1992).

[125] K. P. Meletov, G. A. Kourouklis, D. Christofilos, and S. Ves, J. exp. theoret. Physics **81**, 798 (1995).

[126] K. P. Meletov, D. Christofilos, S. Ves, and G. A. Kourouklis, phys. stat. sol. (b) **198**, 553 (1996).

[127] K. Kamarás, A. Breitschwerdt, S. Pekker, K. Fodor-Csorba, G. Faigel, and M. Tegze, Appl. Phys. A **56**, 231 (1993).

[128] S. Pekker, G. Faigel, K. Fodor-Csorba, L. Gránásy, E. Jakab, and M. Tegze, Solid State Commun. **83**, 423 (1992).

[129] S. Pekker, G. Faigel, G. Oszlányi, M. Tegze, T. Kemény, and E. Jakab, Synthetic Metals **55-57**, 3014 (1993).

[130] P. A. Heiney, J. E. Fischer, A. R. McGhie, W. J. Romanow, A. M. Denenstein, J. J. P. McCauley, A. B. S. III, and D. E. Cox, Phys. Rev. Lett. **66**, 2911 (1991).

[131] L. Jiang, J. Li, L. A. Nagahara, N. Kino, K. Kitazawa, T. Iyoda, K. Hashimoto, and A. Fujishima, Appl. Phys. A **61**, 17 (1995).

[132] D. H. Oh and Y. H. Lee, Phys. Rev. Lett. **75**, 4230 (1995).

[133] V. Zólyomi, J. Koltai, J. Kürti, and S. Pekker, Phys. Rev. B **78**, 115405 (2008).

[134] J. C. Charlier, X. Blase, and S. Roche, Rev. Mod. Phys. **79**, 677 (2007).

[135] M. S. Dresselhaus, G. Dresselhaus, J. C. Charlier, and E. Hernández, Phil. Trans. R. Soc. Lond. A **362**, 2065 (2004).

[136] P. R. Wallace, Phys. Rev. **71**, 622 (1947).

[137] S. Reich, C. Thomsen, and J. Maultzsch, *Carbon nanotubes: Basic concepts and physical properties* (Wiley-VCH, Weinheim, 2004).

[138] M. Cardona and R. Merlin, *Light scattering in solids IX, Topics in applied physics* (Springer-Verlag, Berling Heidelberg, 2007), Vol. 108, p. 115.

[139] J. W. Mintmire and C. T. White, Phys. Rev. Lett. **81**, 2506 (1998).

[140] R. Saito, G. Dresselhaus, and M. S. Dresselhaus, Phys. Rev. B **61**, 2981 (2000).

[141] S. Reich and C. Thomsen, Phys. Rev. B **62**, 4273 (2000).

[142] C. L. Kane and E. J. Mele, Phys. Rev. Lett. **78**, 1932 (1997).

[143] M. Ouyang, J. L. Huang, C. L. Cheung, and C. M. Lieber, Science **292**, 702 (2001).

[144] X. Blase, L. X. Benedict, E. L. Shirley, and S. G. Louie, Phys. Rev. Lett. **72**, 1878 (1994).

[145] P. Delaney, H. J. Choi, J. Ihm, S. G. Louie, and M. L. Cohen, Nature **391**, 466 (1998).

[146] J. C. Charlier, X. Gonze, and J. P. Michenaud, Europhys. Lett. **29**, 43 (1995).

[147] A. M. Rao, J. Chen, E. Richter, U. Schlecht, P. C. Eklund, R. C. Haddon, U. D. Venkateswaran, Y. K. Kwon, and D. Tománek, Phys. Rev. Lett. **86**, 3895 (2001).

[148] S. Reich, C. Thomsen, and P. Ordejón, Phys. Rev. B **65**, 155411 (2002).

[149] A. Rubio, Appl.Phys. A **68**, 275 (1999).

[150] M. J. O'Connell, S. Sivaram, and S. K. Doorn, Phys. Rev. B **69**, 235415 (2004).

[151] H. Kataura, Y. Kumazawa, Y. Maniwa, I. Umezu, S. Suzuki, Y. Ohtsuka, and Y. Achiba, Synthetic Metals **103**, 2555 (1999).

[152] S. Tasaki, K. Maekawa, and T. Yamabe, Phys. Rev. B **57**, 9301 (1998).

[153] S. M. Bachilo, M. S. Strano, C. Kittrell, R. H. Hauge, R. E. Smalley, and R. B. Weisman, Science **298**, 2361 (2002).

[154] M. J. O'Connell, S. M. Bachilo, C. B. Huffman, V. C. Moore, M. S. Strano, E. H. Haroz, K. L. Rialon, P. J. Boul, W. H. Noon, C. Kittrell, J. Ma, R. H. Hauge, R. B. Weisman, and R. E. Smalley, Science **297**, 593 (2002).

[155] C. L. Kane and E. J. Mele, Phys. Rev. Lett. **90**, 207401 (2003).

[156] M. S. Dresselhaus, G. Dresselhaus, R. Saito, and A. Jorio, Annu. Rev. Phys. Chem **58**, 719 (2007).

[157] C. D. Spataru, S. Ismail-Beigi, L. X. Benedict, and S. G. Louie, Phys. Rev. Lett. **92**, 077402 (2004).

[158] R. Loudon, Am. J. Phys **27**, 649 (1959).

[159] T. Ando, J. Phys. Soc. Jpn. **66**, 1066 (1997).

[160] A. Ugawa, A. G. Rinzler, and D. B. Tanner, Phys. Rev. B **60**, R11305 (1999).

[161] A. Ugawa, J. Hwang, H. H. Gommans, H. Tashiro, A. G. Rinzler, and D. B. Tanner, Current Appl. Phys. **1**, 45 (2001).

[162] O. Hilt, H. B. Brom, and M. Ahlskog, Phys. Rev. B **61**, R5129 (2000).

[163] J. Hone, I. Ellwood, M. Muno, A. Mizel, M. L. Cohen, and A. Zettl, Phys. Rev. Lett. **80**, 1042 (1998).

[164] F. Borondics, K. Kamarás, M. Nikolou, D. B. Tanner, Z. H. Chen, and A. G. Rinzler, Phys. Rev. B **74**, 045431 (2006).

[165] J. M. Benoit, B. Corraze, and O. Chauvet, Phys. Rev. B **65**, 241405 (2002).

[166] M. S. Fuhrer, M. L. Cohen, A. Zettl, and V. Crespi, Solid State Commun. **109**, 105 (1999).

[167] J. Jiang, J. Dong, H. T. Yang, and D. Y. Xing, Phys. Rev. B **64**, 045409 (2001).

[168] T. Kampfrath, K. von Volkmann, C. M. Aguirre, P. Desjardins, R. Martel, M. Kranz, C. Frischkorn, M. Wolf, and L. Perfetti, Phys. Rev. Lett. **101**, 267403 (2008).

[169] J. Lefebvre, P. Finnie, and Y. Homma, Phys. Rev. B **70**, 045419 (2004).

[170] R. B. Capaz, C. D. Spataru, P. Tangney, M. L. Cohen, and S. G. Louie, Phys. Rev. Lett. **94**, 036801 (2005).

[171] S. B. Cronin, Y. Yin, A. Walsh, R. B. Capaz, A. Stolyarov, P. Tangney, M. L. Cohen, S. G. Louie, A. K. Swan, M. S. ´Unl´u, B. B. Goldberg, and M. Tinkham, Phys. Rev. Lett. **96**, 127403 (2006).

[172] U. D. Venkateswaran, phys. stat. sol. (b) **241**, 3345 (2004).

[173] J. A. Elliott, J. K. W. Sandler, A. H. Windle, R. J. Young, and M. S. P. Shaffer, Phys. Rev. Lett. **92**, 095501 (2004).

[174] S. Okada, A. Oshiyama, and S. Saito, J. Phys. Soc. Jpn **70**, 2345 (2001).

[175] S. Reich, C. Thomsen, and P. Ordejon, Phys. Rev. B **65**, 153407 (2002).

[176] S. P. Chan, W. L. Yim, X. G. Gong, and Z. F. Liu, Phys. Rev. B **68**, 075404 (2003).

[177] M. H. F. Sluiter and Y. Kawazoe, Phys. Rev. B **69**, 224111 (2004).

[178] C. Li and T. W. Chou, Phys. Rev. B **69**, 073401 (2004).

[179] X. H. Zhang, D. Y. Sun, Z. F. Liu, and X. G. Gong, Phys. Rev. B **70**, 035422 (2004).

[180] R. B. Capaz, C. D. Spataru, P. Tangney, M. L. Cohen, and S. G. Louie, phys. stat. sol. (b) **241**, 3352 (2004).

[181] M. Hasegawa and K. Nishidate, Phys. Rev. B **74**, 115401 (2006).

[182] J. C. Charlier, P. Lambin, and T. W. Ebbesen, Phys. Rev. B **54**, R8377 (1996).

[183] C. J. Park, Y. H. Kim, and K. J. Chang, Phys. Rev. B **60**, 10656 (1999).

[184] L. Yang and J. Han, Phys. Rev. Lett. **85**, 154 (2000).

[185] M. S. C. Mazzoni and H. Chacham, Appl. Phys. Lett. **76**, 1561 (2000).

[186] P. E. Lammert, P. Zhang, and V. H. Crespi, Phys. Rev. Lett. **84**, 2453 (2000).

[187] O. Gülseren, T. Yildirim, S. Ciraci, and C. Kilic, Phys. Rev. B **65**, 155410 (2002).

[188] J. Q. Lu, J. Wu, W. Duan, F. Liu, B. F. Zhu, and B. L. Gu, Phys. Rev. Lett. **90**, 156601 (2003).

[189] I. Loa, J. Raman. Spectrosc **34**, 611 (2003).

[190] S. Lebedkin, K. Arnold, O. Kiowski, F. Hennrich, and M. M. Kappes, Phys. Rev. B **73**, 094109 (2006).

[191] J. Tang, L.-C. Qin, T. Sasaki, M. Yudasaka, A. Matsushita, and S. Iijima, Phys. Rev. Lett. **85**, 1887 (2000).

[192] S. M. Sharma, S. Karmakar, S. K. Sikka, P. V. Teredesai, A. K. Sood, A. Govindaraj, and C. N. R. Rao, Phys. Rev. B **63**, 205417 (2001).

[193] S. Rols, I. N. Goncharenko, R. Almairac, J. L. Sauvajol, and I. Mirebeau, Phys. Rev. B **64**, 153401 (2001).

[194] S. Kazaoui, N. Minami, H. Yamawaki, K. Aoki, H. Kataura, and Y. Achiba, Phys. Rev. B **62**, 1643 (2000).

[195] M. S. Amer, M. M. El-Ashry, and J. F. Maguire, J. Chem. Phys. **121**, 2752 (2004).

[196] A. Merlen, N. Bendiab, P. Toulemonde, A. Aouizerat, A. S. Miguel, J. Sauvajol, G. Montagnac, H. Cardon, and P. Petit, Phys. Rev. B **72**, 035409 (2005).

[197] M. Monteverde and M. Núnez-Regueiro, Phys. Rev. Lett. **94**, 235501 (2005).

[198] F. Bommeli, L. Degiorgi, P. Wachter, W. S. Bacsa, W. A. de Heer, and L. Forro, Synthetic Metals **86**, 2307 (1997).

[199] M. E. Itkis, S. Niyogi, M. E. Meng, M. A. Hamon, H. Hu, and R. C. Haddon, Nano Letters **2**, 155 (2002).

[200] M. E. Itkis, D. E. Perea, S. Niyogi, S. M. Richard, M. A. Hamon, H. Hu, B. Zhao, and R. C. Haddon, Nano Letters **3**, 309 (2003).

[201] C. Journet and P. Bernier, Appl. Phys. A **67**, 1 (1998).

[202] F. Hennrich, S. Lebedkin, S. Malik, J. Tracey, M. Barczewski, H. Roesner, and M. Kappes, Phys. Chem. Chem. Phys. **4**, 2273 (2002).

[203] F. Hennrich, R. Wellmann, S. Malik, S. Lebedkin, and M. Kappes, Phys. Chem. Chem. Phys. **5**, 178 (2003).

[204] M. T. Martinez, M. A. Callejas, A. M. Benito, M. Cochet, T. Seeger, A. Ansón, J. Schreiber, C. Gordon, C. Marhic, O. Chauvet, and W. K. Maser, Nanotechnology **14**, 691 (2003).

[205] M. Shiraishi, T. Takenobu, A. Yamada, M. Ata, and H. Kataura, Chem. Phys. Lett. **358**, 213 (2002).

[206] N. Akima, Y. Iwasa, S. Brown, A. M. Barbour, J. Cao, J. L. Musfeldt, H. Matsui, N. Toyota, M. Shiraishi, H. Shimoda, and O. Zhou, Adv. Mater. **18**, 1166 (2006).

[207] D. A. Walters, M. J. Casavant, X. C. Qin, C. B. Huffman, P. J. Boul, L. M. Ericson, E. H. Haroz, M. J. O'Connell, K. Smith, D. T. Colbert, and R. E. Smalley, Chem. Phys. Lett. **338**, 14 (2001).

[208] J. E. Fischer, W. Zhou, J. Vavro, M. C. Llaguno, C. Guthy, R. Haggenmueller, M. J. Casavant, D. A. Walters, and R. E. Smalley, J. Appl. Phys. **93**, 2157 (2003).

[209] A. C. Dillon, T. Gennett, K. M. Jones, J. L. Alleman, P. A. Parilla, and M. J. Heben, Adv. Mater. **11**, 1354 (1999).

[210] H. Hu, B. Zhao, M. E. Itkis, and R. C. Haddon, J. Phys. Chem. B **107**, 13838 (2003).

[211] M. Monthioux, B. Smith, B. Burteaux, A. Claye, J. E. Fischer, and D. Luzzi, Carbon **39**, 1251 (2001).

[212] J. Zhang, H. Zou, Q. Qing, Y. Yang, Q. Li, Z. Liu, X. Guo, and Z. Du, J. Phys. Chem. B **107**, 3712 (2003).

[213] A. Kuznetsova, D. B. Mawhinney, V. Naumenko, J. T. Y. Jr., J. Liu, and R. E. Smalley, Chem. Phys. Letters **321**, 292 (2000).

[214] S. Rols, M. R. Johnson, P. Zeppenfeld, M. Bienfait, O. E. Vilches, and J. Schneble, Phys. Rev. B **71**, 155411 (2005).

[215] T. Pichler, M. Knupfer, M. S. Golden, J. Fink, A. Rinzler, and R. E. Smalley, Phys. Rev. Lett. **80**, 4729 (1998).

[216] D. B. Tanner, A. J. Sievers, and R. A. Buhrman, Phys. Rev. B **11**, 1330 (1975).

[217] T. I. Jeon, K. J. Kim, C. Kang, I. H. Maeng, J. H. Son, K. H. An, J. Y. Lee, and Y. H. Lee, J. Appl. Phys. **95**, 5736 (2004).

[218] H. Altan, F. Huang, J. F. Federici, A. Lan, and H. Grebel, J. Appl. Phys. **96**, 6685 (2004).

[219] O. Jost, A. A. Gorbunov, W. Pompe, T. Pichler, R. Friedlein, M. Knupfer, M. Reibold, H. D. Bauer, L. Dunsch, M. S. Golden, and J. Fink, Appl. Phys. Lett. **75**, 2217 (1999).

[220] M. Hjort and S. Stafström, Phys. Rev. B **63**, 113406 (2001).

[221] K. Nordlund and P. Hakonen, Nature materials **4**, 514 (2005).

[222] W. Bu, J. Jiang, and J. Dong, Phys. Lett. A **302**, 125 (2002).

[223] L. J. Li, R. J. Nicholas, R. S. Deacon, and P. A. Shields, Phys. Rev. Lett. **93**, 156104 (2004).

[224] D. Karaiskaj and A. Mascarenhas, Phys. Rev. B **75**, 115426 (2007).

[225] C. A. Kuntscher, K. Thirunavukkuarasu, A. Pekker, K. Kamarás, F. Hennrich, M. Kappes, and Y. Iwasa, phys. stat. sol. (b) **244**, 3982 (2007).

[226] C. A. Kuntscher, K. Thirunavukkuarasu, K. Kamarás, F. Simon, and D. A. Walters, phys. stat. sol. (b) **245**, 2288 (2008).

[227] G. Liu, X. Wang, J. Chen, and H. Lu, phys. stat. sol. (b) **245**, 689 (2008).

[228] L. Yang, M. P. Anantram, J. Han, and J. P. Lu, Phys. Rev. B **60**, 13874 (1999).

[229] Y. N. Gartstein, A. A. Zakhidov, and R. H. Baughman, Phys. Rev. B **68**, 115415 (2003).

[230] J. Wu, W. Walukiewicz, W. Shan, E. Bourret-Courchesne, J. W. A. III, K. M. Yu, E. E. Haller, K. Kissell, S. M. Bachilo, R. B. Weisman, and R. E. Smalley, Phys. Rev. Lett. **93**, 017404 (2004).

[231] R. S. Deacon, K. C. Chuang, J. Doig, I. B. Mortimer, and R. J. Nicolas, Phys. Rev. B **74**, 201402(R) (2006).

[232] P. Puech, E. Flahaut, A. Sapelkin, H. Hubel, D. J. Dunstan, G. Landa, and W. S. Bacsa, Phys. Rev. B **73**, 233408 (2006).

[233] A. Merlen, P. Toulemonde, N. Bendiab, A. Aouizerat, J. Sauvajol, G. Montagnac, H. Cardon, P. Petit, and A. S. Miguel, phys. stat. sol. (b) **243**, 690 (2006).

[234] J. E. Proctor, M. P. Halsall, A. Ghandour, and D. J. Dunstan, J. Phys. Chem. Solids **67**, 2468 (2006).

Acknowledgements

I would like to express my gratitude to Prof. Dr. Christine Kuntscher for introducing me into the vast and interesting field of low-dimensional systems, and for offering constant guidance and dedicated attention in my work.

My immense thanks to our collaborator Dr. Katalin Kamarás not only for giving us the samples of fullerene-based compounds and some SWCNT films studied for this work, but also undoubtedly for her rewarding discussions. I thank our other collaborators Dr. F. Hennrich, Prof. Dr. M. Kappes, Prof. Y. Iwasa, Dr. F. Simon and Dr. D. A. Walters for providing the SWCNT films studied within this PhD project.

I would like to use this opportunity to express my profound gratitude to Prof. Dr. Martin Dressel, for paving way for my research career, and for offering his valuable support and discussions.

Of course, the research projects can not progress easily without the help from the technical assistants in the institute. Therefore, I convey my thanks to Ms. Gabriele Untereiner at 1. Physikaliches Institut, Universität Stuttgart and Ms. Beate Spörhase at Experimental Physik II, Universität Augsburg. A special thanks to Ms. Danuta Trojak for assistance during scanning electron microscopic measurements on carbon nanotubes films.

My thanks to all members of AG Kuntscher for creating a wonderful work environment. It is an extreme pleasure to thank my dear friends Dr. Alexej Pashkin, Dr. Simone Frank, Dr. Leonetta Baldassarre, Kaneez Rabia, Estaline Amitha Francis and Sindu John Louis for standing firmly by my side with their constant encouragement and moral support. I can not be forgetting their fruitful discussions and comments related to my work. I would also like to thank all my colleagues at Physikalisches Institut 1, for helping me in all possible ways during the early days of my PhD work.

Last but not the least, I thank my parents, husband, brother and sister for being my invisible strength and motivation no matter what happens, without which it would have been impossible for me to pursue my work.

Curriculum Vitae

Personal information

Date of birth : 29 May 1979
Nationality : Indian
Gender : Female
Martial status : Married

Education

Jun 1982 - May 1996	All India Secondary School Examination, Central Board of Secondary Education, India.
Jul 1996 - May 1999	Bachelor's degree (vocational) in Physics, University of Madras, Chennai, India.
Aug 2001 - Jun 2003	Master's degree in Physics, Indian Institute of Technology Madras, Chennai, India. Title: *Effect of sample preparation procedure on magnetotransport properties of polycrystalline bulk and epitaxial thin films of double perovskite* Sr_2FeMoO_6.
Aug 2003 - Nov 2004	Master's degree in Physics, Universität Stuttgart, Stuttgart, Germany. Title: *Electronic and Magnetic properties of quasi-one-dimensional titanates* $La_{1-y}Ca_yTiO_{3.4\pm\delta}$.
Nov 2004 - Jul 2006	Start of Ph.D in Physics, Universität Stuttgart, Stuttgart, Germany.
Aug 2006 - May 2009	Completion of Ph.D in Physics, Universität Augsburg, Augsburg, Germany.

List of publications

- *Far- and mid-infrared anisotropy of magnetically aligned single-wall carbon nanotubes studied with synchrotron radiation.*
  K. Kamarás, K. Thirunavukkuarasu, C.A. Kuntscher, M. Dressel, F. Simon, H. Kuzmany, D.A. Walters, and D.A. Moss,
  Infrared Physics & Technology **49**, 35 (2006).

- *Doping dependence of optical properties of low-dimensional perovskite-related* $La_{1-y}Ca_yTiO_{3.4\pm\delta}$.
  K. Thirunavukkuarasu, F. Lichtenberg, and C.A. Kuntscher,
  J.Phys.:Condens.Matter **18**, 9173 (2006).

- *Metal-insulator transition in the low-dimensional organic conductor* $(TMTSF)_2FSO_3$ *probed by infrared microspectroscopy.*
  A. Pashkin, K. Thirunavukkuarasu, Y.-L. Mathis, W. Kang and C.A. Kuntscher,
  Eur. Phys. J. B **56**, 285 (2007).

- *Infrared spectroscopy on the rotor-stator compounds* $C_{60}{\cdot}C_8H_8$ *and* $C_{70}{\cdot}C_8H_8$ *under pressure.*
  K. Thirunavukkuarasu, C.A. Kuntscher, Gy. Bényei, I. Jalsovszky, G. Klupp, K. Kamarás, É. Kovats and S. Pekker,
  phys. stat. sol. (b)**244**, 3857 (2007).

- *Pressure-induced phenomena in single-walled carbon nanotubes.*
  C.A. Kuntscher, K. Thirunavukkuarasu, Á. Pekker, K. Kamarás, F. Hennrich, M. Kappes and Y. Iwasa,
  phys. stat. sol. (b) **244**, 3982 (2007).

- *Infrared microreflectance study of magnetically-aligned single-walled carbon nanotubes under pressure.*
  C.A. Kuntscher, K. Thirunavukkuarasu, K. Kamarás, F. Simon and D.A. Walters,
  phys. stat. sol. (b) **245**, 2288 (2008).

- *Infrared spectroscopy on the fullerene C_{70} under pressure.*
  K. Thirunavukkuarasu, C.A. Kuntscher, F. Borondics, G. Klupp, and K. Kamarás,
  phys. stat. sol. (b) **245**, 2006 (2008).

- *Orientational ordering and intermolecular interactions in the rotor-stator compounds $C_{60}{\cdot}C_8H_8$ and $C_{70}{\cdot}C_8H_8$ studied under pressure.*
  K. Thirunavukkuarasu, C.A. Kuntscher, Gy. Bényei, I. Jalsovszky, G. Klupp, K. Kamarás, É. Kovats and S. Pekker, J. Phys. Chem. C **112**, 17525 (2008).